

Representing Sub-failure Quasi-static Ligament Mechanics and Bone Kinematics in a Human
Ankle Finite Element Model

A Thesis

Presented to
the faculty of the School of Engineering and Applied Science
University of Virginia

in partial fulfillment
of the requirements for the degree

Master of Science

by

Adwait Mane

May

2016

APPROVAL SHEET

The thesis
is submitted in partial fulfillment of the requirements
for the degree of
Master of Science



AUTHOR

The thesis has been read and approved by the examining committee:

Dr. Richard W. Kent

Advisor

Dr. Matthew B. Panzer

Dr. Jason L. Forman

Accepted for the School of Engineering and Applied Science:



Craig H. Benson, Dean, School of Engineering and Applied Science

May
2016

Acknowledgements

I would like to thank a number of people who influenced my time as a Master's student at the Center for Applied Biomechanics (CAB) at the University of Virginia (UVA).

I owe thanks to my advisor Professor Richard Kent, for providing me the opportunity to grow as a scholar at the CAB. I have become a better engineer due to your mentorship. I would also like to thank Professor Matt Panzer and Dr. Jason Forman for serving on my thesis committee and for their technical help.

I wish to acknowledge the High Ankle Sprain team for their tireless work on this project, especially Professor Matt Panzer and Dr. Bingbing Nie for patiently answering my questions about computational modeling. Dr. Edward Spratley and Dr. Robert Salzar offered valuable technical advice and feedback during my graduate experience.

I would like to thank Alexander Mait, Carolyn Roberts, and John Paul Donlon for reviewing parts of this document. In addition, I would like to thank Abhiraj for assistance with figure formatting, and Tim Gillispie, Rheba, and Aaron Gardner for the English language review.

I wish to thank all the students and staff at the CAB. Thanks in particular to Alex and Dani for their company in our office at CAB. I would also like to thank my friends and classmates, particularly Abhiraj, Debajyoti, and Trishala who have all helped and encouraged me during this journey.

Finally, I would like to thank my parents, brother, grandparents and relatives for constantly supporting me in all my endeavors. You have been a lifelong source of inspiration and optimism. I am humbled by the confidence you have placed in me and am grateful for your love and dedication.

Abstract

Syndesmotic ankle sprains, along with lateral ankle sprains, account for about 85–90% of foot and ankle injuries. The mechanism of syndesmotic ankle sprains is not well understood because knowledge of the relationship between gross rotations of the foot and *in situ* ligament mechanics is limited.

The objective of this thesis was to develop a human ankle finite element model to gain insight into the relationship between gross ankle mechanics and *in situ* ligament mechanics. The specific goals were to improve the representation of articular cartilage and ligaments in an existing finite element model and to evaluate the bone kinematic and gross moment responses of the model against data from cadaver ankle experiments.

The model was refined and optimized to meet the stated goals. This refinement included a representation of articular cartilage with reduced gaps and of ligaments as distributions of fiber bundles. Each fiber bundle was represented by a bilinear stiffness curve with physically interpretable parameters. One of the parameters was a zero force toe region. The fiber bundle toe regions were optimized to minimize the differences between the responses of the model and those measured from cadaver ankle experiments. Evaluation of the optimized model showed that the bone orientation, bone position and gross moment responses of the model were within 2°, 2 mm and 5 Nm of the experimental data. The optimized model also provided *in situ* ligament stiffness curves that can be used to describe *in situ* ligament behavior, which is difficult to measure experimentally.

The optimized model was used to describe the effect of calcaneus dorsiflexion, eversion and external rotation on the *in situ* force responses of the anterior tibio-fibular ligament. The optimized model predicted that calcaneus dorsiflexion may predispose the anterior tibio-fibular ligament to injury for an external rotation input to the calcaneus. This provided insight into the relationship between gross ankle kinematics and *in situ* ligament mechanics.

The optimized model can be extended to include failure criteria for the fiber bundles. This can facilitate the study of the injury mechanism of syndesmotic ankle sprains, as well as injury prevention strategies.

Table of Contents

List of Figures	v
List of Tables	vii
List of Nomenclature	vii
Contributions.....	viii

Chapter 1. Introduction

1.1. Motivation.....	1
1.2. Research objectives.....	2
1.3. Study design.....	3
1.4. Literature review	6
1.4.1. Functional anatomy of the ankle.....	6
1.4.2. Experimental studies of ankle joint mechanics.....	7
1.4.3. Ankle ligament mechanics.....	9
1.4.4. Computational human ankle models.....	10

Chapter 2. Refinement of the University of Virginia Ankle model

2.1. UVA Ankle model	12
2.2. Ligament representation update	15
2.2.1. Ligament insertion geometry update	15
2.2.2. Ligament modeling approach	15
2.2.3. Discussion	21
2.3. Representation of articular cartilage	21
2.3.1. Methods.....	22
Cartilage model.....	22
Contact definition.....	23
External rotation simulations	27
2.3.2. Results.....	29
Gross moment response under calcaneus external rotation	29
Talus kinematic responses	30
Ligament force responses	30
2.3.3 Discussion	34
Gross moment, talus kinematic and ligament force responses	34
Limitations and future work.....	34
2.4 Discussion and conclusion.....	35

Chapter 3. Optimization of the refined model

3.1 Introduction.....	36
3.2. Sensitivity of design variables	36
3.2.1. Methods.....	36
Simulation setup.....	36
Algorithm of the sensitivity study.....	37

3.2.2. Results of sensitivity analysis	39
3.2.3. Discussion	40
Implications of the sensitivity analysis	40
Sample size and design variable ranges	43
3.2.4. Conclusions	43
3.3. Optimization of <i>in situ</i> fiber toe regions	44
3.3.1. Methods	44
Bone kinematics obtained from cadaver ankle experiments	44
Model optimization and evaluation setup	46
3.3.2. Results	48
3.3.3 Model evaluation	51
3.3.4. Discussion	53
<i>In situ</i> fiber toe regions and ligament stiffness curves	53
Model evaluation	55
3.3.5. Summary	56

Chapter 4. *In situ* behavior of the anterior tibio-fibular ligament

4.1. Introduction	57
4.2. Methods	58
4.3. Results	59
4.4. Discussion	63
Talar wedging and fibular translation at 0° of calcaneus yaw rotation	63
Talar wedging and fibular translation at 30° of calcaneus yaw rotation	64
Comparison with experimental studies	65
4.5. Conclusion	69

Chapter 5. Conclusions, limitations and future work

5.1. Conclusions	71
5.2. Limitations	72
5.3. Future work	73
References	74
Appendix 1	80

List of Figures

Figure 1. Gross rotations of the ankle (Shin et al. 2012).	1
Figure 2. Overall approach for meeting research objectives.	4
Figure 3. Bones of the foot and ankle (Shin et al. 2012).	6
Figure 4. a) Lateral (left image) and medial (deltoid) ankle ligaments b) Syndesmotoc ankle ligaments (Williams et al. 2014). The AITFL and PITFL (superficial and deep) are referred to as the ATiF and PTiF in this thesis.	7
Figure 5. Experimental setup used by Wei et al. (2010) (left) to measure the gross rotational stiffness of the ankle (right).	8
Figure 6. Displacement field in ATiF under uniaxial loading reported by Forestiero et al. (2014).	11
Figure 7. The model developed by Shin et al. (2012) was validated for gross kinematic and dynamic behavior. The forefoot impact case is shown above.	13
Figure 8. Local coordinate systems defined on the bones.	14
Figure 9. Comparison of insertion geometries of the PTaF, PTiF, ATaF and ATiF showing updates made in the refined model.	16
Figure 10. The ATiF represented by a distribution of springs, with each spring representing a fiber bundle.	17
Figure 11. Schematic of an <i>in situ</i> ligament stiffness curve.	18
Figure 12. Stiffness curve for a fiber bundle (referred to as a fiber for simplicity) showing the toe region and linear stiffness region.	19
Figure 13. Linearized ATiF stiffness curve.	20
Figure 14. Compressive stress vs strain curve used to define cartilage response in the refined model (Mow and Mansour 1977).	23
Figure 15. Representative 3-D thickness distribution maps of the a) talus b) tibia and c) fibula (Millington et al., 2007).	24
Figure 16. Articular cartilage meshes in the refined model.	25
Figure 17. Bone meshes of the baseline and refined models showing the addition of cartilage (ligaments excluded).	26
Figure 18. Cross section in y-z plane shows that the addition of cartilage (bottom right image) reduces gaps between the bones.	27
Figure 19. Schematic of the experimental test rig (Mait et al. 2015).	28
Figure 20. Boundary conditions for the simulations.	29
Figure 21. Gross moment response of the refined and baseline model compared with the experimental value reported by (Mait et al., 2015).	30
Figure 22. Rigid body displacements of the talus (from neutral foot, zero-load state) in the tibia coordinate system. Non-zero displacement at 0° foot external rotation is due to motion during axial preload.	31

Figure 23. Intrinsic rigid body orientations of the talus in the tibia coordinate system. Non-zero orientation at 0° foot external rotation is due to motion during axial preload.	32
Figure 24. Ligament force responses of the baseline and refined models. Ligament force is the sum of forces in all fibers.	33
Figure 25. The 100(1- α)% confidence interval determines the significance of the regression coefficient.	39
Figure 26. Sensitivity analysis on the yaw-pitch-roll angle during of the fibula, the talus, and the navicular during the in-plane rotation around the Z-axis of the tibia. The * symbol represents regression coefficients that are not statistically significant.	41
Figure 27. A representative quantile-quantile (QQ) plot of residuals vs standard normal samples for the multivariate linear regression model. The QQ plot for the talus yaw regression model is shown here.	42
Figure 28. Flowchart of the optimization for determining <i>in situ</i> ligament properties (Nie et al. 2016).	45
Figure 29. a) Schematic of the experimental test rig (Mait et al. 2015). b) Illustration of the Local Coordinate System (LCS) defined for each bone (Shown: left foot) (Nie et al. 2016).	46
Figure 30. The orientations of the talus and fibula of the optimized model are closer to the experimental response of specimen 743L. The range of the other two cadaver specimens is shown with the responses of specimen 743L.	49
Figure 31. Comparison of the bone angles and displacements of the experiments and the optimized model on single rotations of the foot (model optimization) (Nie et al. 2016).	50
Figure 32. <i>In situ</i> ligament stiffness curves of the CT, PTaF, CF and ATiF from the FE model under external rotation of the calcaneus relative to the tibia. The PTaT, ATaF, and PTiF were not loaded under an external rotation input.	52
Figure 33. Comparison of the rotation moment (applied at the calcaneus) of the experiments and the model under multiple rotations.	53
Figure 34. Comparison of the bone kinematics of the experiments, and the responses predicted by the model when multiple rotations were applied (model evaluation) (Nie et al. 2016).	54
Figure 35. Peak force in the ATiF for external rotation with different initial conditions.	59
Figure 36. Schematic showing forces at 20° calcaneus dorsiflexion (DF20; top row) and 20° calcaneus eversion (EV20; bottom row) in the ankle ligaments. The black dot (top left image) is the instantaneous center of calcaneus dorsiflexion.	60
Figure 37. Total force in the ATiF, and bone kinematics for the ER30 (left column) and DF20+ER30 (right column) cases.	61
Figure 38. Total force in the ATiF, and bone kinematics for the EV20+ER30 (left column) and the DF20+EV20+ER30 (right column) cases.	62
Figure 39. Schematic of talus motions that cause the talus to wedge into the ankle mortise.	63
Figure 40. Schematic showing subtalar joint unlocking mechanism under calcaneus eversion (Button et al. 2015). The sustentaculum tali (shown by arrow) of the calcaneus locks with the	

articulating surface of the talus in the neutral position (top images). When everted, these surfaces unlock (bottom images).	66
Figure 41. Lateral view of a left foot showing cadaver athletic taping pattern used by Wei et al. (2012) (left image). Schematic to show that the taping pattern may have increased the stiffness of the subtalar joint (right image).....	68

List of Tables

Table 1. Updates to UVA Ankle model for model refinement.	14
Table 2. Insertion widths of the ankle ligaments in the model.	17
Table 3. Definition of design variables and their ranges for the parametric ankle model. R^2 indicates the fit of the linear regression when defining the fiber material.....	20
Table 4. Cartilage mesh characteristics in refined model.	26
Table 5. Design variables definition and range selection of the parametric ankle model.	37
Table 6. Accuracy of the regression models. mR^2 is the coefficient of multiple determination, ..	40
Table 7. A representative table of regression coefficients, confidence intervals, and p values for the six most statistically significant DVs (based on p values) of the talus yaw model.	42
Table 8. Experimental loading conditions and the input rotation angles of the calcaneus used for model optimization and evaluation purpose (subject 743L).	46
Table 9. Values of the objective function at the initial and final iteration.....	48
Table 10. Optimized <i>in situ</i> toe regions of fibers of ankle ligaments. The relative length of the toe region was determined as its ratio relative to the initial ligament length (Nie et al. 2016).	51
Table 11. Deviations of model responses from experimental ranges.	54
Table 12. Abbreviations describing rotation inputs applied to the calcaneus.....	58
Table 13. Comparison of ATiF force and talus yaw in optimized model and experiments reported by Wei et al. (2012).	67

List of Nomenclature

i	index identifying ankle ligaments
c_i (mm)	<i>in situ</i> fiber bundle toe region of ligament i
$l_{0,i}$ (mm)	initial length of ligament i
n_i	number of fiber bundles in ligament i
K_i (N/mm)	linear stiffness of ligament i
DV	design variable
p	index identifying design variables
x_p	design variable
s	number of design variables for sensitivity study
X	vector whose elements are design variables
r	index identifying response variables
y_r	response variable in linear regression model

b_p	regression coefficient
Δx_p	range of design variables
m	index identifying sub-optimization
$\Delta d_x, \Delta d_y, \Delta d_z$	bone displacements in x, y and z directions

Contributions

Paper I

Mane, A., Panzer, M. B., Nie, B., Forman, J. L., Mait, A. R., & Kent, R. W. (manuscript in preparation for resubmission). Refining a Finite Element Model of the Human Ankle to Study High Ankle Sprains: Representation of Articular Cartilage.

Division of work between authors: Nie, Panzer and Mane developed the outline of this study. Panzer created the cartilage mesh with the help of Mane. Mane ran the simulations and analyzed the results with the help of Panzer and Nie. The paper was written by Mane, and was reviewed by all authors. This study is described in Section 2.3 of this thesis.

Paper II

Nie, B., Panzer, M. B., Mane, A., Mait, A. R., Donlon, J. P., Forman, J. L., & Kent, R. W. (2015). A framework for parametric modeling of ankle ligaments to determine the in situ response under gross foot motion. *Computer methods in biomechanics and biomedical engineering*, 1-12.

Division of work between authors: Nie, Panzer and Mane developed the outline of this study. Nie developed the sampling strategy and ran the simulations with the help of Mane. Nie analyzed and presented the results with the help of Mane and Panzer. The paper was written by Nie with the help of Mane, and was reviewed by all authors. This study is described in Sections 2.2 and 3.2 of this thesis.

Paper III

Nie, B., Panzer, M. B., Mane, A., Mait, A. R., Donlon, J. P., Forman, J. L., & Kent, R. W. (in second round of review). In situ behavior of ankle ligaments. *Annals of Biomedical Engineering*.

Division of work between authors: Nie, Panzer and Mane developed the outline of this study. Mane and Nie implemented the optimization routine and ran the simulations. Mane and Nie analyzed and presented the results with the help of Panzer. The paper was written by Nie with the help of Mane, and was reviewed by all authors. This study is described in Section 3.3 of this thesis.

Symposium Presentation of the Included Work

Mane, A., Nie, B., Panzer, M. B., Donlon, J. P., Mait, A. R., & Kent, R. W. (2015). Human Ankle Ligament Toe Region Identification through Inverse Finite Element Approach. *13th International Symposium on Computer Methods in Biomechanics and Biomedical Engineering*. Montreal, Canada.

Chapter 1

Introduction

1.1. Motivation

Ankle sprains are the most common athletic injury, accounting for 10–28% of all athletic injuries (Ekstrand & Tropp, 1990; Garrick, 1977). Lateral and syndesmotic ankle sprains account for about 85–90% of foot and ankle injuries (Rubin & Sallis, 1996). Syndesmotic ankle sprains, also called high ankle sprains, are ligament injuries to the distal tibiofibular syndesmosis that are more severe and require greater recovery time than lateral ankle sprains (Boytim, Fischer, and Neumann 1991; Guise 1975). In the clinical literature, external rotation (Figure 1) of the foot relative to the tibia is considered the primary injury mechanism of many syndesmotic ankle sprains (Nussbaum et al. 2001; Boytim, Fischer, and Neumann 1991; Waterman et al. 2010), however some studies have suggested that eversion and dorsiflexion also play a role (Boytim, Fischer, and Neumann 1991; Wei et al. 2012; Sarrafian 1983; Norkus & Floyd 2001; Wolfe et al. 2001; Waterman et al. 2011). The precise injury mechanism of syndesmotic ankle sprains remains unclear due to limited knowledge of the relationships between gross foot and ankle kinematics and the resultant ligament mechanics.

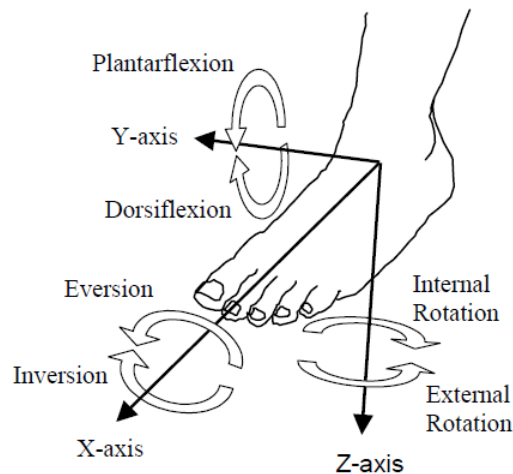


Figure 1. Gross rotations of the ankle (Shin et al. 2012).

An understanding of *in situ* ligament mechanics is needed to investigate mechanisms of syndesmotic ankle sprains hypothesized in the clinical literature. While the mechanical characteristics of isolated ligaments are well understood, our knowledge of several aspects of the *in situ* behavior is lacking. *In situ* mechanics are characterized by complex behaviors such as pre-stress, slack, and non-homogeneous deformation patterns. A complete representation of *in situ*

ligament stress-strain behavior using experiments alone is difficult (reviewed in Section 1.2.3). Computational models provide tractable alternatives as they can be used as surrogates to provide measurements that are difficult to record experimentally (reviewed in Section 1.2.4). They also have the advantage of high controllability and repeatability, and the cost of a simulation is far less than the cost of an experiment. A computational human ankle model validated and verified with experimental data can provide a better understanding of *in situ* ligament behavior.

1.2. Research objectives

The overall objective of this thesis was to gain insight into the relationship between gross ankle mechanics and *in situ* ligament mechanics under quasi-static, sub-failure conditions during internal and external rotation, dorsiflexion, and eversion. This required an improvement in the representation of ligaments and articular cartilage compared to a previous model developed by Shin et al. (2012) and refined by Gabler et al. (2014) which did not attempt to represent *in situ* ligament mechanics.

The specific objective of this thesis was to develop a human ankle finite element (FE) model with the following characteristics by enhancing the existing model developed by Gabler et al. (2014):

Objective 1: Representation of ankle bone geometry from the existing FE model.

Objective 2: A more physiological representation of the ankle ligaments compared to that in the existing model. A more physiological representation refers to the following:

Objective 2a: Representation of more anatomically reasonable insertion geometries.

Objective 2b: Representation of distributed fiber bundles. This objective is motivated by ligament microstructure.

Objective 3: Representation of the following salient features that have a physical interpretation in an *in situ* ligament stiffness curve:

Objective 3a: A zero-force *in situ* toe region.

Objective 3b: A smooth nonlinear stiffening region between the zero force *in situ* toe region and the non-zero linear stiffness region.

Objective 3b: A non-zero linear stiffness region.

Objective 4: Representation of articular cartilage to reduce the gaps between articular surfaces to less than 0.2 mm, and to produce physically more realistic bone kinematics compared to a model with larger gaps between articulating surfaces.

Objective 5: Model responses evaluated as follows:

Objective 5a: Bone orientation responses of the model evaluated to obtain a mean deviation from the experimental range of less than 2°.

Objective 5b: Bone position responses of the model evaluated to obtain a mean deviation from the experimental range of less than 2 mm.

Objective 5c: Gross moment responses of the model evaluated to obtain a deviation from the experimental range of less than 5 Nm.

Another objective of this thesis was as follows:

Objective 6: Describe the relationship between *in situ* force in the anterior tibio-fibular ligament and kinematic responses of the talus and fibula for combinations of gross rotation inputs to the calcaneus that are relevant to syndesmotic ankle sprains (dorsiflexion, eversion and external rotation).

Objectives 3 and 6 can provide insight into *in situ* ligament mechanics, which is the overall objective of this thesis. The other objectives are intermediate goals to enable Objectives 3 and 6 to be met.

1.3. Study design

This section describes the approach taken to combine the individual objectives to work towards the overall objective. The approach consisted of three parts: 1) model refinement, 2) model optimization, and 3) evaluation of model responses by comparing them with cadaver ankle responses (Figure 2).

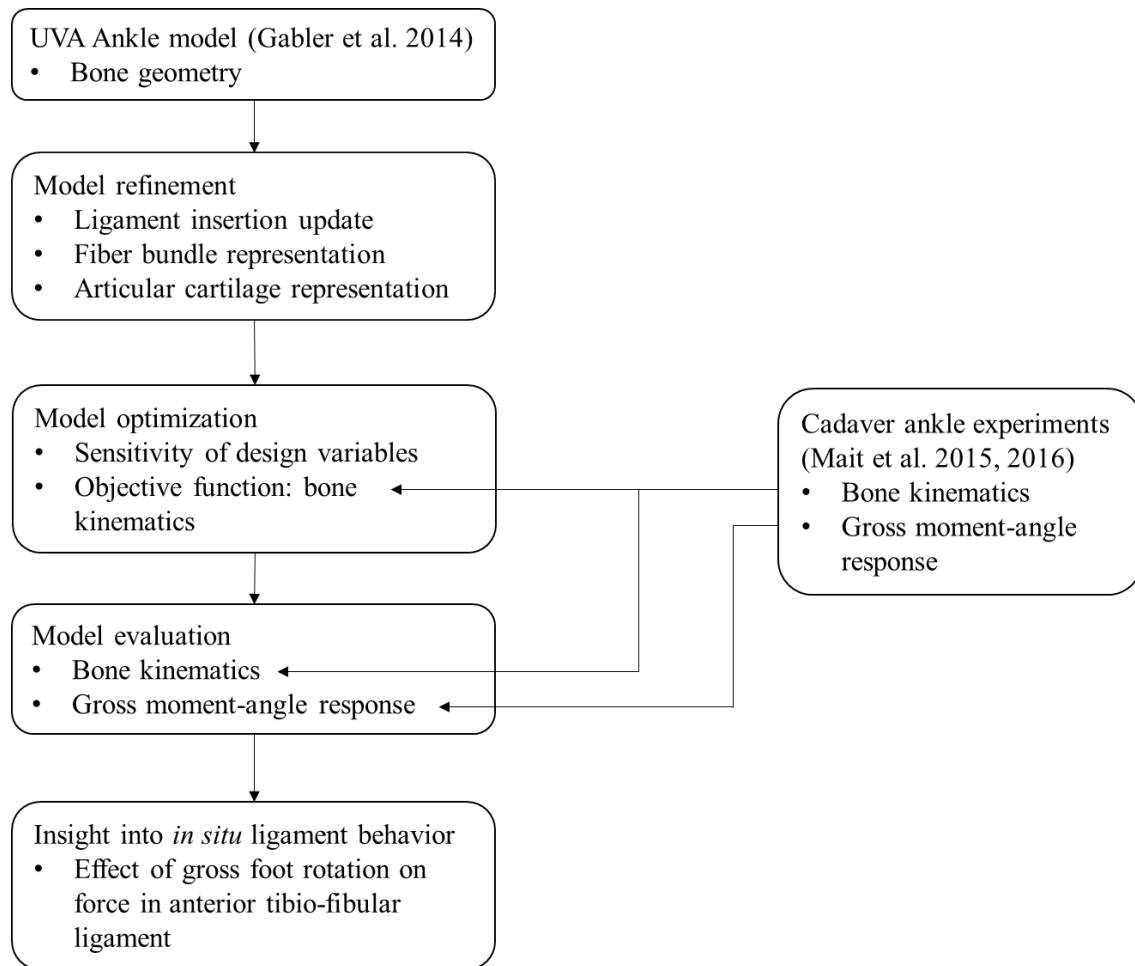


Figure 2. Overall approach for meeting research objectives.

Shin et al. (2012) developed a foot and ankle FE model for automotive impact scenarios as part of the Global Human Body Model Consortium (GHBMC). This model was updated by Gabler et al. (2014) to obtain the University of Virginia (UVA) Ankle model. The UVA Ankle model was validated under dynamic forefoot impact, axial rotation, dorsiflexion, and combined loadings. These validation cases are at the level of gross ankle mechanics. Since one of the objectives of this thesis was to evaluate the kinematics of individual bones against those measured in cadaver ankle experiments, it was necessary to refine and optimize the UVA Ankle model.

Chapter 2 describes the refinement of the UVA Ankle model. The representation of ligaments in the UVA Ankle model was updated. The UVA Ankle model relied on simple one and two spring ligament representations and approximate locations of ligament insertions. While these were adequate to validate the gross ankle mechanics in the UVA Ankle model, a finer representation

was necessary to meet the objectives of this thesis. One of the objectives was a more physiological representation of the ligaments. To meet this objective, the ligament insertion geometries were updated and the ligaments were represented as distributed fiber bundles. A bilinear stiffness curve that included a zero force *in situ* toe region and a non-zero linear stiffness region was defined for each bundle. The fiber bundle representation was motivated by the objective of representing the salient features of *in situ* ligament stiffness curves (Objective 3).

Chapter 2 also describes the representation of articular cartilage for refining the model. The UVA Ankle model had gaps between the ankle bones in the order of 2-3 mm, which led to physically unrealistic hard contact at the bone interfaces. A layer of cartilage was added to the ankle bones to meet the objective of reducing the gaps to less than 0.2 mm. The model with the updated ligaments and articular cartilage is referred to as the refined model.

Chapter 3 discusses the optimization and evaluation of the refined model. The parameters representing the fiber bundles were used as the design variables. A sensitivity study was performed to identify the design variables that had the greatest influence on the kinematics of the ankle bones. The most sensitive design variables were then used to optimize the model. An objective function was defined to measure the difference between the bone kinematics of the model and a cadaver ankle, and an optimization study was performed to minimize the objective function. The optimized model was evaluated against measurements from cadaver ankle experiments (Objective 5).

In chapter 4, the optimized model was used to describe how gross ankle mechanics affect some of the talus and fibula kinematics. The relationship between important kinematic responses of the talus and fibula and the *in situ* behavior of the ATiF is also described. This provided insight into mechanisms that may predispose the ATiF to injury. This chapter pertains to Objective 6.

The approach of refining, optimizing, and evaluating the model comprised the steps taken to meet the overall objective of gaining insight into the relationship between gross ankle mechanics and ligament mechanics under quasi-static, sub-failure kinematic inputs in internal and external rotation, dorsiflexion and eversion. The ligament mechanics thus obtained can be interpreted as *in situ* ligament behavior.

1.4. Literature review

1.4.1. Functional anatomy of the ankle

The ankle is one of the most intricate joints in the human body and plays an important role in functions such as mobility and stability of the human body. The complex morphology of the ankle joint enables the competing goals of mobility, necessary for locomotion over uneven terrain, and stability, necessary for bearing loads of several times body weight. The primary structures of interest in this study are the ankle and subtalar joints, including the surrounding connective tissues. The ankle joint is also called the talocrural joint. The bones of the ankle include the tibia, fibula, talus and calcaneus, along with the tarsal complex (Figure 3).

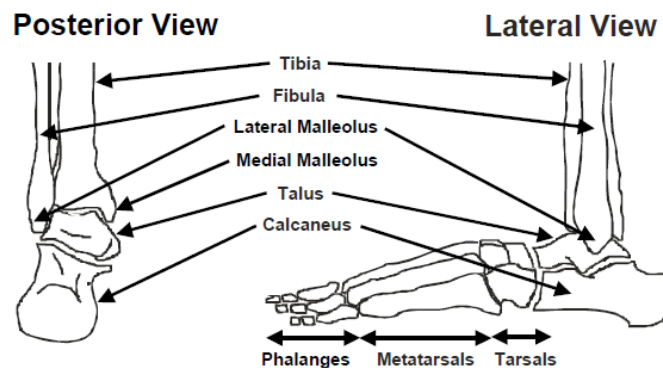


Figure 3. Bones of the foot and ankle (Shin et al. 2012).

The connective tissues include ligaments that fall into three broad categories: deltoid, lateral and syndesmotic ankle ligaments (Figure 4). The anterior talo-tibial (ATaT), posterior talo-tibial (PTaT), calcaneo-tibial (CT), and tibio-navicular (TiN) ligaments comprise the deltoid, originating from the medial malleolus, which stabilizes the ankle joint on the medial side. Originating from the lateral malleolus, the lateral ligaments, namely the anterior talo-fibular (ATaF), posterior talo-fibular (PTaF) and calcaneo-fibular (CF) ligaments, stabilize the ankle joint on the lateral side. The syndesmotic ankle ligaments, which include the anterior tibio-fibular (ATiF) and posterior tibio-fibular (PTiF) ligaments, are relatively stiff ligaments that comprise the distal syndesmosis and stabilize the ankle mortise. The interosseous membrane (IOM) extends between the tibia and fibula and is narrower and thicker distally. It runs distally and laterally along the tibia and fibula and stabilizes the two bones. The ankle also consists of tendons that transfer muscle loads (Netter et al. 2010). Mobility is achieved through rotations of the ankle (Figure 1). Broadly, these are plantar/dorsiflexion about an axis running medial to lateral and connecting the medial and lateral malleolus; internal/external rotation about an axis roughly collinear with the shaft axis of the tibia;

and inversion/eversion about the long axis of the foot through the subtalar joint. Precise definitions of the coordinate system are provided in Section 2.1.

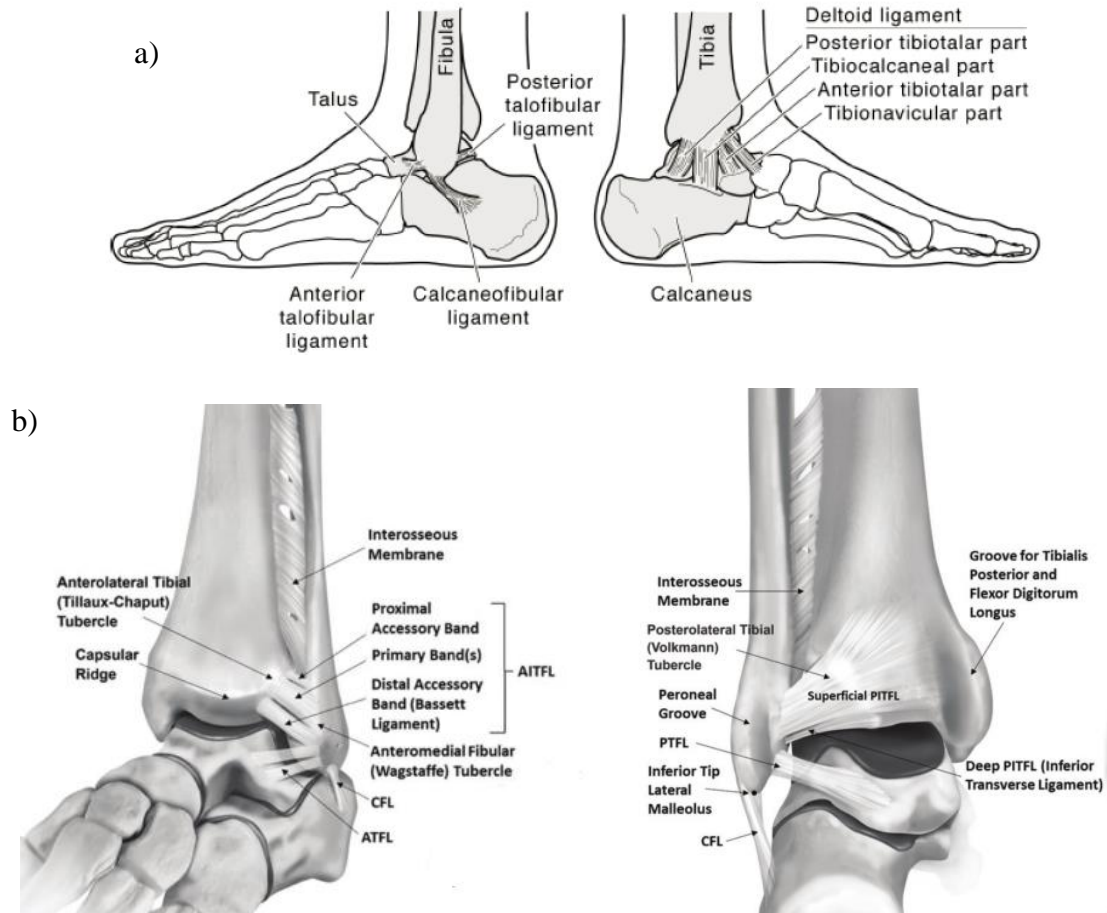


Figure 4. a) Lateral (left image) and medial (deltoid) ankle ligaments b) Syndesmotic ankle ligaments (Williams et al. 2014). The AITFL and PITFL (superficial and deep) are referred to as the ATiF and PTiF in this thesis.

1.4.2. Experimental studies of ankle joint mechanics

There is a vast literature in the orthopedics community that addresses the stability of the ankle when some ligaments are compromised (Johnson and Markolf 1983; Siegler, Chen, and Schneck 1988; Xenos et al. 1995). Ligaments of interest are sequentially sectioned, and the effect on joint stability is studied. Such studies tend to focus on the gross rotational stiffness of the ankle for clinical diagnosis of ligament injury. The gait and locomotion research community has also devoted considerable attention to ankle mechanics with an emphasis on bone kinematics and

ligament mechanics (Carson & Harrington, 2001; Jenkyn & Nicol, 2007). The goal of such studies is to obtain correlations between pathological gaits and foot and ankle mechanics, eventually developing effective treatments for pathological gaits. All of these studies make at least one of the following assumptions: 1) the axis of joint rotation is held constant 2) skin-mounted markers represent the underlying bone kinematics. These assumptions limit the applicability of these studies for the objective of this thesis. Mait et al.'s (2015; 2016a; 2016b) experiments conducted at the Center for Applied Biomechanics at the University of Virginia provide the best experimental setup and boundary conditions for obtaining bone kinematics under natural joint motion.

The gross moment response of the ankle under internal and external rotation has been reported in the literature. Johnson et al. (1983) reported the rotational stiffness of cadaver ankles up to 8 degrees of internal and external rotation. In this study, the contribution of the anterior talofibular ligament in stabilizing the ankle joint was studied by recording the rotational stiffness before and after sectioning the ligament. Chen et al. (1988) reported rotational stiffness of up to 21 degrees of external rotation and 29 degrees of internal rotation. Wei et al. (2010) reported the rotational stiffness up to 50 degrees of external rotation (Figure 5). In all these studies, fibula motion was constrained in all degrees of freedom. In addition, an internal/external rotation axis was imposed on the ankle to simplify the experimental setup, but it is well known that the rotation axis varies during joint motion (Lundberg et al. 1989; Parenteau et al. 1998). Due to these simplifying assumptions, the responses reported in these studies differ from the responses obtained during natural joint motion.

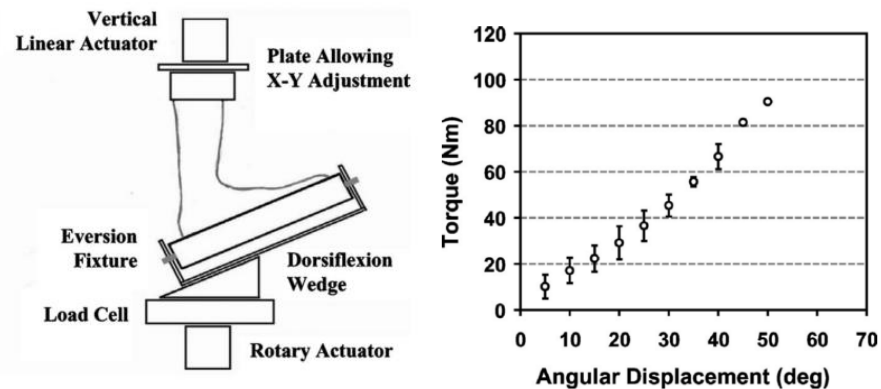


Figure 5. Experimental setup used by Wei et al. (2010) (left) to measure the gross rotational stiffness of the ankle (right).

The kinematics of the talocrural and subtalar joints have been studied in the gait and locomotion research community (Jenkyn & Nicol 2007). However, these studies use human volunteer subjects and rely on skin-mounted markers to obtain the underlying bone kinematics. Skin motion artifact

in the foot leads to relative motion between the markers and the underlying bone: Tranberg and Karlsson (1998) reported relative motion between the bones and skin of 4.3 mm and 2.3°, and Reinschmidt et al. (1997) reported relative motion of 4.4°. These studies can be used to evaluate a computational model, but finer model validation requires kinematics obtained from bone-mounted markers.

Bone-mounted markers have been used to measure talus kinematics under gross external rotation loading of the foot within physiological ranges of motion (Siegler et al. 1988) and at failure (Villwock, Meyer, Powell, & Haut, 2009). Similar to the studies reporting gross moment responses, these studies constrain fibula motion in all degrees of freedom and impose an internal/external rotation axis.

Mait et al. (2015) designed experiments with functionally relevant boundary conditions and recorded the gross kinetics and bone kinematics of the foot. The fibula was unconstrained in all degrees of freedom at the boundaries. The axis of external rotation of the foot was allowed to move during joint motion. The leg was sectioned at the knee, so the entire interosseous membrane was intact for the duration of the test. Markers were mounted on each of the ankle bones. These improvements over previous studies allowed more natural joint motion and a more precise determination of bone kinematics. Therefore, the data from these tests were used to optimize the computational model.

1.4.3. Ankle ligament mechanics

The response of isolated ankle ligaments in uniaxial tension is well known in the literature. Funk et al. (2000) reported linear and quasi-linear viscoelastic models and failure properties of eight ankle ligaments based on uniaxial step relaxation and ramp tests. Funk et al.'s analytical model is based on a phenomenological discrete element representation of each ligament. Lucas et al. (2009) reported viscoelastic and failure properties of collagen fascicles from porcine specimens. This study is part of a larger effort to develop a general ligament model based on microstructural properties. Since excised specimens were used in both studies, the *in situ* state was lost. Measuring *in situ* ligament responses experimentally is challenging. Therefore, the *in situ* response of ankle ligaments is not fully understood.

In situ measurements of ligament elongations provide insight into one aspect of *in situ* ligament behavior. Colville and Zarins (1990) measured the elongations of lateral and syndesmotic ligaments of cadaver ankles in flexion under a range of initial moments in internal/external rotation and inversion/eversion. Strain gages were sutured to the ligaments to obtain the *in situ* elongations. De Asla et al. (2009) measured *in vivo* elongations of the ATaF and CF in four static foot positions using a combination of dual-orthogonal fluoroscopic and magnetic resonance imaging (MRI) techniques. Such ligament elongation measurements represent one aspect of the stress-strain behavior of ligaments. Force or stress-field measurements are required along with elongation or

strain-field measurements for a complete description of the stress-strain characteristics. This task is extremely challenging because currently available force sensors or load cells are inadequate for mounting on being implanted in ligaments. To the author's knowledge, no study has reported simultaneous *in situ* measurements of stress and strain in ankle ligaments. Moreover, any attempt to measure *in situ* ligament behavior by attaching external devices, especially by suturing, can alter the *in situ* mechanical behavior.

A complete description of the *in situ* behavior of the ankle ligaments that accounts for pre-stress and slack is difficult using experiments alone. Wei et al. (2011) pursued a computational approach. A multi-body computational model was validated using bone kinematic data from experiments with skin-mounted markers for tracking bone motion. The computational model was then used to obtain ligament strains through forward dynamics simulations. While this study was a useful proof-of-concept, several simplifying assumptions were made (reviewed in the next section), and the skin-mounted markers introduced skin motion artifacts in the bone kinematic data.

Current experimental techniques are inadequate for obtaining a complete description of *in situ* mechanics of ankle ligaments. Computational models can provide a tractable alternative for obtaining *in situ* mechanics of ankle ligaments, but models validated at the level of bone kinematics are necessary for such an endeavor. This thesis reports the development of such a model, which is referred to as the refined model. The refined model represents *in situ* slack in the ankle ligaments, which is a step towards a complete description of *in situ* mechanics of ankle ligaments.

1.4.4. Computational human ankle models

Computational models complement experimental approaches to study gross joint mechanics. While multi-body ankle models can provide rapid solutions for joint mechanics (Button, Feng, & Haut, 2015; Kwak, Blankevoort, & Ateshian, 2000; Liacouras & Wayne, 2007; Wei, Hunley, Powell, & Haut, 2011), FE models have the ability to obtain the stress and strain information of the ligaments (Cheung et al. 2006; Reggiani et al. 2006). Several FE foot and ankle models have been developed by comparing the global model response with experimental results (Tannous et al. 1996; Beillas et al. 1999). These models can predict joint mechanics at the structural level. Since these models do not account for complex load paths and ligamentous structure and were validated under only a few simple loading conditions, they cannot reliably predict bone kinematics and *in situ* ligament mechanics.

Shin et al. (2012) developed an FE model of the foot and leg that showed improved biofidelity relative to previous FE models. The model was validated for gross kinetic and kinematic behavior in several loading conditions including, forefoot impact, axial rotation, dorsiflexion, and combined loadings. No attempt was made to validate the model at the bone kinematics and ligament mechanics level. A more detailed review of the model is provided in Section 2.1. Wei et al. (2011) reported *in situ* ligament behavior using a multi-body model, but the bone kinematic data used for

model validation was based on skin-mounted markers, which can move as much as 4.3 mm and 2.3° relative to the underlying bones (Tranberg and Karlsson 1998). Currently, the relationship between gross ankle mechanics and the underlying bone kinematics and ligament mechanics remains unclear.

Detailed three-dimensional computational models of ligaments have been reported in the literature. Gardiner and Weiss (2003) developed an FE model of the human medial collateral ligament using a transversely isotropic hyperelastic material model. Each ligament is defined by five material parameters. The FE model of the talocrural and subtalar joints developed by Forestiero, Carniel, and Natali (2014) have two parameters for the fibers in each ligament with additional parameters for the ground matrix and viscous effects. Twenty-four parameters are needed to describe the ligaments of the talocrural and subtalar joints. These models can provide detailed stress-strain fields in the ligaments (Figure 6) but are limited by the large number of parameters needed and increased computational cost. A further limitation is that ligament toe regions and pre-stress are not represented, and gross joint mechanics are not considered.

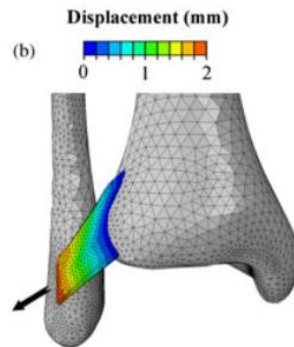


Figure 6. Displacement field in ATiF under uniaxial loading reported by Forestiero et al. (2014).

This thesis is a step towards understanding the relationship between gross ankle mechanics and the underlying *in situ* ligament mechanics. The optimized model can be the starting point for studying *in situ* ligament mechanics and then incorporating ligament failure to study the injury mechanism of syndesmotic ankle sprains.

Chapter 2

Refinement of the University of Virginia Ankle model

Computational ankle models in the literature have relied on approximate ligament insertion geometries, and one or two spring approximations for ligaments (Gabler, Panzer, and Salzar 2014; Wei et al. 2011). Such models have left gaps between articular surfaces (UVA Ankle model) or included articular cartilage as part of the bone (Wei et al., 2011). Section 2.1 reviews the UVA Ankle model. Refinement of this model through an updated representation of ligaments and articular cartilage was necessary to achieve Objectives 2 and 4. This is described in sections 2.2 and 2.3.

2.1. UVA Ankle model

An FE model of a human foot and ankle was originally developed for the Global Human Body Model Consortium (GHBMC) for their 50th percentile male seated occupant model (owned and licensed by GHBMC – version 3.5) (Shin, Yue, & Untaroiu, 2012). This model was developed to improve understanding of mechanisms of injuries to the ankle and subtalar joints in automotive impact scenarios, and was validated for gross kinematic and dynamic behavior in multiple loading conditions, including forefoot impact (Figure 7), axial rotation, dorsiflexion, and combined loadings. The bones of the leg, and ankle and subtalar joints were modeled as deformable structures, while the forefoot and midfoot bones were modeled as rigid bodies. Ligaments were defined as nonlinear springs using the stiffness curves reported by Funk et al. (2000). Flesh and skin were modeled as deformable parts. The model developed by Shin et al. (2012) was updated to improve biofidelity under high-rate axial loading conditions (Gabler, Panzer, & Salzar, 2014). The updates included refinement of meshes for several bones and an improved heel pad model. The model with the updates of Gabler et al. (2014) is referred to as the UVA Ankle model in this thesis. The UVA Ankle model was the starting point for model refinement in this thesis (Table 1).

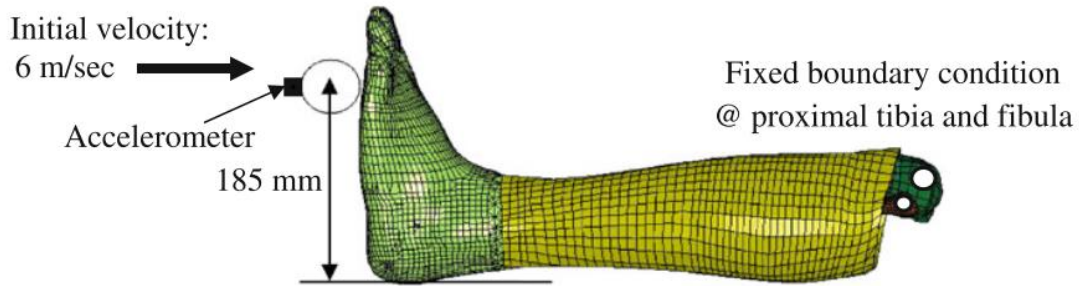


Figure 7. The model developed by Shin et al. (2012) was validated for gross kinematic and dynamic behavior. The forefoot impact case is shown above.

Since the UVA Ankle model was developed to predict the gross structural response of the ankle, an approximate representation of ligaments and insertion geometries was sufficient. Each of the ankle ligaments was modeled using one or two spring elements, and ligament insertions were estimated on the anatomical descriptions of Netter et al. (2010) and a commercial database of human anatomy (<http://www.3dcadbrowser.com>) since ligament insertion geometries were unavailable for the subject whose computed tomography scans were used to define bone geometries.

To obtain the refined model, orthogonal right-handed coordinate systems were defined on the tibia, fibula, talus, calcaneus, and navicular. For the tibia, the Z-axis was defined by the axis of the minimum principal moment of inertia. The origin was the intersection of the Z-axis and the plafond, and the Y-axis passed through the apex of the medial malleolus (Figure 8). For the remaining bones, the origins were located at the centroid of the bones (except the fibula, whose origin was at the centroid of the lateral malleolus) and the coordinate axes were parallel to those of the tibia for a neutral unloaded foot. The tibia coordinate system was defined as the global coordinate system. This coordinate system definition was chosen since it was based on anatomical landmarks and could be easily defined for the bone geometry of cadaver ankles used for evaluating the refined model.

Table 1. Updates to UVA Ankle model for model refinement.

	UVA Ankle model	Refined model*
Ligaments	Approximate ligament insertion geometries (section 2.1)	Ligament insertion geometries updated (section 2.2.1)
	Ligaments represented as one or two spring approximations	Ligaments represented as distributed fiber bundles (section 2.2.2)
	Nonlinear ligament stiffness curves (Funk et al. 2000)	Bilinear fiber bundle stiffness curves (section 2.2.2)
Cartilage	No articular cartilage	Articular cartilage represented (section 2.3)
Flesh and heel pad	Flesh and heel pad represented	No flesh and heel pad
Bones	Elastoplastic bones	Rigid bones

* The baseline model (section 2.3) is identical to the refined model with the exception that articular cartilage is not represented in the baseline model.

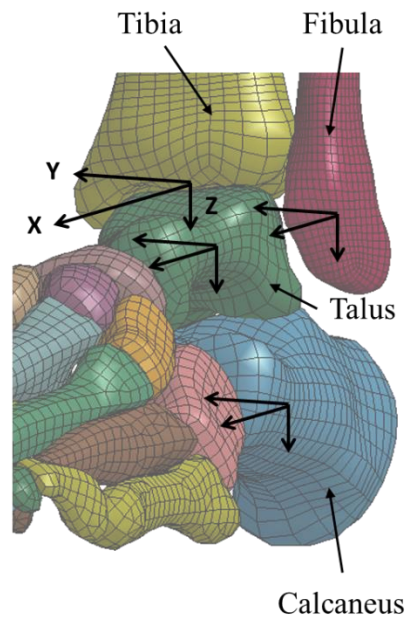


Figure 8. Local coordinate systems defined on the bones.

2.2. Ligament representation update

2.2.1. Ligament insertion geometry update

Ligament insertion geometries affect the load paths in human joints, and consequently affect the bone kinematics and ligament mechanics. Observations of PTaF, PTiF, ATaF and ATiF insertion geometries in UVA Ankle showed meaningful deviations from insertion geometries reported in anatomical studies (Figure 9). The insertion geometries of these ligaments were updated to meet Objective 2a. The insertion widths of nine ankle ligaments were obtained from anatomical studies (Table 2).

It is challenging to identify ligament insertions in a cadaver since the ligaments blend with the bones and surrounding soft tissues at the insertion sites (Figure 9). Idealized representation of ligament insertions from Netter et al. (2010) were used as a reference to get a general idea of the insertion geometries. Anatomical studies from the literature were used to obtain finer details. A combination of sources was used to determine the ligament insertion geometry when incomplete information was available.

2.2.2. Ligament modeling approach

The overall objective of this thesis was to study ligament mechanics which includes complex behaviors such as non-homogeneous deformations of ligament fibers. Because the one- or two-spring ligament representation in the UVA ankle model was inadequate for this purpose, an updated representation of ligaments motivated by ligament microstructure was obtained.

Ligaments are made of bundles of collagen fascicles (also called fibers) (Kastelic, Palley, & Baer, 1980; Lucas et al., 2009). In the refined model, a distribution of springs loaded in tension was used to represent a ligament (Figure 10). Each spring represented a mechanically functional fiber bundle, which is hereafter referred to as “fiber” for simplicity.

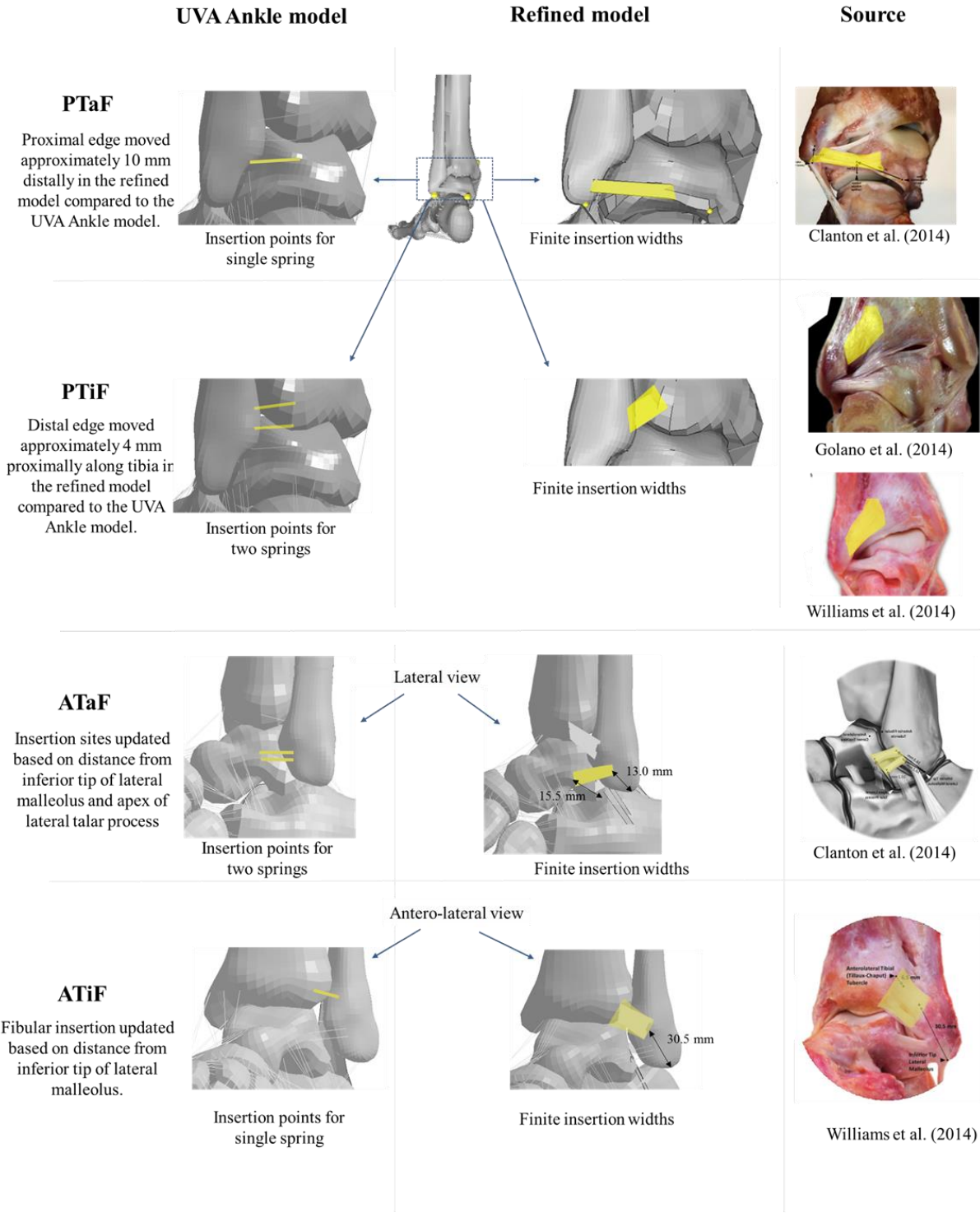


Figure 9. Comparison of insertion geometries of the PTaF, PTiF, ATaF and ATiF showing updates made in the refined model.

Table 2. Insertion widths of the ankle ligaments in the model.

Ligament/IOM list	No.	Insertion geometry				Reference	
		Bone	Insertion width (mm)	Bone	Insertion width (mm)		
Deltoid	ATaT	1	Talus	6.4	Tibia	7	(Campell et al. 2014)
	PTaT	2	Talus	6.4	Tibia	7	
	CT	3	Calcaneus	6	Tibia	6	
	TiN	4	Tibia	12.6	Navicular	9.3	
Lateral	ATaF	5	Talus	3.5	Fibula	4.7	(Clanton et al. 2014)
	PTaF	6	Talus	4.8	Fibula	4.3	
	CF	7	Calcaneus	10	Fibula	10	
High ankle	ATiF	8	Tibia	15	Fibula	15	(Golano et al. 2014, Williams et al. 2014)
	PTiF	9	Tibia	15	Fibula	10	

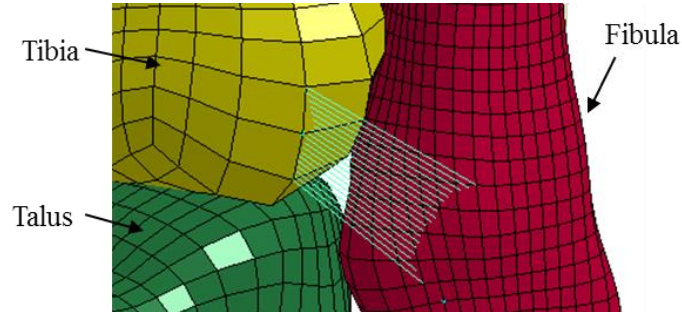


Figure 10. The ATiF represented by a distribution of springs, with each spring representing a fiber bundle.

The *in situ* stiffness curve of an ankle ligament shows three distinct regions (Figure 11): a zero-force region associated with *in situ* slack in the ligament and corresponding to the ligament being in a “buckled” state (Nigg, Skarvan, & Yeadon, 1990), a nonlinear stiffening region that is related to fascicle uncrimping, and a nonzero linear stiffness region that corresponds to ligament elongation when all fascicles are uncrimped. The *in situ* slack and fascicle uncrimping region together are referred to as a composite *in situ* ligament toe region, or simply ligament toe region, in this thesis. Since *in situ* slack is a structural characteristic of a ligament, the ligament toe region is also a structural characteristic.

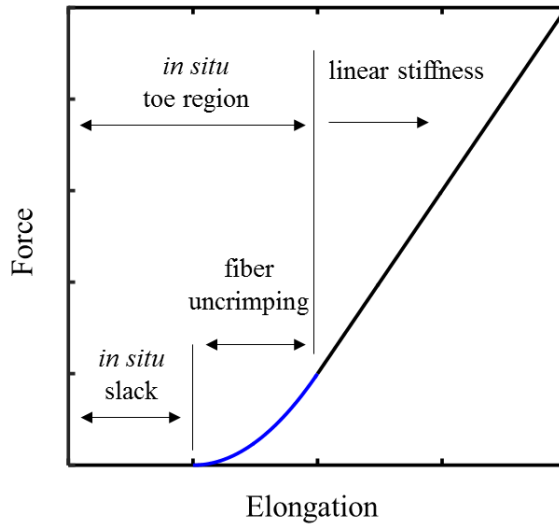


Figure 11. Schematic of an *in situ* ligament stiffness curve.

Each fiber in a ligament was represented by a bilinear stiffness curve (Figure 12). This was done for nine ankle ligaments and the IOM. The *in situ* stiffness curve of each fiber showed two regions (Figure 12): a zero-force *in situ* toe region, referred to as “fiber toe region” for simplicity, and a non-zero linear fiber stiffness region. The variable c_i (mm) refers to the *in situ* fiber toe region of a ligament i ($i = 1, \dots, 9$). A bilinear representation was chosen for the fiber stiffness so that the model could be easily parameterized in the sensitivity and optimization studies described in Chapter 3. The distribution of the IOM fibers was defined by the skewness of the IOM and was represented by a geometric series as follows

$$d_j = \alpha^{j-1}$$

where α is the skewness parameter and d_j is the distance between successive fibers in the proximal direction. The distance between the two most distal fibers was 1 mm.

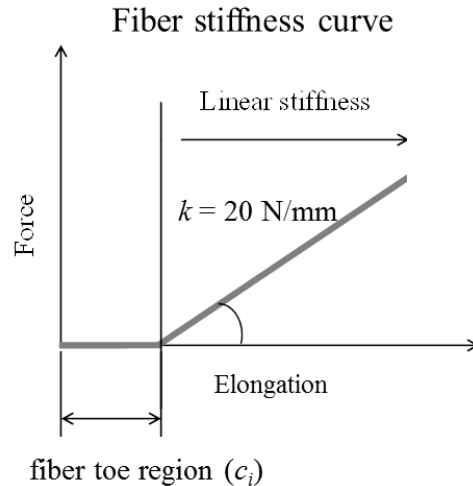


Figure 12. Stiffness curve for a fiber bundle (referred to as a fiber for simplicity) showing the toe region and linear stiffness region.

Literature on the length of the toe regions of ankle ligaments is sparse as the toe regions are difficult to obtain experimentally. Clinical studies support the notion of a composite ligament toe region in ankle ligaments (Nigg et al., 1990). Nigg et al. (1990) reported a wide range from (2 - 50%) of ligament initial length for ankle ligament toe regions. Therefore the upper bound for the fiber toe regions was set to 50% of initial ligament length (Table 3) for the sensitivity study described in Section 3.2.

The fiber stiffness was determined from a linear approximation of the nonlinear stiffness curves (Funk et al. 2000) used for the UVA Ankle model. The stiffness of each fiber was set to 20 N/mm, which is the ligament fascicle stiffness reported by Lucas et al. (2007) rounded to the nearest multiple of 10 N/mm. The instantaneous elastic force-elongation relationships reported by (Funk et al., 2000) were linearized (Figure 13) to obtain nominal ligament stiffness values, K_i . The nominal number of fibers in a ligament, n_i , was obtained by dividing the linearized ligament stiffness value by the linear fiber stiffness value. The linear fiber stiffness was the same for all the ligaments while the number of fibers varied across the ligaments.

$$K_i \text{ (N/mm)} = 20 \cdot n_i \quad (i = 1, \dots, 9)$$

The lower bound for the number of fibers in each ankle ligament was half the nominal value and the upper bound was twice the nominal value. For the midfoot and forefoot ligaments, the material properties used by Shin et al. (2012) were retained.

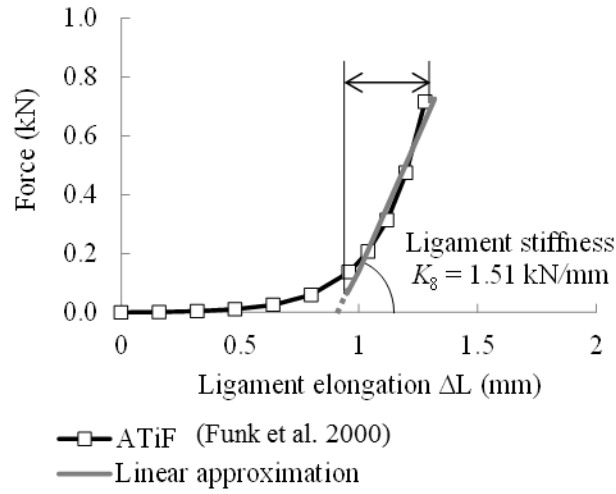


Figure 13. Linearized ATiF stiffness curve.

Table 3. Definition of design variables and their ranges for the parametric ankle model. R^2 indicates the fit of the linear regression when defining the fiber material.

Ligament/IOM list		No. (i)	Basis value			Design variable (DV) ($x_p, p = 1, \dots, 20$)			
			$l_{0,i}$ (mm)	K_i (N/mm)	R^2	Toe region (c_i) (mm)		Fiber number (n_i)	
						Lower bound	Upper bound	Lower bound	Upper bound
Deltoid	ATaT	1	20.8	125	0.91	0	10.4	3	12
	PTaT	2	11.9	826	0.80	0	6.0	21	82
	CT	3	22.7	302	0.99	0	11.4	8	30
	TiN	4	33.2	39	1.00	0	16.6	1	4
Lateral	ATaF	5	16.5	89	0.94	0	8.3	2	9
	PTaF	6	25.0	770	0.93	0	12.5	19	77
	CF	7	15.2	452	0.82	0	7.6	12	46
High ankle	ATiF	8	16.5	1516	0.92	0	8.3	38	152
	PTiF	9	14.8	1258	0.99	0	7.4	31	126
IOM	Fibers	10	-	-	-	-	-	10	100
	Skewness		-	-	-	-	-	1	1.2

2.2.3. Discussion

The insertion geometries of the ATiF, ATaF, PTiF and PTaF were updated in the refined model to meet the objective of a more anatomically reasonable representation of ligament insertions (Objective 2a) compared to the UVA Ankle model. The relatively simple bilinear representation at the fiber level can represent the salient features (Objective 3) of an *in situ* stiffness curve at the ligament level (Figure 11). Superposition of the forces in the fibers generates the total ligament force. The zero force *in situ* slack region and the non-zero linear stiffness regions of the ligament stiffness curve correspond to the zero-force and linear regions of the fiber stiffness curves. While nonlinear stiffening is observed experimentally in a ligament in uniaxial tension, nonlinear stiffening in the model is a result of rotations of the bones. A gross rotation input applied to the calcaneus causes the individual bones to rotate and produces non-homogeneous elongation of the fibers in a ligament. This is discussed in more detail in Section 3.3.

2.3. Representation of articular cartilage

The computational ankle models reviewed in Section 1.3 have been validated at a gross structural level. The objectives of this thesis are to represent bone kinematics and mechanics of individual ankle ligaments, for which gross structural validation is necessary, but not sufficient. Cartilage defines the geometry of the articular surfaces of a joint, and the geometry of the articular surfaces strongly influences the load paths and the relative bone motion in a joint. The UVA Ankle model and the computational ankle models reviewed in Section 1.4.4 did not represent deformable cartilage. This section describes how representation of articular cartilage in the refined model leads to more physically realistic gross ankle mechanics, local talus kinematics and ligament force responses.

Representation of articular cartilage is an objective of this thesis (Objective 4). Cartilage defines the geometry of the articular surfaces of a joint, and the geometry of the articular surfaces strongly influences the load paths and the relative bone motion in a joint. The UVA Ankle model and the computational ankle models reviewed in Section 1.4.4 did not represent deformable articular cartilage since they focused largely on gross ankle mechanics. Representation of cartilage is relevant to the objectives of this thesis as it can provide more physically realistic bone kinematics. This can enable evaluation of the bone kinematic responses of the model against experimentally measured responses (Objective 5), and eventually help us gain insight into *in situ* ligament mechanics.

2.3.1. Methods

Cartilage model

The topography of talar, tibial and fibular cartilage were defined using 3D stereophotographic scan data of a disarticulated ankle joint reported by Millington et al. (2007) (Figure 15). Millington et al.'s data were used primarily to obtain the cartilage thickness. The region of the bone surface covered by cartilage was obtained from Netter (2010). Calcaneal cartilage thickness was estimated to be similar to the thickness of the cartilage surface it articulated against i.e. inferior talar cartilage. These data were used as a reference for creating the articular cartilage surfaces for each bone in the model (Figure 16 and Figure 17), and the resulting model was defined as the refined model in this study. The cartilage meshes were a single element in thickness. Pentahedral elements were used for the edge elements for a smooth transition to the bone, and hexahedral elements were used for the rest of the mesh. A selective reduced integrated element formulation was used. The resulting cartilage mesh had relatively good mesh quality (Table 4) and was finer than the bone mesh since the cartilage parts were deformable and the bones were rigid.

For all cartilage parts, the *MAT_057 card with a user-defined compressive nonlinear stress-strain curve (Mow and Mansour 1977) (Figure 14) and a nominal density value of 1000 kg/m^3 was used (LS-Dyna Keyword User's Manual – Volume II – R7.1). This relatively simple material definition was sufficient for the objectives of this study. The focus of this study was to provide smoother contact at articular interfaces compared to the UVA Ankle model and to reduce gaps between the articular surfaces (Figure 18), rather than to obtain stress and strain distributions in the cartilage parts. This material definition also gave numerically stable results for all simulations, which was a high priority. Nonlinear stiffening in compression was desirable to reduce instability in regions of high stress.

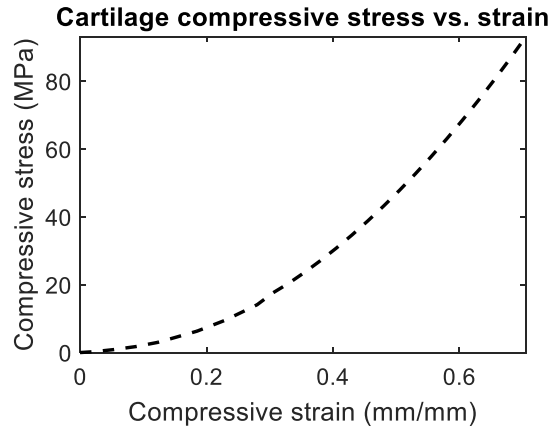
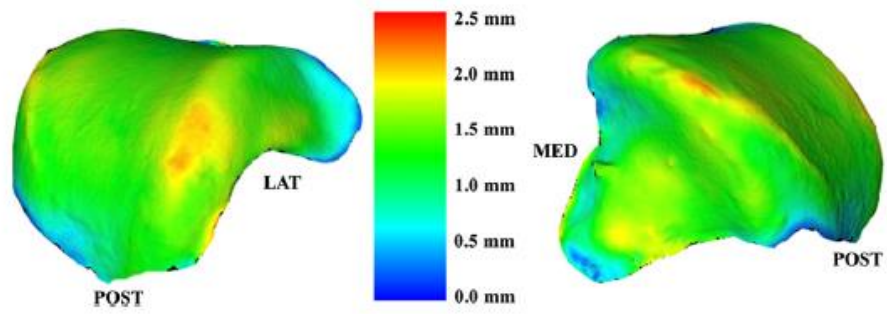


Figure 14. Compressive stress vs strain curve used to define cartilage response in the refined model (Mow and Mansour 1977).

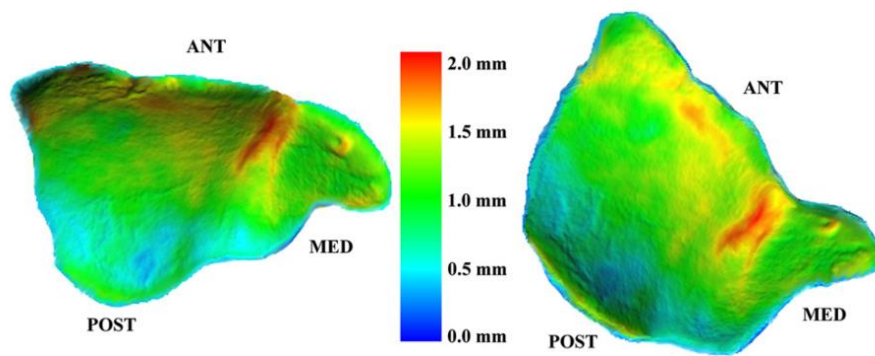
Contact definition

A contact algorithm was used to define the interaction of articular cartilage surfaces. A kinematic constraint based contact algorithm was implemented using the *CONTACT_CONSTRAINT_SURFACE_TO_SURFACE card in LS-Dyna. The synovial capsule was not modeled since the lubricating effect of the synovial fluid was incorporated by using a low static and dynamic friction coefficient of 0.05, which was found to give a more numerically stable solution than lower values of the friction coefficients. No kinematic joints were used in the model so that joint motion was governed by ligamentous constraints and contact forces alone.

a)



b)



c)

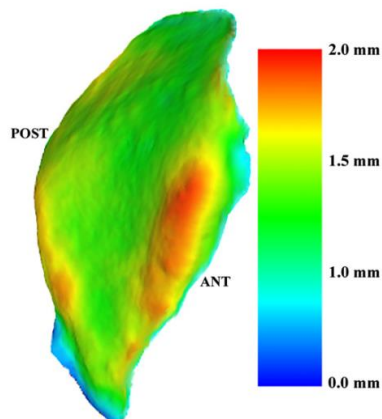


Figure 15. Representative 3-D thickness distribution maps of the a) talus b) tibia and c) fibula (Millington et al., 2007).

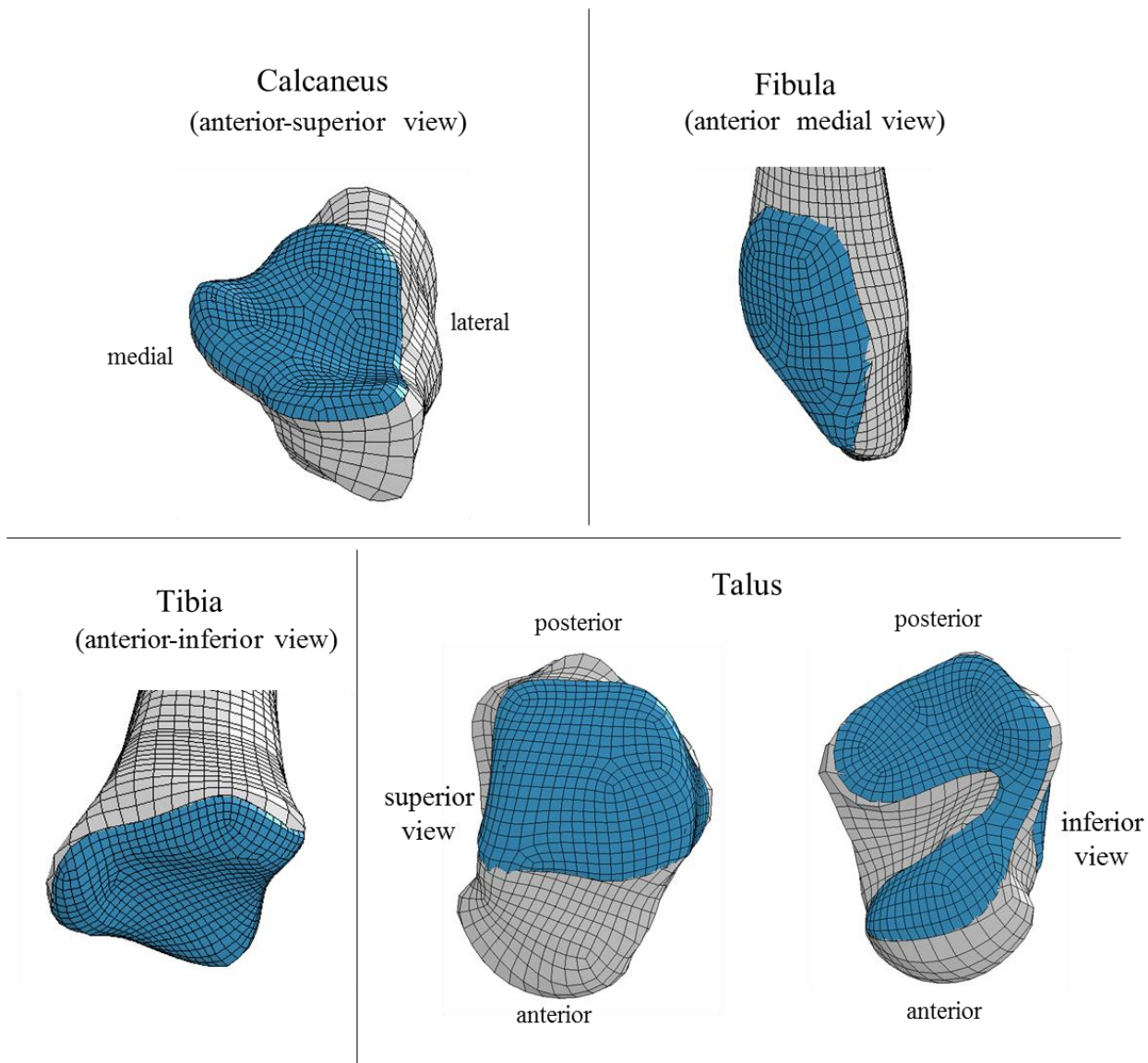


Figure 16. Articular cartilage meshes in the refined model.

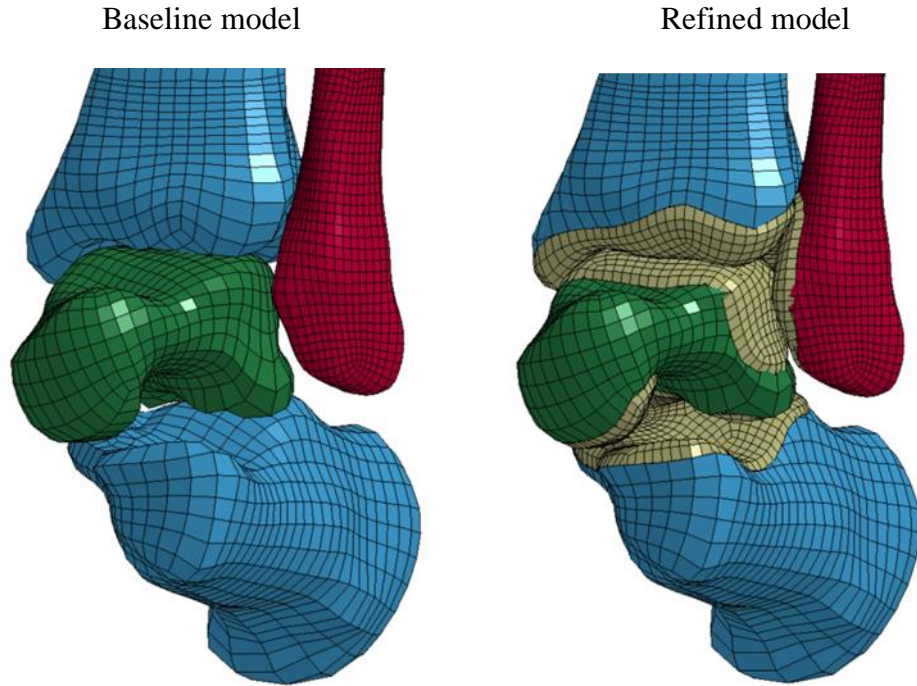


Figure 17. Bone meshes of the baseline and refined models showing the addition of cartilage (ligaments excluded).

Table 4. Cartilage mesh characteristics in refined model.

No. of solid elements	2636
Mean element volume	0.51 mm ³
Solid elements with Jacobian Ratio > 0.7	87%
Minimum Jacobian Ratio	0.35
Minimum element timestep	1.03 μs

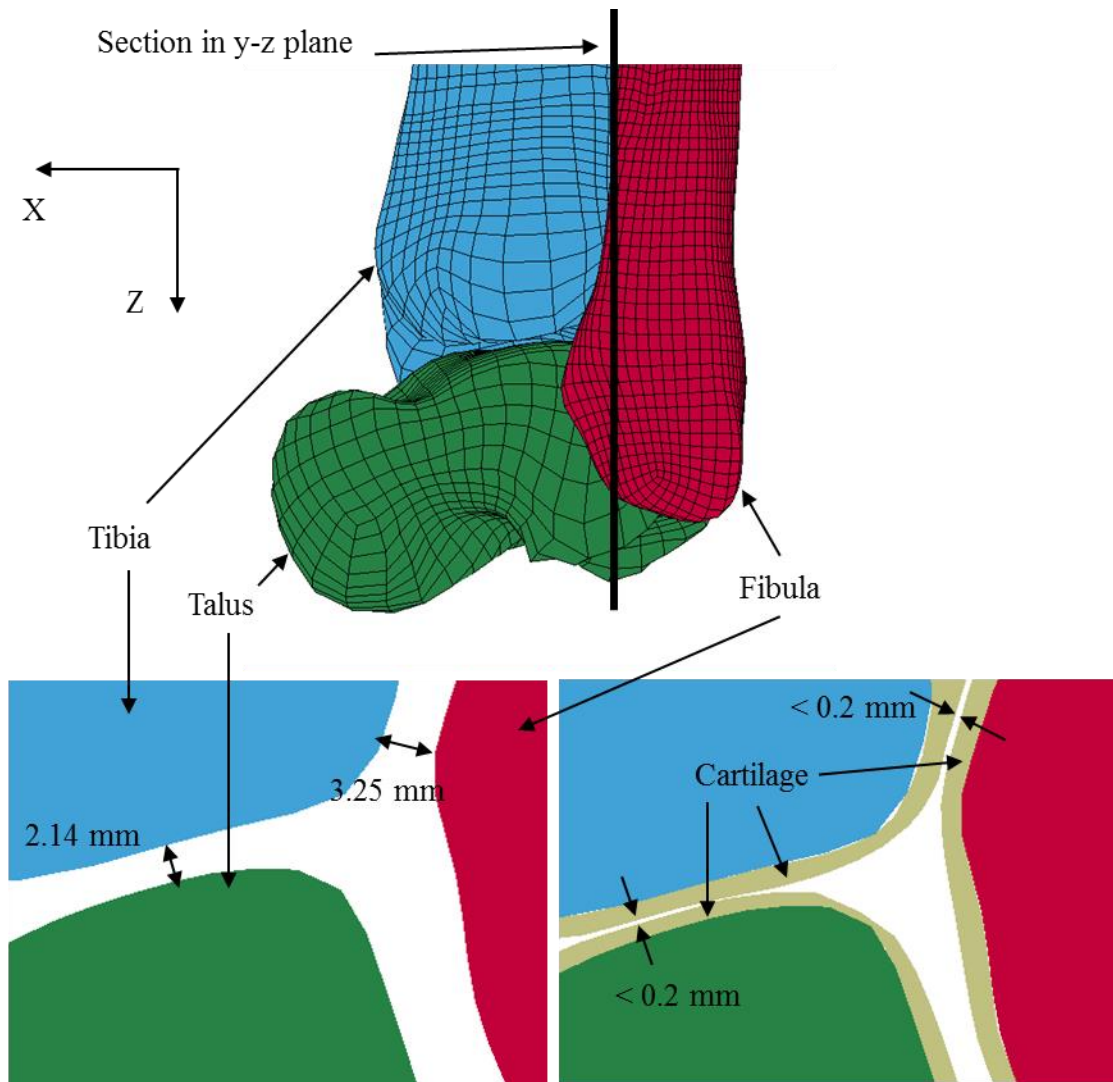


Figure 18. Cross section in y-z plane shows that the addition of cartilage (bottom right image) reduces gaps between the bones.

External rotation simulations

A 500N axial preload (representing approximate force on one foot for a standing 100 kg person) followed by a 30° external rotation input was applied to the calcaneus about the axis specified by Parenteau et al. (1998) (Figure 20). The rotation input is referred to as foot external rotation. The loading was quasi-static since the ratio of kinetic energy to internal energy was less than 2.5% for the simulation. The calcaneus was free to translate in all directions to reduce off-axis reaction moments and forces. Calcaneus rotations about the global X and Y axes were constrained. These boundary conditions are consistent with the experimental boundary conditions used by Mait et al.

(2015). The tibia was constrained in all degrees of freedom. All other bones were unconstrained. All simulations were performed using the LS-DYNA explicit FE solver (version R7.1, Livermore Software Technology Corporation, Livermore, CA).

The boundary conditions used for the simulations and for Mait et al.'s (2015) experimental study (Figure 19) allowed natural joint motion since the internal/external rotation axis was allowed to translate in the X-Y plane during joint motion. This was possible because the calcaneus was free to translate in the X and Y directions. In comparison, the experimental studies reviewed in Section 1.2 of this thesis imposed an internal/external rotation axis on the ankle and constrained fibula motion.

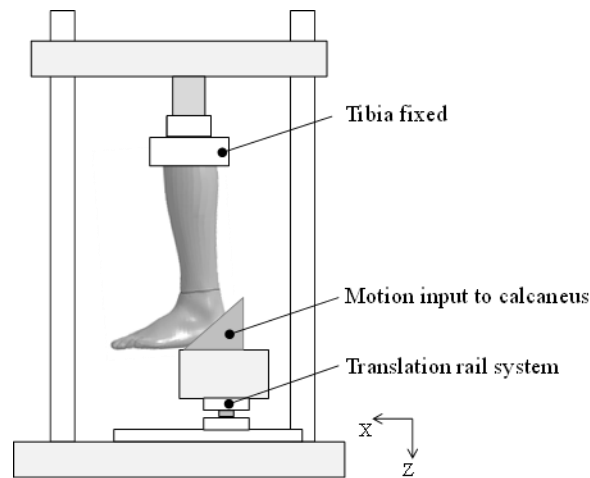


Figure 19. Schematic of the experimental test rig (Mait et al. 2015).

Since boundary conditions were applied to the tibia and calcaneus, differences in the local bone kinematics of the baseline and refined models were assessed using talar motion. All talar motions were measured with respect to the initial position and orientation of the talus in the unloaded state. The intrinsic description of yaw, pitch and roll rotations was used (Shabana, 2013). Briefly, yaw, pitch and roll refer to rotations about the body-fixed Z, Y, and X axes such that pitch is the rotation about the body-fixed Y axis obtained after the yaw rotation, and roll is the rotation about the body-fixed X axis after the yaw and pitch rotations. The external rotation input refers to calcaneus yaw relative to the tibia coordinate system.

Ligament forces were calculated as the sum of forces generated in all fibers of the ligament. The five ankle ligaments considered in this study were the ATiF, ATiT, TiN, CFL and PTaF.

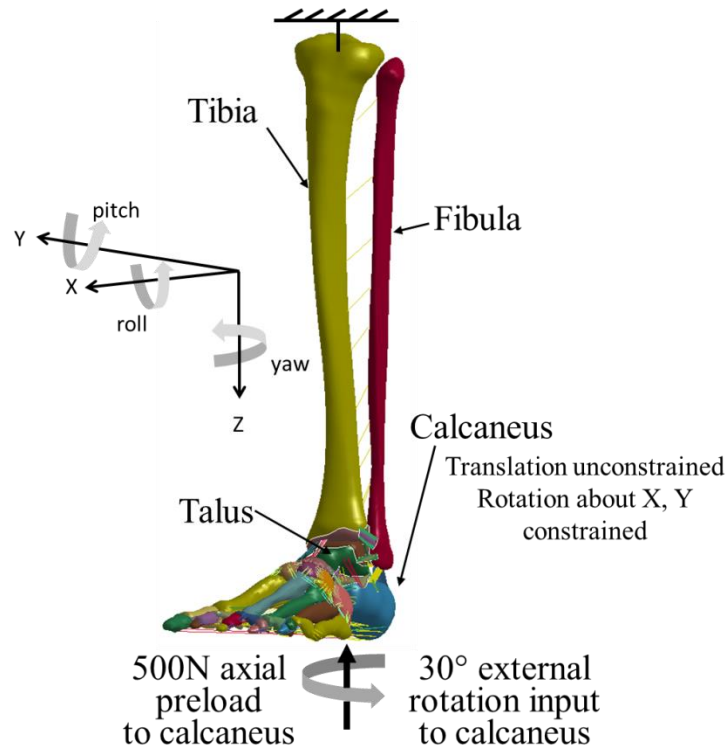


Figure 20. Boundary conditions for the simulations.

2.3.2. Results

In the results and discussion, smoothness refers to a qualitative assessment of the model responses. A response curve from the refined model was considered smoother than the corresponding curve from the baseline model when it had fewer and smaller local peaks and valleys, and smaller changes in slope. For instance, the talus displacement response curves of the refined model were smoother than the response curves of the baseline model (Figure 22). The smoother response curves generated by the refined model were more physically realistic (discussed in Section 2.3.3).

Gross moment response under calcaneus external rotation

The gross moment responses of the baseline and refined models under external rotation of the calcaneus were compared. The responses of both models showed good biofidelity compared to a single experimental data point (Mait et al., 2015) (Figure 21). However, noticeable differences were observed between the two models throughout the simulated rotation, both in the moment-angle response curves and in the animations. The refined model response was smoother than the baseline model response, and the latter had substantial “noise” in the moment-angle signal. This can be explained by the gaps between the bones which result in hard contact when the bones

interact. A low pass filter (200 Hz cutoff frequency) was needed to remove high frequency noise from the response of the baseline model. Filtering was not needed to assess the signal of the refined model since it had a fairly smooth response during the external rotation.

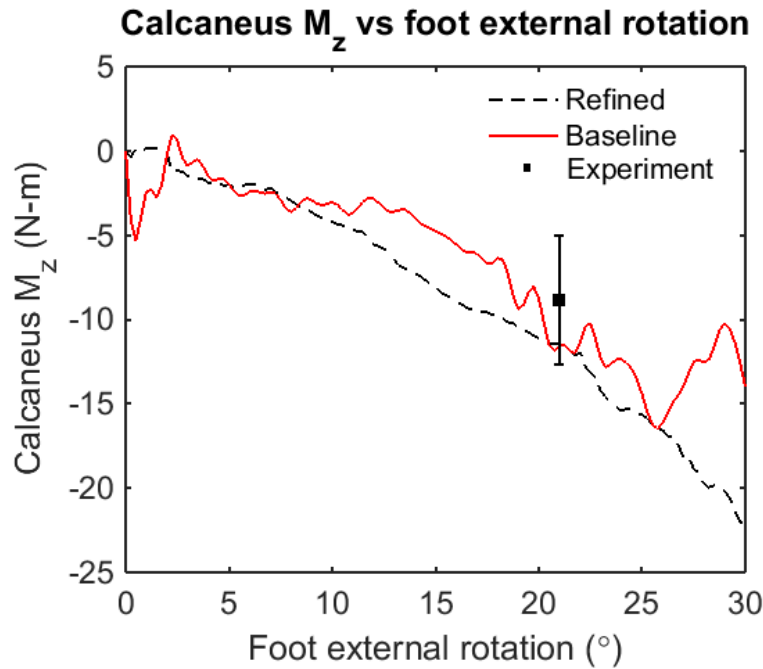


Figure 21. Gross moment response of the refined and baseline model compared with the experimental value reported by (Mait et al., 2015).

Talus kinematic responses

Talus rigid body displacements and orientations of the baseline and refined model were compared (Figure 22 and Figure 23). The displacements and orientations are relative to the unloaded state, so non-zero values at 0° external rotation were due to the axial preload phase. Similar to what was observed for the gross moment-angle response, the refined model had smoother kinematic responses during the external rotation while the baseline model responses were noisy. Noticeable differences in talar motion were observed between these two cases, even at 20° external rotation where the external moments were similar.

Ligament force responses

There were also noticeable differences in the measured ligament forces between the baseline and refined model for the five ankle ligaments (Figure 24). A 200 Hz cutoff frequency low pass filter was needed to remove high frequency numerical noise from the response of the baseline model.

The ATaT (refined model) and the TiN (Figure 24 b and c) have non-zero force at zero foot rotation since they were first loaded during axial preload whereas the ATiF, ATaT (baseline model), CF and PTaF (Figure 24 b, d and e) were first loaded during foot external rotation. Large peaks and valleys are seen in the ligament force response curves beyond 20° of foot external rotation. Bone translation and rotation leads to ligament elongation, and the nonlinear relationship between ligament elongation and force magnifies the peaks and valleys in the bone translation and rotation response curves.

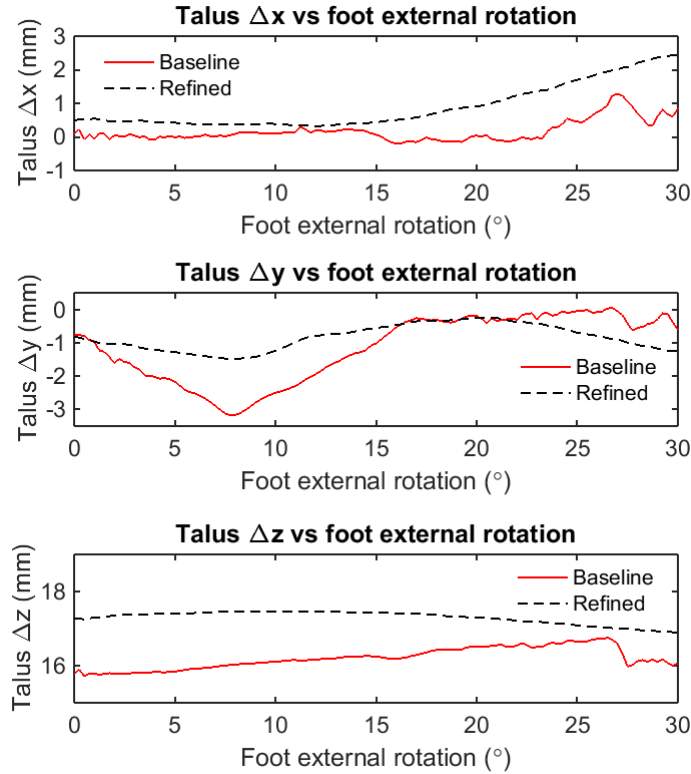


Figure 22. Rigid body displacements of the talus (from neutral foot, zero-load state) in the tibia coordinate system. Non-zero displacement at 0° foot external rotation is due to motion during axial preload.

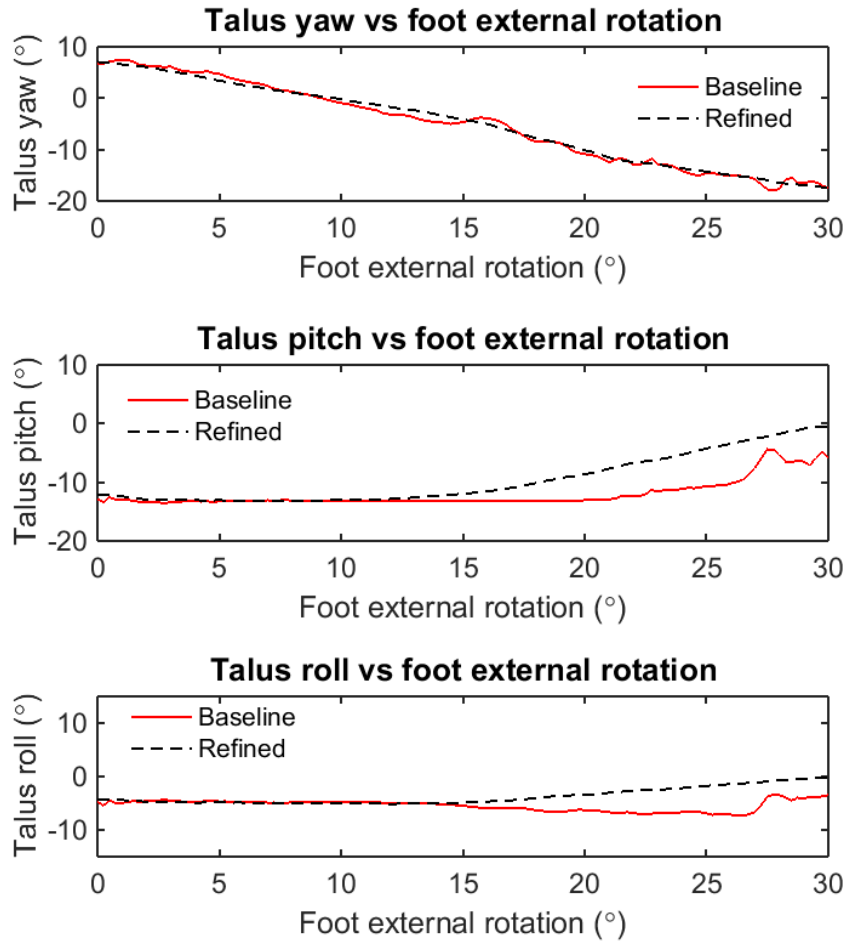


Figure 23. Intrinsic rigid body orientations of the talus in the tibia coordinate system. Non-zero orientation at 0° foot external rotation is due to motion during axial preload.

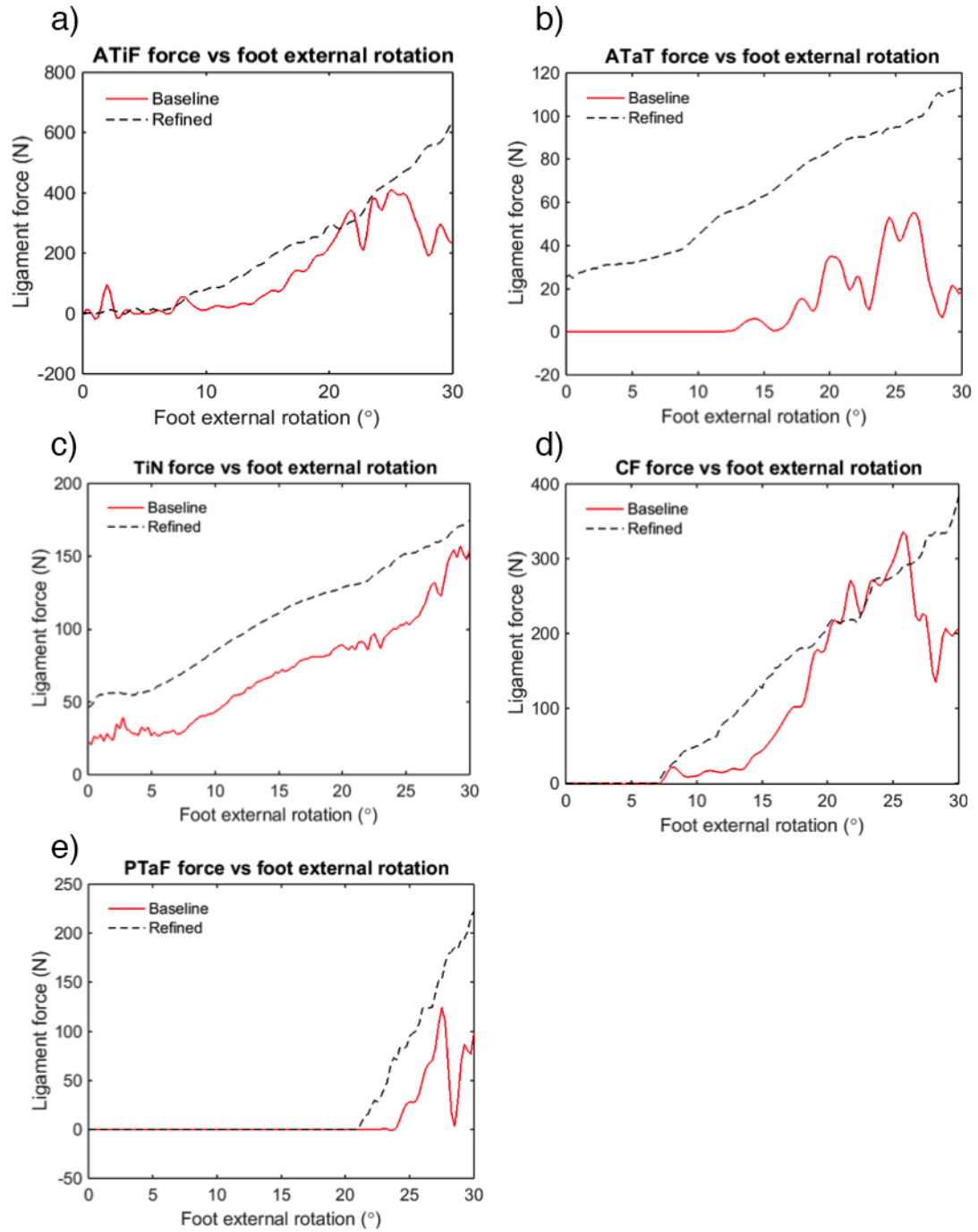


Figure 24. Ligament force responses of the baseline and refined models. Ligament force is the sum of forces in all fibers.

2.3.3 Discussion

The hypothesis for this study was that representation of articular cartilage will result in more physically realistic bone kinematic responses during external rotation of the foot in terms of smoothness of the responses (smoothness is defined in Section 2.3.2). Gaps at bone interfaces in the baseline model cause mechanical chatter of the talus. The results show that representation of articular cartilage in the refined model reduces this chatter and leads to smoother joint motion.

Gross moment, talus kinematic and ligament force responses

Preliminary structural-level validation was done using the response data from PMHS tests by Mait et al. (2015) (Figure 21) since they employed the same boundary conditions as the model. Other experimental studies applying external rotation to the foot constrained calcaneus translation as well as the fibula motion (Chen, Siegler, & Schneck, 1988; Johnson & Markolf, 1983; Wei et al., 2012), which was found to artificially constrain the talus in preliminary simulation analysis.

Healthy articular cartilage surfaces are smooth, and their interfaces have some of the lowest known coefficients of friction (on the order of 0.01) (Fung, 1993). Therefore it is expected that *in situ* bone kinematic and ligament responses under quasi-static loads should be smooth, and this has been demonstrated in PMHS tests (Chen et al., 1988; Johnson & Markolf, 1983; Siegler et al., 1988; Wei et al., 2012). In this study, the refined model responses were substantially smoother, and therefore more physically realistic, than the baseline model responses. Mechanical chatter of the bones in the baseline model was caused by repeated hard bone-to-bone contact. One prominent event in the baseline model occurred at 26.5° of foot external rotation (Figure 22 and Figure 23). Although it appears like a failure response, it was actually a hard contact impingement of the talus between the calcaneus and tibia, which caused a sudden shift of the talus. This resulted in a sudden drop in the gross moment response (Figure 21) and large changes in ligament force (Figure 24). Thus, the results support the hypothesis for this study since the representation of articular cartilage prevents rigid bone-to-bone impact and produces smoother, more physically realistic responses.

Limitations and future work

Bone and cartilage geometry for the same subject were not available, so cartilage geometry from a different dataset (Millington et al., 2007) was used. Despite this limitation, the cartilage parts were adequate for this study since they covered all bone-to-bone contact interfaces in the ankle and subtalar joint. Viscoelastic and fluid flow effects in the cartilage (Mow et al., 1984) were excluded since the focus of this study was to obtain more physically realistic bone kinematic responses by reducing gaps between articular surfaces rather than to obtain detailed time-dependent stress and strain distributions in the cartilage.

2.4 Discussion and conclusion

The refined model was created from the UVA Ankle model by updating the representation of ligaments. The ankle ligaments were modeled as distributed springs, which is physically more realistic than the single spring representation in the UVA Ankle model. Each spring represents a bundle of fibers and a bilinear stiffness curve was assigned to each fiber bundle.

The refined model was parameterized using the zero-force toe region and the number of fibers in a ligament. The linear stiffness was the same for all fibers in all ankle ligaments. The linearized ligament stiffness values reported by Funk et al. (2000) were used as the nominal ligament stiffness values. These were obtained by varying the number of fibers in each ligament. The toe region was the same for all fibers in a ligament, but varied from one ligament to another.

Articular cartilage was represented in the refined model (Section 2.3). Previous computational ankle models have ignored articular cartilage since they focused largely on gross ankle mechanics (Tannous et al. 1996; Beillas et al. 1999; Gabler et al. 2014). The representation of articular cartilage reduced the gaps between the ankle bones in the refined model and resulted in bone kinematics that were physically more realistic compared with those of the baseline model. This fulfilled Objective 4

The refined model can be used to gain insights into *in situ* ligament mechanics, which is the overall objective of this thesis. The next chapter describes how the refined model was optimized to achieve the objective of evaluating the model against the response of cadaver ankles.

Chapter 3

Optimization of the refined model

This chapter discusses the use of the fiber and ligament parameters in the refined model as design variables (DVs) in a sensitivity study (Section 3.2). The sensitivity analysis was performed to determine the variables that had the greatest influence on the bone kinematic responses of the model. The most sensitive variables were optimized to meet the evaluation targets for the bone kinematics (Section 3.3). The gross moment responses of the model were also evaluated against experimental data. Model evaluation at the level of bone kinematics represents an advancement over existing computational models of the ankle that have focused largely on gross structural level validation. The bone kinematics of the optimized model can be used to infer *in situ* ligament behavior, which was one of the objectives of this thesis.

3.1 Introduction

The refined model was parameterized as described in Section 2.2.2. The 20 parameters (Table 5) composed a 20-vector variable $X = (x_1, \dots, x_{20})$. These were the DVs for the sensitivity study. The methods and results sections of the sensitivity (Section 3.2) and optimization (Section 3.3) have been reported in the literature (Nie et al., 2015, 2016).

3.2. Sensitivity of design variables

3.2.1. Methods

Simulation setup

External rotation was applied to the calcaneus at an angular velocity of $10^\circ/\text{s}$. This was accomplished by fixing all 6 degrees of freedom (DOF) of the proximal tibia and applying Z-axis external rotation to the calcaneus up to 30° , which was considered to be a non-injury range of ankle motion (Siegler et al. 1988). Other DOF of the calcaneus were either fixed (Z-axis translation, X- and Y-axis rotation) or free (X- and Y-axis translation). The other three bones, the fibula, talus, and navicular, were free in all six DOF so that the motion was dictated by the ligaments. The kinematics of the ankle bones were measured as intrinsic yaw, pitch and roll angles of the local coordinate systems at 30° of calcaneus rotation relative to the orientation of the bone local coordinate system at the start of the simulation (described in Section 2.1 and Section 2.3.1).

Table 5. Design variables definition and range selection of the parametric ankle model.

Ligament/IOM list		No. (<i>i</i>)	Design variable (DV) ($x_p, p = 1, \dots, 20$)			
			Toe region (c_i) (mm)		Fiber number (n_i)	
			Lower bound	Upper bound	Lower bound	Upper bound
Deltoid	ATaT	1	0	10.4	3	12
	PTaT	2	0	6.0	21	82
	CT	3	0	11.4	8	30
	TiN	4	0	16.6	1	4
Lateral	ATaF	5	0	8.3	2	9
	PTaF	6	0	12.5	19	77
	CF	7	0	7.6	12	46
High ankle	ATiF	8	0	8.3	38	152
	PTiF	9	0	7.4	31	126
IOM	Fibers	10	-	-	10	100
	Skewness		-	-	1	1.2

Algorithm of the sensitivity study

Nie et al. (2015) described the algorithm used for the sensitivity study. The Latin Hypercube (LH) was chosen as the sampling scheme for the sensitivity study. The LH algorithm was first introduced as a statistical method to generate a stratified sample of parameter values from a multi-dimensional distribution (McKay, Beckman, & Conover, 2000). As a structured quasi-random sampling strategy, the Latin Hypercube can generate random sample points ensuring that all portions of the vector space are sampled, and potentially nonlinear input and output relationships can be represented in resulting response surfaces (Neal, Tu, & Jones, 2008; Neal, 2004). Assume that N sample points were to be determined for the s -vector variable $X = (x_1, \dots, x_s)$, which was composed of all the DVs. Then the range of each x_p was divided into N equally probable intervals and sampled once from each interval. Let this sample be x_{pt} ($t = 1, \dots, N$). For the x_p ($p = 1, \dots, s$) component in X_t ($t = 1, \dots, N$), the components of the various x_p 's were matched at random. One of most recent LH techniques, the maximin design, sought to maximize the minimum statistical distance between model inputs to increase the multidimensional uniformity (Johnson et al. 1990). The maximin LH design implementation by Carnell was used in this study (Carnell 2009) to generate 1000 sampling points ($N = 1000$). Simulations with the resultant models were conducted, and all the runs were normally terminated. The computation time of each simulation was approximately 7 min on a Xeon E5-1620 processor with 3.60 GHz frequency using the LS-DYNA solver version R7.1.1.

Each model response was taken as a multivariate linear regression model, y_r , with r indicating the number of the model response, i.e. $r = 9$. For each DV x_p , the regression coefficients, b_p ($p = 1, \dots, s$), were calculated as

$$y_r = b_0 + \sum_{p=1}^s \frac{b_p}{\Delta x_p} x_p = b_0 + \frac{b_1}{\Delta x_1} x_1 + \frac{b_2}{\Delta x_2} x_2 + \dots + \frac{b_s}{\Delta x_s} x_s$$

Δx_p is the range of the DV. The DVs were normalized by the range so that the units of all the regression coefficients were consistent. The regression coefficients showed the influence of each DV on the individual model response. A positive correlation meant a higher DV value would result in a larger value of the response and vice versa.

Linear ANOVA was used to evaluate significance of the DVs at a confidence level of $\alpha = 0.05$ (Myers, Montgomery, & Anderson-Cook, 2016; Stander, Roux, Eggleston, & Craig, 2007). This approach was used to verify statistical significance of the DVs assessed using p values. The $100(1-\alpha)\%$ confidence interval for each DV was defined as

$$b_p - 0.5\Delta b_p \leq \beta_p \leq b_p + 0.5\Delta b_p$$

$$\Delta b_p (\alpha) = 2t_{\alpha/2} \sqrt{\sigma^2 C_{pp}}$$

β_p is the range of values of the regression coefficient b_p within the confidence interval. $t_{\alpha/2}$ is the Student's t- distribution, σ^2 is the variance, and C_{pp} is the diagonal element of the inverse of the moment matrix (Myers et al., 2016; Stander et al., 2007). If the following is true:

$$b_p \geq 0.5\Delta b_p$$

then $\beta_p \neq 0$ at a confidence level of α . This implies that the corresponding DV is significant at a confidence level of α (Figure 25).

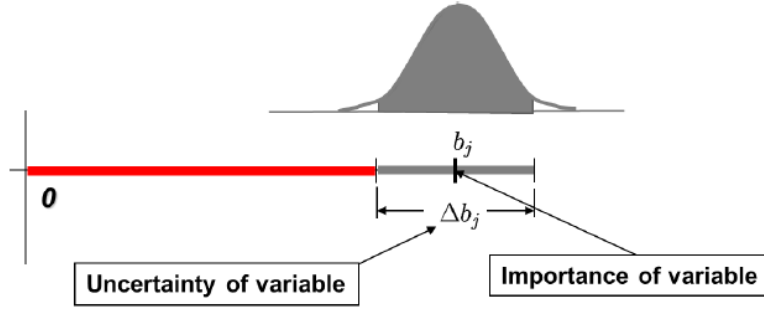


Figure 25. The $100(1-\alpha)\%$ confidence interval determines the significance of the regression coefficient.

The accuracy of the regression model was evaluated using the coefficient of multiple determination, mR^2 .

$$mR^2 = \frac{\sum_{t=1}^N (\hat{y}_t - \bar{y}_t)^2}{\sum_{t=1}^N (y_t - \bar{y}_t)^2}$$

y is the response of the FE model, \hat{y} is the predicted response of the regression model, t is the index representing a sample with a total of N samples.

3.2.2. Results of sensitivity analysis

During in-plane rotation loading around the Z-axis of the tibia, six DVs with the highest sensitivity were plotted for each of the nine rotation angles (Figure 26). The regression coefficients, confidence intervals, p values for the six most sensitive DVs, and quantile-quantile plots of the residuals versus standard normal samples for each response are provided in Appendix 1. For the fibula, the yaw angle was of the largest magnitude among the yaw-pitch-roll angles. The most significant DV for the yaw angle was the toe region of ATiF, $c_i(\text{ATiF})$, with a regression coefficient of -14.94° . The second most significant DV turned out to be the toe region of PTaF, $c_i(\text{PTaF})$, which exhibited a regression coefficient of 9.62° . Similarly, for the talus, $c_i(\text{PTaF})$ was the most significant variable for the yaw angle with a regression coefficient of -10.54° . $c_i(\text{PTaT})$ and $c_i(\text{ATiF})$ exhibited the highest influence on the pitch and roll angle. For the navicular, a relatively large roll angle was noticed, and the most significant DV was $c_i(\text{TiN})$, with a positive coefficient of 6.36° . The regression coefficients for which $b_p \geq 0.5\Delta b_p$ were statistically significant. These are marked with a * symbol in Figure 26. Statistical significance evaluated using this approach agreed with the statistical significance obtained from p values. The fibula roll regression model was most accurate and the talus roll regression model was least accurate (Table 6). A representative table of regression coefficients, confidence intervals, and p values for the six

most sensitive DVs of the talus yaw model is reported (Table 7). Quantile-quantile (QQ) plot for the talus yaw response shows good qualitative agreement with the standard normal distribution (Figure 27).

Table 6. Accuracy of the regression models. mR^2 is the coefficient of multiple determination,

Model response		mR^2
Fibula	Yaw	0.897
	Pitch	0.746
	Roll	0.902
Talus	Yaw	0.764
	Pitch	0.761
	Roll	0.632
Navicular	Yaw	0.789
	Pitch	0.664
	Roll	0.792

3.2.3. Discussion

Implications of the sensitivity analysis

The most important outcome of the sensitivity analysis was that the three most significant and sensitive DVs for each response were toe regions. As shown in the sensitivity results, the toe regions proved to exhibit a significant influence on the bone kinematics. Interestingly, the DVs representing ligament stiffness, n_i , were found to be relatively insignificant on the bone angles, e.g. no n_i was among the five most significant DVs in the sensitivity analysis of the fibula angles (Nie et al., 2016).

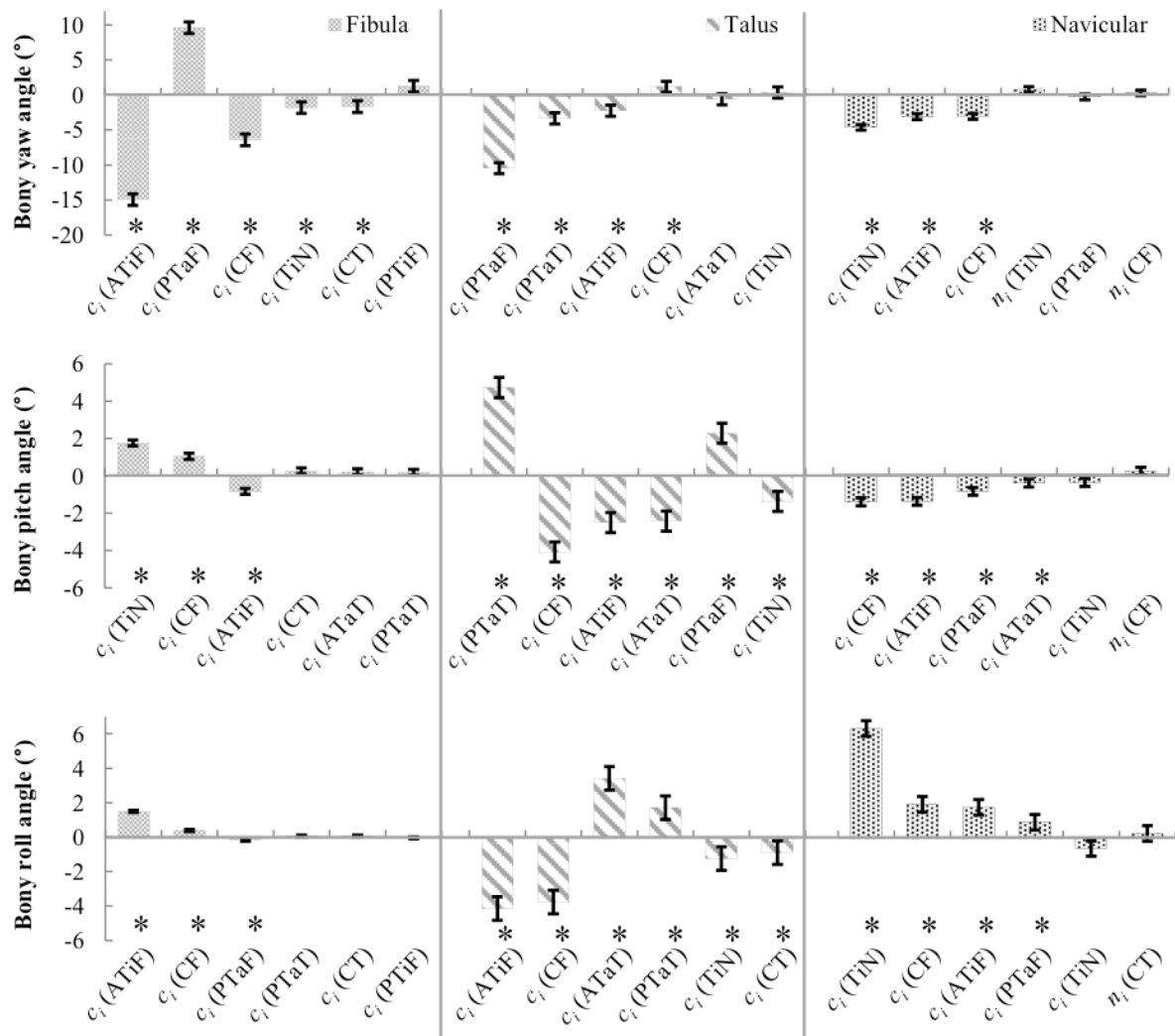


Figure 26. Sensitivity analysis on the yaw-pitch-roll angle during of the fibula, the talus, and the navicular during the in-plane rotation around the Z-axis of the tibia. The * symbol represents regression coefficients that are not statistically significant.

Table 7. A representative table of regression coefficients, confidence intervals, and p values for the six most statistically significant DVs (based on p values) of the talus yaw model.

Design variable	Regression coefficient	Confidence Interval (lower)	Confidence Interval (upper)	Confidence interval	p value
c_i (PTaF)	-10.50	-10.90	-10.20	0.70	8E-284
c_i (PTaT)	-3.31	-3.71	-2.91	0.80	6.3E-53
c_i (ATiF)	-2.20	-2.60	-1.80	0.80	5.6E-26
c_i (CF)	1.26	0.86	1.66	0.80	8.5E-10
c_i (ATaT)	-0.54	-0.94	-0.14	0.80	0.008
c_i (TiN)	0.45	0.05	0.85	0.80	0.0287

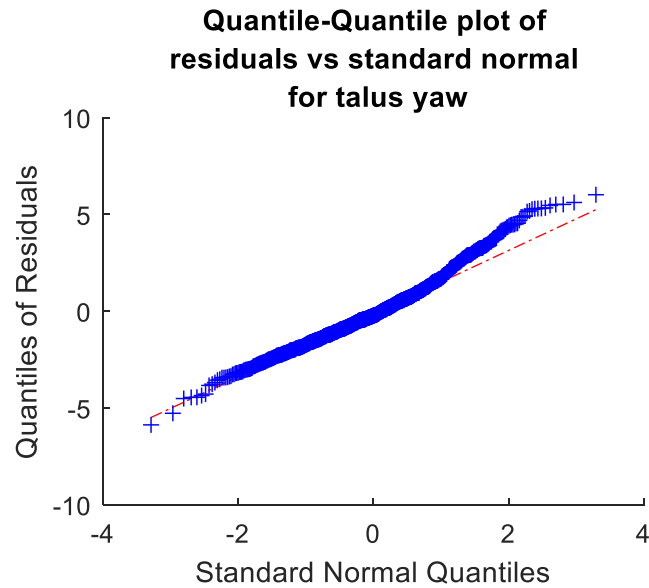


Figure 27. A representative quantile-quantile (QQ) plot of residuals vs standard normal samples for the multivariate linear regression model. The QQ plot for the talus yaw regression model is shown here.

The fibula yaw and roll responses had an mR^2 value greater than 0.89 which is a good fit. The mean mR^2 value for all responses was 0.772, which suggests that the accuracy of some of the regression models can be improved. The bilinear fiber stiffness representation introduces some nonlinear effects into the relationship between the bone kinematics and DVs in the FE model. However, a qualitative assessment of the QQ plots (appendix 1) showed that the distribution of the residuals was close to a standard normal distribution.

Sample size and design variable ranges

With a total of twenty DVs included in the DOE, a high sample size, N , is required in order to maintain the level of statistical power (Collins, Dziak, & Li, 2009). Therefore, 1000 simulations were conducted to explore the whole design space. The sensitivity analysis was related to the DV selection and their range, as well as the loading conditions. The relatively large DV range (Table 5) was determined to account for as many model responses as possible under the given loading conditions. A wide range of the DVs representing the toe region was included to reflect the genetic variability of the ligament, and the range reported by Nigg et al. (1990). The DV selection, the effective DV range, and the descriptive capability of the model requires interpretative knowledge of the mechanics of the ankle structures and judgement specific to its application field. For the optimization study described in the next section, only significant DVs with limited range were used. For future work, to assess the effect of the range of the DVs on the sensitivity rankings, the sensitivity rankings obtained using a different range of the DVs can be compared with the sensitivity rankings obtained in this section. This was not necessary in the present study as the model evaluation targets were met by optimizing the FE model using the most sensitive DVs (Section 3.3).

3.2.4. Conclusions

The sensitivity study described in Section 3.2 explored the relationships between the gross foot and ankle behavior and the underlying bone and ligament mechanics. Ligament laxity and uncrimping behavior were represented by a composite *in situ* toe region at the fiber level. The DVs for the sensitivity study were the *in situ* fiber toe regions, the number of fibers (which represented ligament stiffness) and the skewness of the IOM. The sensitivity of the bone kinematics to the DVs was investigated by conducting a 1000-case design of experiment study. The *in situ* fiber toe regions exhibited a statistically significant effect on the bone kinematics, and the stiffness values were found to be relatively insignificant (Nie et al. 2016). *In situ* toe regions are often neglected in computational ankle models (Wei et al. 2011). The high sensitivity of the bone kinematic responses to the toe regions suggested that *in situ* toe regions should be represented in computational ankle models to study bone kinematics and *in situ* ligament mechanics. The sensitivity study was an intermediate step that showed that the design space could be reduced for

the model optimization (described in the next section). This facilitated the representation of salient features of *in situ* ligament stiffness curves (Objective 3) and the kinematics of individual bones (Objective 5), as described in the next section.

3.3. Optimization of *in situ* fiber toe regions

3.3.1. Methods

The number of DVs for the optimization study was reduced based on the results of the sensitivity study (Section 3.2.2). The results of the sensitivity study showed that the toe regions were the most sensitive DVs. Therefore, only the toe regions were optimized. This reduced the number of DVs for the optimization study from 20 to 9. The 9 DVs formed a 9-vector variable $X = (x_1, \dots, x_9)$. The value of each DV, x_p ($p = 1, \dots, 9$), was identified by matching the bone kinematic responses predicted by the model with the experimental data through an optimization approach that consisted of an outer loop and four independent sub-optimizations within the outer loop (Figure 28). Each sub-optimization used a different single rotation of the foot. The sub-optimizations were recorded as $\text{sopt}(m)$ ($m = 1, \dots, 4$), and the calcaneus rotation inputs for the four sub-optimizations were external rotation, internal rotation, eversion, and dorsiflexion. The results of the optimization routine were the optimal *in situ* fiber toe regions.

Bone kinematics obtained from cadaver ankle experiments

A description of the experimental setup used to obtain bone kinematics under external rotation of the foot was reported by Mait et al. (2015). The lower extremities from three human cadavers (mean age, 42 years; range, 31-47 years) were disarticulated at the knee taking care to retain the proximal ligaments between the tibia and fibula. The proximal portion of the tibia was potted and then rigidly constrained while the motion of the fibula was dictated only by its connective tissue and articulation with other bones (i.e., the fibula was not potted). The calcaneus was potted and installed in a jig that allowed it to translate in the transverse plane (i.e., along the X and Y axes, Figure 29). The foot was positioned in a neutral orientation, and the calcaneus was subjected to quasi-static rotation for producing a single rotation of the foot; the rotation could be external rotation, internal rotation, eversion, or dorsiflexion. Multiple rotations were achieved by subjecting the foot to different rotations in sequence, such as eversion followed by external rotation (Table 8). The multiple rotation cases were used for evaluating the model. Aluminum cubes were mounted via screws to the ankle bones including the tibia, fibula, talus, calcaneus and navicular. Local Coordinate Systems (LCSs) were defined for each bone as described in Section 2.1, and the tibia coordinate system served as the global reference frame. The kinematics of the fibula, talus, navicular, and calcaneus, relative to the tibia coordinate system, were calculated. Bone rotations

were calculated as yaw, pitch, and roll angles using the intrinsic Euler angle description (Shabana, 2013; also described in Section 2.3.1). The x, y, and z displacements (referred to as Δd_x , Δd_y , and Δd_z) were calculated relative to the bone position at the start of the test when the foot was in neutral.

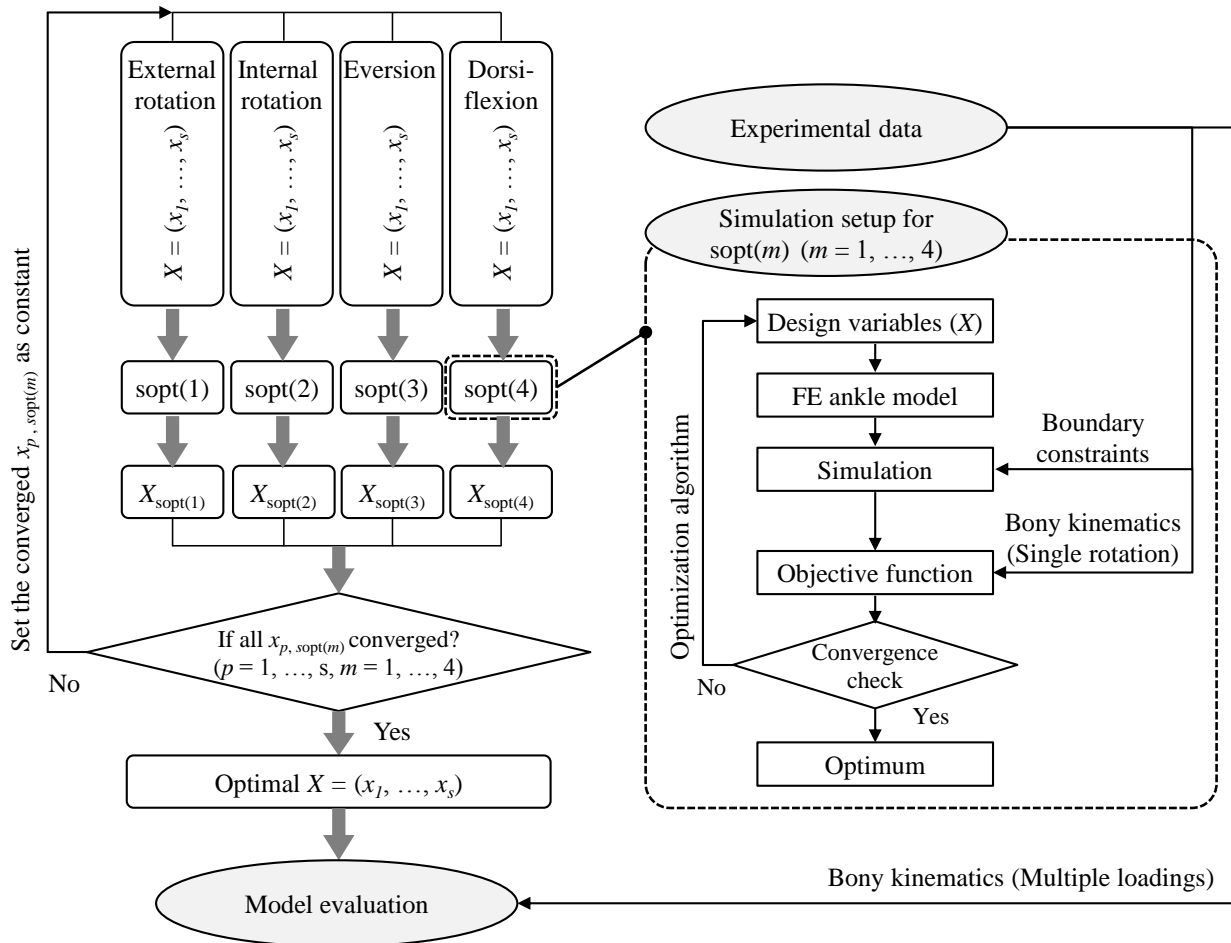


Figure 28. Flowchart of the optimization for determining *in situ* ligament properties (Nie et al. 2016).

Specimen 743L was chosen as the experimental basis for the model optimization since the shapes of the bones, particularly the talus, were qualitatively closest to those in the model. The deviations of the maximum and minimum values among the three cadaver specimens from the mean response of the three specimens were used as the positive and negative experimental ranges for each response. These ranges reasonably represented the biological variance of the population.

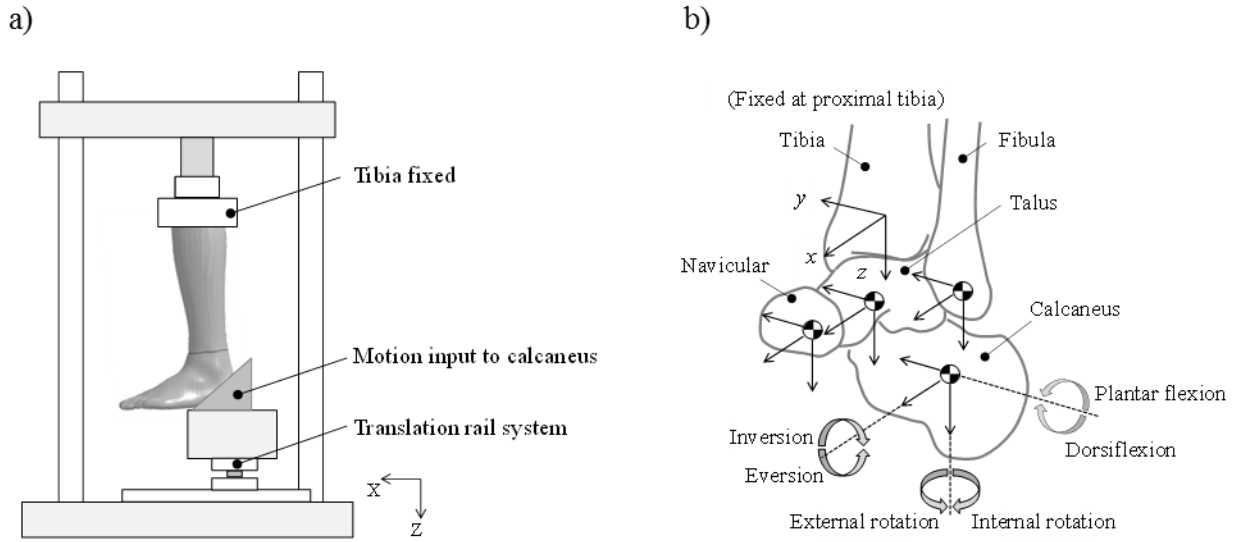


Figure 29. a) Schematic of the experimental test rig (Mait et al. 2015). b) The Local Coordinate Systems (LCSs) defined for the bones (a left foot is shown) (Nie et al. 2016).

Table 8. Experimental loading conditions and the input rotation angles of the calcaneus used for model optimization and evaluation purpose (subject 743L).

Loading conditions	Single rotation (For model optimization)				Multiple loadings (For model evaluation)	
	External rotation	Internal rotation	Eversion	Dorsiflexion	Eversion+ External rotation	Dorsiflexion+ External rotation
Rotation angle of the calcaneus (°)	21	25	11	17	11 + 21	17 + 23

Model optimization and evaluation setup

The experimental setup was replicated using the FE ankle model in LS-DYNA. The proximal end of the tibia was fixed in space in all degrees of freedom, and the calcaneus was positioned to match each experimental condition. Continuous rotation was applied to the calcaneus to enforce a prescribed rotation at 10°/s to the angle measured in the experiments (Figure 29, Table 8). The fibula, talus, and navicular were free in all six degrees of freedom so that their motion was dictated by the relevant connective tissues and articulations with other bones. The resultant yaw-pitch-roll angles were calculated using the intrinsic Euler angle description (Shabana 2013; also described

in Section 2.3.1). The x, y and z displacements of the fibula, talus and navicular were calculated relative to the position of the bone at the start of the simulation. A total of nine angles and nine displacements (three angles and three displacements for each of the three bones), defined analogously to the experiments, were available as the model responses.

Within each ligament, the average length of the bundle of fiber elements was used to represent the initial length, $l_{0,i}$. The searching range of the toe regions (c_i) was set by scaling the initial ligament length, $l_{0,i}$, from 0 to 0.2 as a reasonable approximation. The 9 DVs, x_p ($p = 1, \dots, 9$), formed a 9-vector variable $X = (x_1, \dots, x_9)$ which was modified by the optimization routine.

A genetic algorithm was used as it can provide reasonably accurate solutions to global optimization problems (Simpson et al. 2001). This algorithm was implemented for each sub-optimization. For the first iteration, the algorithm selects a ‘population’ of five random samples. The samples chosen for subsequent iterations are ‘descendants’ of the previous population. The objective function (Opt_{error}) to minimize was defined as the sum of the root mean squared error of the nine angles and nine displacements of the bones. The objective function is a measure of the difference between the bone kinematic responses of the model and the experiments.

$$\text{Opt}_{error} = \frac{\sqrt{\frac{1}{9} \sum_{r=1}^9 (\text{Angle}_{model,r} - \text{Angle}_{experiment,r})^2}}{\overline{\text{Angle}}} + \frac{\sqrt{\frac{1}{9} \sum_{r=1}^9 (\Delta d_{model,r} - \Delta d_{experiment,r})^2}}{\overline{\Delta d}} \quad [2]$$

where r is the number of the bone angle, i.e. $r = 9$. $\overline{\text{Angle}}$ and $\overline{\Delta d}$ denoted the mean value of the experimental data. The angle and displacement root mean squared terms were non-dimensionalized using $\overline{\text{Angle}}$ and $\overline{\Delta d}$ so that these terms could be summed to obtain a single non-dimensional term for the objective function. It was possible for the value of Opt_{error} to be greater than unity since the root mean squared term (numerator) could be greater than the mean experimental value. The optimization was performed using LS-OPT 5.1.0 (LSTC 2014).

Convergence checks were performed at the level of the outer loop and for each sub-optimization. The convergence check within each sub-optimization was based on the value of the objective function. A small tolerance value of 0.01 was used and the maximum number of iterations was set to 10. While, the sub-optimizations reduced the value of the objective function, due to the small tolerance value, almost all sub-optimizations executed the maximum number of iterations and did not converge based on the value of the objective function. At the level of the outer loop, convergence of the model was determined based on the values of the DVs. For a given DV, x_p , if the values from all the sub-optimizations were within $0.05\Delta x_p$, (where Δx_p is the DV range), that DV was fixed for the next iteration of the outer loop. This check on the convergence of the DVs emphasized uniqueness of the DVs (within a 5% range) across sub-optimizations.

The total number of iterations (after multiple iterations of the outer loop) ranged from 156 for the external rotation sub-optimization to 164 for the internal rotation sub-optimization. The mean

decrease in the value of the objective function was 5.6 (Table 9). The values of all the toe regions were zero for the first iteration.

Table 9. Values of the objective function at the initial and final iteration.

Sub-optimization with single rotation loading	First iteration	Final iteration
External rotation	6.2	1.6
Internal rotation	7.4	2.7
Eversion	8.2	2.0
Dorsiflexion	8.5	1.7

Simulations under the two multiple rotations were conducted to evaluate the optimized ankle model (Table 8). The nine angle responses and nine displacement responses of the bones were evaluated against cadaver ankle responses.

3.3.2. Results

The talus and fibula orientation responses of the optimized model under external rotation were more similar to those observed in the experiments compared with the orientation responses of the initial model (Figure 30). Talus yaw and pitch showed the greatest improvement. The bone orientations of the optimized model showed good agreement in general with the experimental data under single rotations of the foot, i.e., external rotation, internal rotation, eversion and dorsiflexion (Figure 31). The model responses were within 2° and 2 mm of the experimental ranges for most responses (exceptions are discussed in Section 3.3.4).

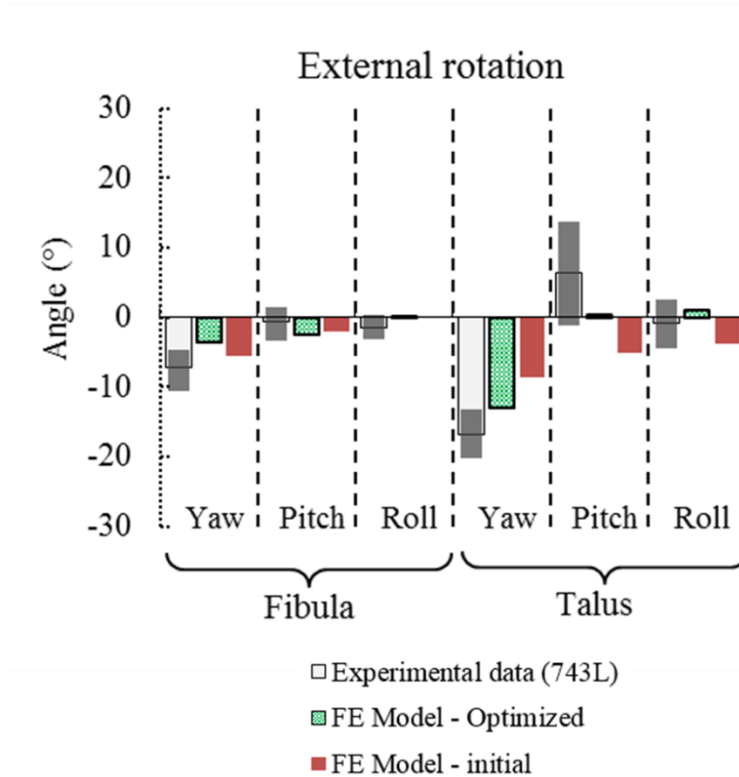


Figure 30. The orientations of the talus and fibula of the optimized model are closer to the experimental response of specimen 743L. The range of the other two cadaver specimens is shown with the responses of specimen 743L.

The absolute values of the optimized *in situ* fiber toe regions ranged from 0.4 mm to 4.1 mm, and the relative length ranged from 0.9% to 14.7% (Table 10). The toe regions obtained enabled a representation of *in situ* ligament stiffness curves that included *in situ* slack, nonlinear stiffening and linear stiffness regions (Figure 32), which was an objective of this thesis (Objective 3).

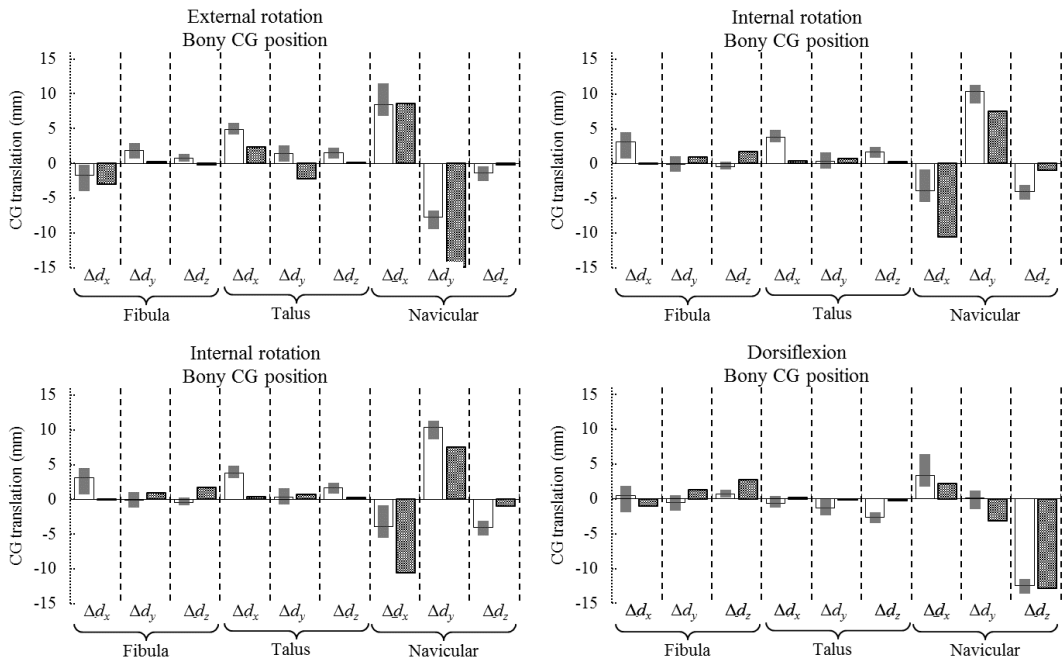
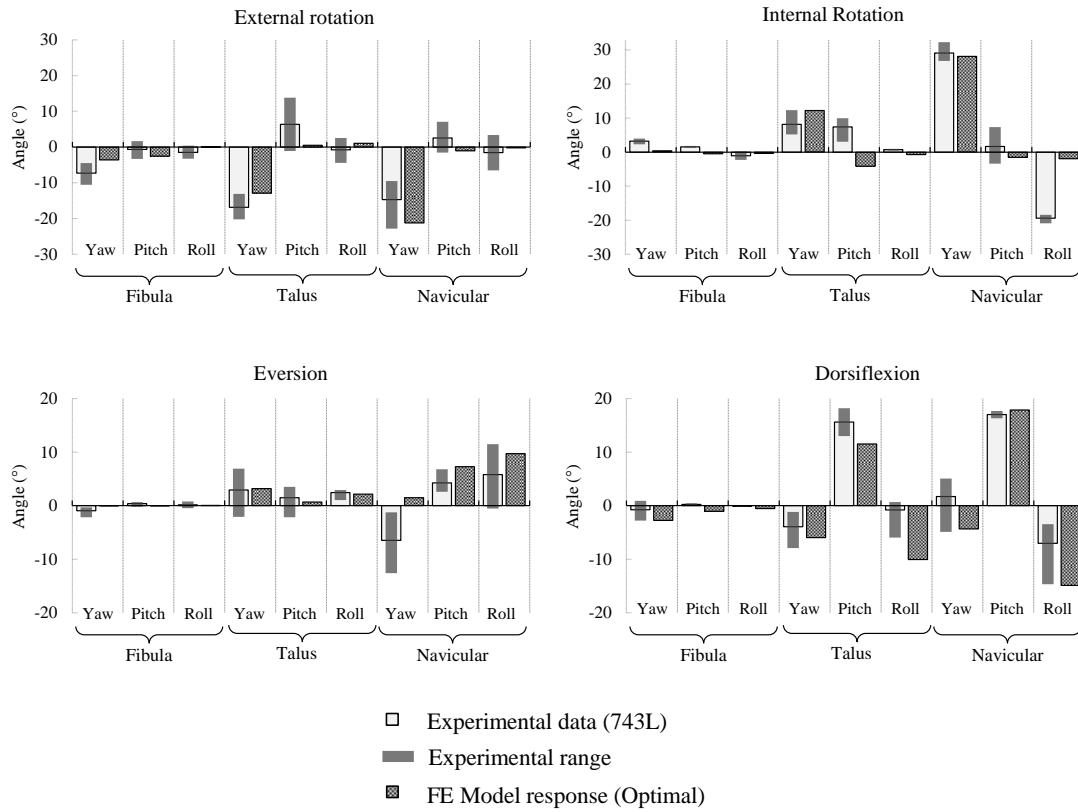


Figure 31. Comparison of the bone angles and displacements of the experiments and the optimized model on single rotations of the foot (model optimization) (Nie et al. 2016).

Table 10. Optimized *in situ* toe regions of fibers of ankle ligaments. The relative length of the toe region was determined as its ratio relative to the initial ligament length (Nie et al. 2016).

Ligament list			Initial length	Toe region		Linear stiffness (from lit.)
			$l_{0,i}$	c_i	c_i	$K_i = k^*(n_i)$
No. (i)			(mm)	(Optimum) (mm)	(Optimum, relative length)	(N/mm)
Deltoid (Medial)	ATaT	1	21	0.9	4.5%	125
	PTaT	2	12	1.8	14.7%	826
	CT	3	23	2.3	10.3%	302
	TiN	4	33	4.1	12.5%	39
Lateral	ATaF	5	17	0.1	0.9%	89
	PTaF	6	25	1.6	6.5%	770
	CF	7	15	0.7	4.5%	452
High ankle	ATiF	8	17	1.3	7.9%	1516
	PTiF	9	15	0.4	2.6%	1258

3.3.3 Model evaluation

The peak moments applied at the calcaneus in the optimized model agreed well those measured experimentally (Figure 33). For the eversion + external rotation input case, the moment in the optimized model (30.2 Nm) was very close to that obtained from specimen 743L (29.6 Nm) and within the experimental range. For the dorsiflexion + external rotation input, the moment in the optimized model (34.3 Nm) exceeded the maximum value in the experimental range by 3.7 N m.

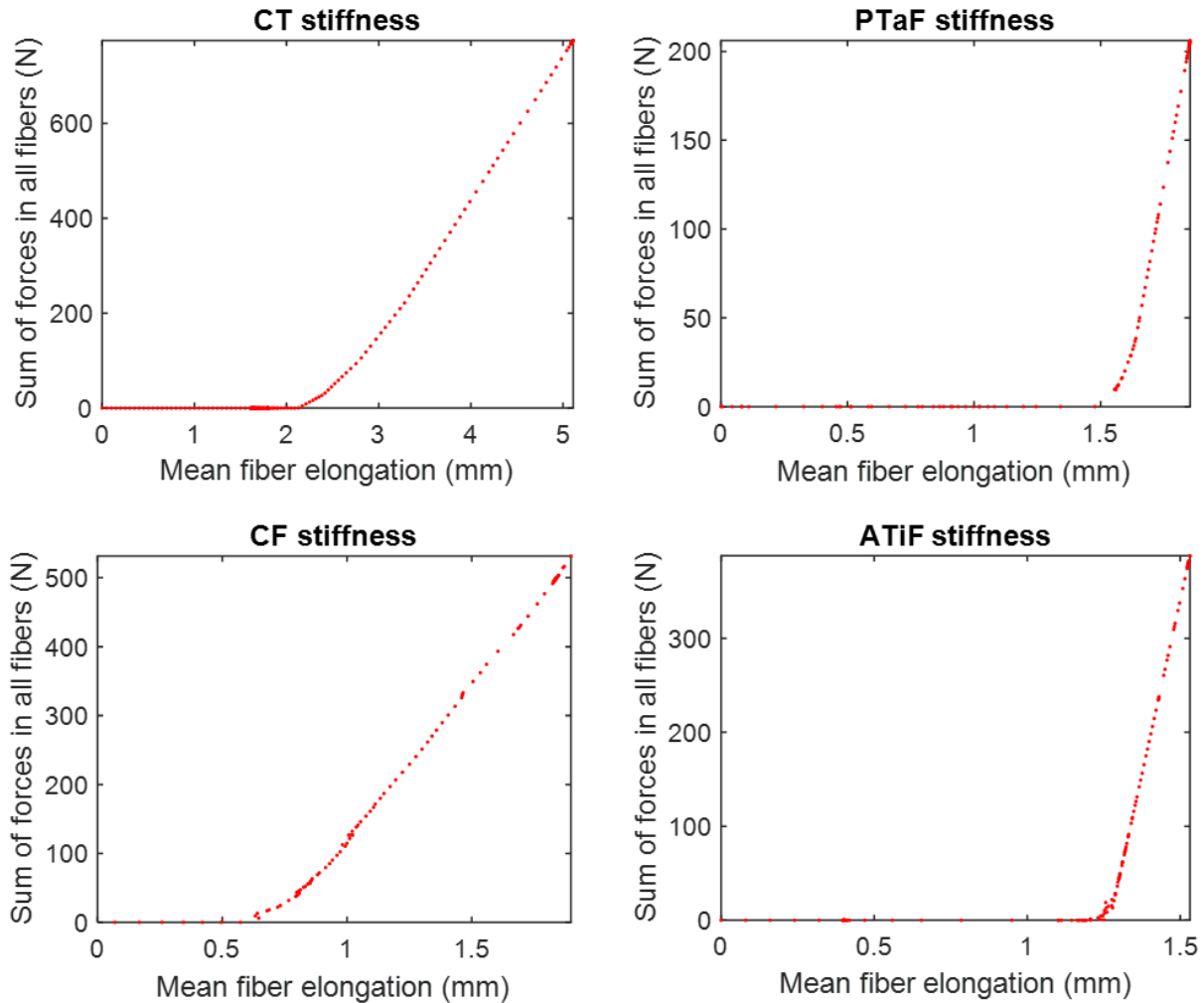


Figure 32. *In situ* ligament stiffness curves of the CT, PTaF, CF and ATiF from the FE model under external rotation of the calcaneus relative to the tibia. The PTaT, ATaF, and PTiF were not loaded under an external rotation input.

For the multiple rotation cases, the bone orientations and positions predicted by the model were close to the experimental range (Figure 34). The bones in the optimized model moved in the same directions as those in the cadaver ankles. These results strongly suggest that the bone kinematics of the optimized model are reasonable. In Table 11, the mean deviations of the model responses from the experimental range are presented to compare them to the evaluation targets.

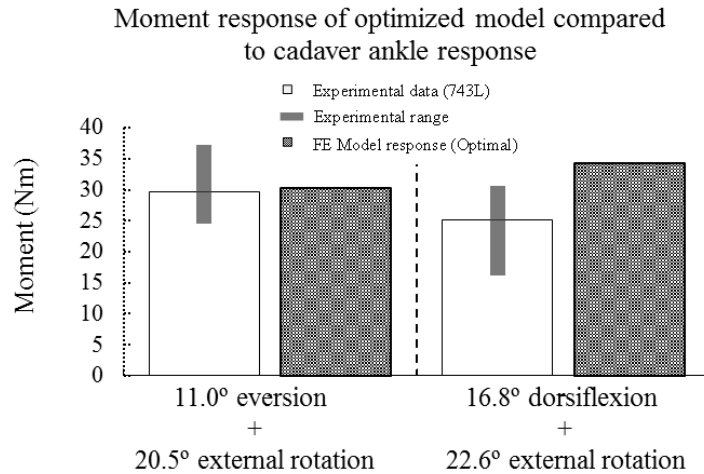


Figure 33. Comparison of the rotation moments (applied at the calcaneus) recorded in the experiments to those obtained from the optimized model for the multiple rotation cases.

3.3.4. Discussion

In situ fiber toe regions and ligament stiffness curves

The *in situ* fiber toe regions, which are a part of the *in situ* mechanical behaviour of ankle ligaments, were reported in Section 3.3. To the best of the author's knowledge, *in situ* fiber and ligament toe regions for ankle ligaments have not been reported in the literature, and therefore, there are no previous results for comparison with the obtained toe region results. Li et al. (1999) developed a computational model of the human knee and reported the *in situ* slack lengths of 12 ligament bundles for the knee in extension. The absolute values of slack length had a mean of 1.0 mm and range of 0.0 to 3.0 mm. The slack length relative to ligament initial length ranged from 0-10% (Blankevoort & Huijskes, 1996; Li et al., 1999). Thus, the absolute and relative fiber toe regions obtained in the optimized model were within 1.1 mm and 2.5% of the values reported in the literature for knee ligaments.

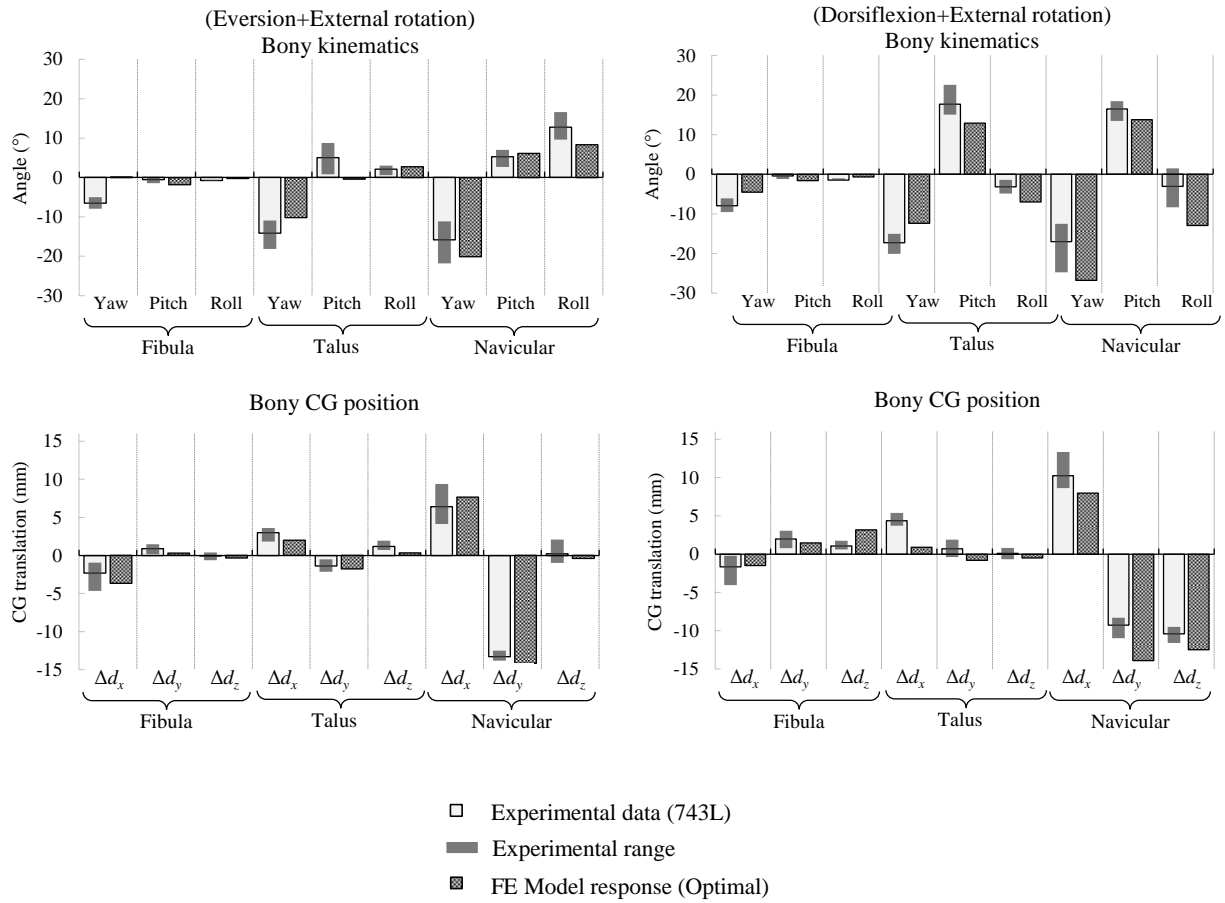


Figure 34. Comparison of the bone kinematics of the experiments, with the responses predicted by the optimized model for the multiple rotation (model evaluation) cases (Nie et al. 2016).

Table 11. Deviations of model responses from experimental ranges.

Rotation input	Mean deviation of bone kinematics from experimental range		Deviation from experimental range
	Orientation (°)	Position (mm)	Gross moment (Nm)
11.0° eversion + 20.5° external rotation	0.9	0.1	0.0
16.8° dorsiflexion + 22.6° external rotation	1.7	1.1	3.7

The stiffness curves obtained from the optimized model (Figure 32) represented the three regions of *in situ* ligament stiffness curves (Figure 11) (Kastelic et al., 1980; Nigg et al., 1990). Thus, the

objective of representing the salient features of ligament stiffness curves (Objective 3) was achieved. The smooth nonlinear stiffening region was obtained through superposition of forces in fibers that deform non-homogeneously. This showed that a bilinear representation of fiber stiffness gave a reasonable representation of *in situ* ligament stiffness curves. The stiffness curves of the ligaments in the anterior portion of the deltoid (TiN and ATaT) did not show nonlinear stiffening since these ligaments were represented by fewer fibers than other ligaments.

The ligament stiffness curves in the optimized model were a physically more reasonable representation of *in situ* ligament behavior compared with the representation of Wei et al. (2011), who used linear springs. The stiffness curves of Wei et al. (2011) passed through the origin since the toe region was not represented. The results presented here show that a relatively simple bilinear stiffness representation of fibers can produce physically realistic ligament stiffness curves and meet evaluation targets for the kinematics of individual bones and the gross moment response.

Model evaluation

The bone kinematic and gross moment responses of the optimized model met the evaluation targets for the multiple rotation cases (Table 11), satisfying Objective 5. The bone orientation responses for each of the single rotation inputs cases used to optimize the model (Figure 31) also met the evaluation target. An exception was the internal rotation input case, where the navicular roll deviated appreciably from the experimental range. When the navicular roll response was excluded, the mean deviation from the experimental range reduced from 3.2° to 1.5° , which was within the evaluation target of 2° (Objective 5a).

It may have been difficult for the algorithm to optimize navicular roll since only a single load path to the navicular (the TiN) was optimized. The navicular is connected to several other ligaments that transfer loads from the tarsals and the calcaneus that were not optimized. This may explain the deviation of the navicular roll response from the experimental range.

The peak moment responses met the evaluation target of being within 5 Nm of the experimental range (Figure 33). However, in the optimized model, the peak moment in the dorsiflexion + external rotation case compared with the eversion + external rotation case followed the opposite trend as that seen in the cadaver ankle experiments. Dorsiflexion may be an important mechanism for loading the ATiF (discussed later in Section 4.4). While the kinematic responses under dorsiflexion agreed well with experimental data, it is suggested that the dorsiflexion moment response be studied in future work to better understand the cause for its deviation from the experimental trend.

3.3.5. Summary

In Section 3.3, the refined model was optimized to characterize *in situ* fiber toe regions that are not readily observed in experiments. A relatively simple bilinear stiffness representation of fibers produced physically interpretable *in situ* ligament stiffness curves along with bone kinematic and the gross moment responses that met the experimental evaluation targets. Based on these results, the optimized model can provide insights into the relationship between gross ankle mechanics and *in situ* ligament mechanics, which is the overall objective of this thesis.

Chapter 4

In situ behavior of the anterior tibio-fibular ligament

4.1. Introduction

The previous chapters described the refinement and optimization of the UVA Ankle model. In this chapter, the optimized model was used to obtain insight into the *in situ* behavior of the ATiF. The motivation of this thesis was to understand the mechanism of syndesmotoc ankle sprains (the ATiF is one of the ligaments injured in such sprains). Knowledge of the relationship between sub-failure ligament mechanics and bone kinematics under gross rotations of the ankle can provide some insight into the injury mechanism. The objective of this chapter was to use the optimized model to describe the relationship between the total force in the ATiF and the kinematic responses of the talus and fibula for gross kinematic inputs to the calcaneus that are relevant to syndesmotoc ankle sprains.

External rotation of the foot relative to the tibia is considered the primary injury mechanism of many syndesmotoc ankle sprains (Nussbaum et al. 2001). Some studies have suggested that eversion and dorsiflexion also play a role (Nussbaum et al., 2001; Wei et al., 2012). Syndesmotoc ankle sprains have also been documented in studies investigating fibular fractures (Haraguchi & Armiger, 2009; Stiehl, Skrade, & Johnson, 1992). Haraguchi and Armiger (2009) showed that external rotation of the foot with the ankle in pronation produced ATiF injury with fibular fracture, followed by deltoid ligament injury using a rigid foot constraint. Stiehl et al. (1992) used a more compliant fiberglass cast tape restraint and documented ATiF injury in combination with fibular fracture.

Wei et al. (2012) reported that dorsiflexion and eversion followed by axial loading and external rotation of the foot generated isolated ATiF injury in all six cadaver ankles tested. This led to the hypothesis that “eversion... predisposes the ATiF to injury, forming a basis for syndesmotoc ankle sprains.” Wei et al. (2012) reported that the ATiF was predisposed to injury because eversion increased talus yaw magnitude, but the mechanism for the increase in talus yaw magnitude due to eversion was not clear. In this chapter, the optimized model was evaluated under four combinations of eversion, dorsiflexion and external rotation inputs to the calcaneus to gain insight into mechanisms that increased ATiF force.

In a clinical setting, ATiF injury is often diagnosed by evaluating the kinematics of the distal fibula (Beumer et al., 2009; Xenos, Hopkinson, & Mulligan, 1995). Radiographs are used to measure tibio-fibular diastasis, which refers to widening of the anterior syndesmosis (Kärrholm, Hansson, & Selvik, 1985). *In vivo* radiographic studies provide some understanding of bone kinematic patterns associated syndesmotoc sprains (Svensson, Lundberg, Walheim, & Selvik, 1989). The

optimized model can provide a more detailed description of the relationship between bone kinematics and ligament load patterns.

4.2. Methods

The boundary constraints for the calcaneus, and the proximal tibia and fibula were identical to the constraints applied for the model optimization study (Section 3.3.1) to keep the optimized model within its intended range of applicability. Briefly, all degrees of freedom of the tibia were constrained and all degrees of freedom of the fibula were free. Calcaneus translation was allowed in the X-Y plane but constrained in the Z direction, and combinations of rotation inputs were applied to the calcaneus (Table 12). In all cases, an axial load of 136.1 N was applied to the calcaneus in the $-Z$ direction before any rotation was applied.

Table 12. Abbreviations describing rotation inputs applied to the calcaneus.

Abbreviation	Rotation input applied to the calcaneus
ER30	30° external rotation
DF20+ER30	20° dorsiflexion followed by 30° external rotation
EV20+ER30	20° eversion followed by 30° external rotation
DF20+EV20+ER30	20° dorsiflexion followed by 20° eversion and 30° external rotation

Talus yaw rotation from the optimized model was compared to the experimental measurements of Wei et al. (2012) because Wei et al. (2012) reported that talus yaw was a mechanism that generated ATiF force. Talus pitch was evaluated since high magnitudes of this response were observed in the optimized model. The talus pitch and fibula yaw responses of the optimized model were evaluated since positive talus pitch and negative fibula yaw increase anterior tibio-fibular diastasis (Kärrholm et al., 1985). Wei et al. (2012) rigidly potted the proximal fibula which did not allow fibula translation in the Z direction (referred to as fibula Δz). However, fibula Δz has been reported *in situ* in cadavers (Mait et al. 2016) and living humans (Beumer et al. 2009). Therefore, translation in the fibula Δz degree of freedom was allowed in the optimized model and this response was evaluated. Δ refers to the change in the response compared to the response of a neutral foot at the start of the simulation. Only talus yaw rotation could be compared to the responses reported by Wei et al. (2012) since talus pitch, fibula yaw and fibula Δz were not reported by Wei et al. (2012).

4.3. Results

20° of calcaneus dorsiflexion loaded the lateral and syndesmotic ligaments (mean force was 427 N) more than the deltoid ligaments (mean force was 162 N), whereas 20° of calcaneus eversion loaded the deltoid ligaments (mean force was 188 N) more than the lateral and syndesmotic ligaments (mean force was 0 N) (Figure 36). In all cases, peak force was greatest in the ATiF among all the ankle ligaments.

Peak ATiF force was greatest in the DF20+ER30 case (Figure 35). Compared to the ER30 case, the DF20+ER30 case generated more ATiF force, the EV20+ER30 case generated less ATiF force, and superposition of dorsiflexion and eversion in the DF20+EV20+ER30 case generated ATiF force in between that generated in the DF20+ER30 and EV20+ER30 cases. The cases with dorsiflexion generated greater talus pitch in the positive direction than the cases without dorsiflexion (Figure 37 and Figure 38). The magnitude of fibula Δz was greatest for the DF20+ER30 case (Figure 37).

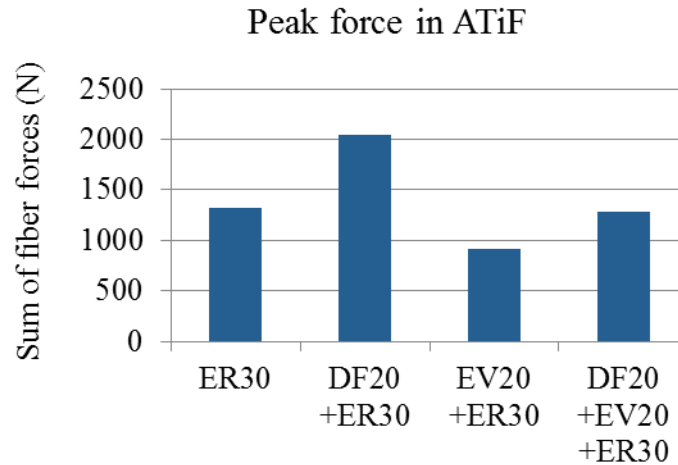


Figure 35. Peak forces in the ATiF for all cases considered.

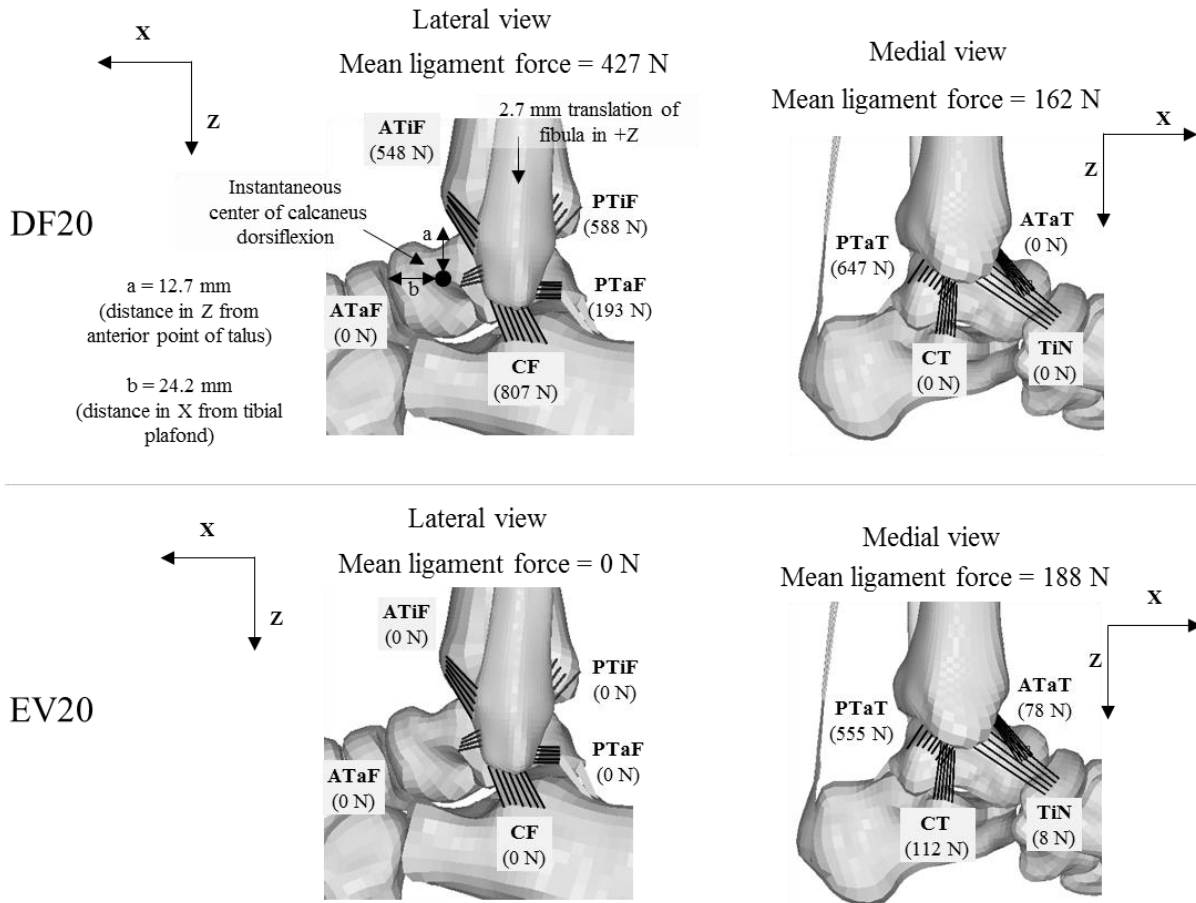


Figure 36. Schematic showing the forces in the ankle ligaments at 20° calcaneus dorsiflexion (DF20; top row) and 20° calcaneus eversion (EV20; bottom row). The black dot (top left image) marks the instantaneous center of calcaneus dorsiflexion.

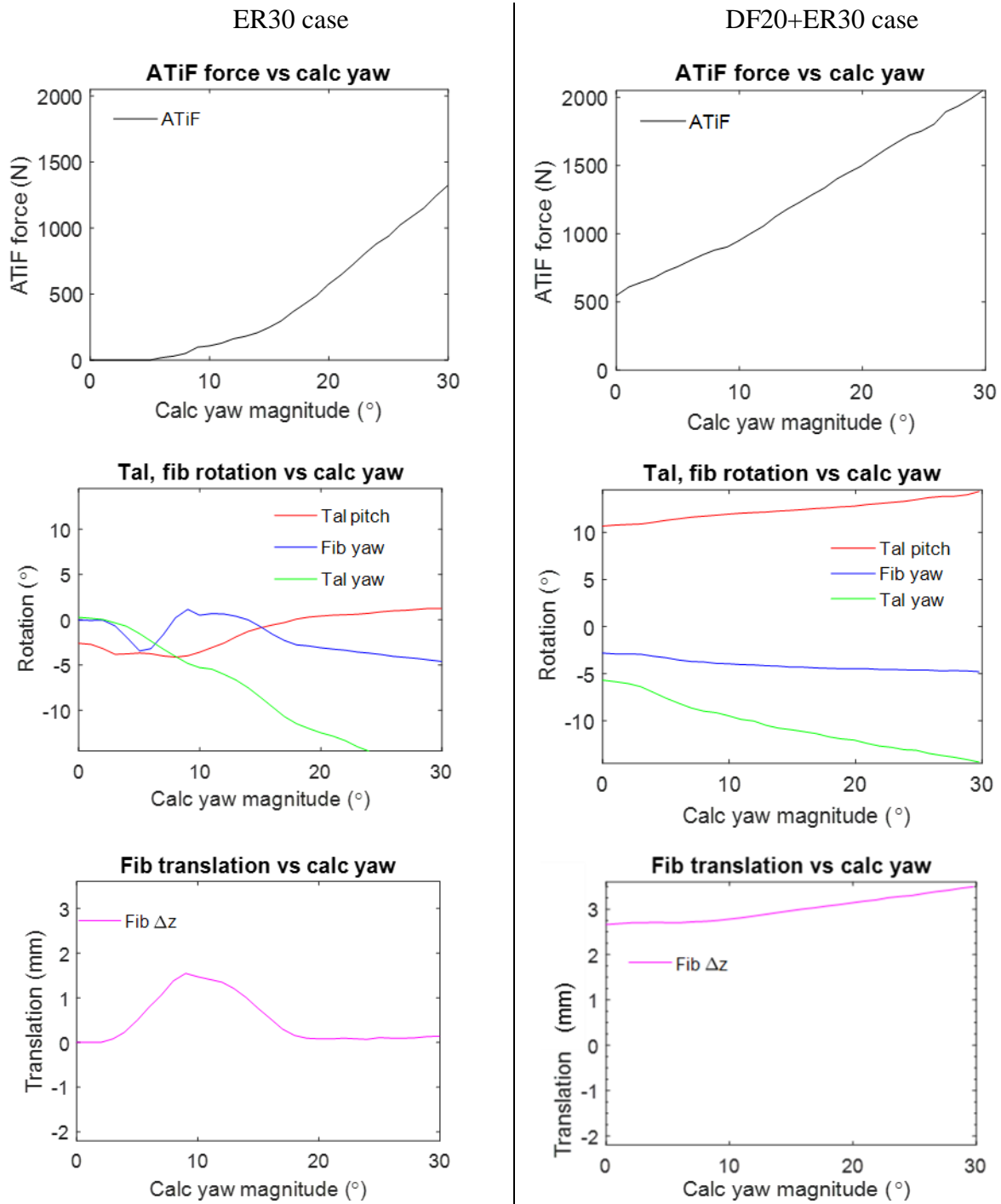


Figure 37. Total force in the ATiF, and bone kinematics for the ER30 (left column) and DF20+ER30 (right column) cases.

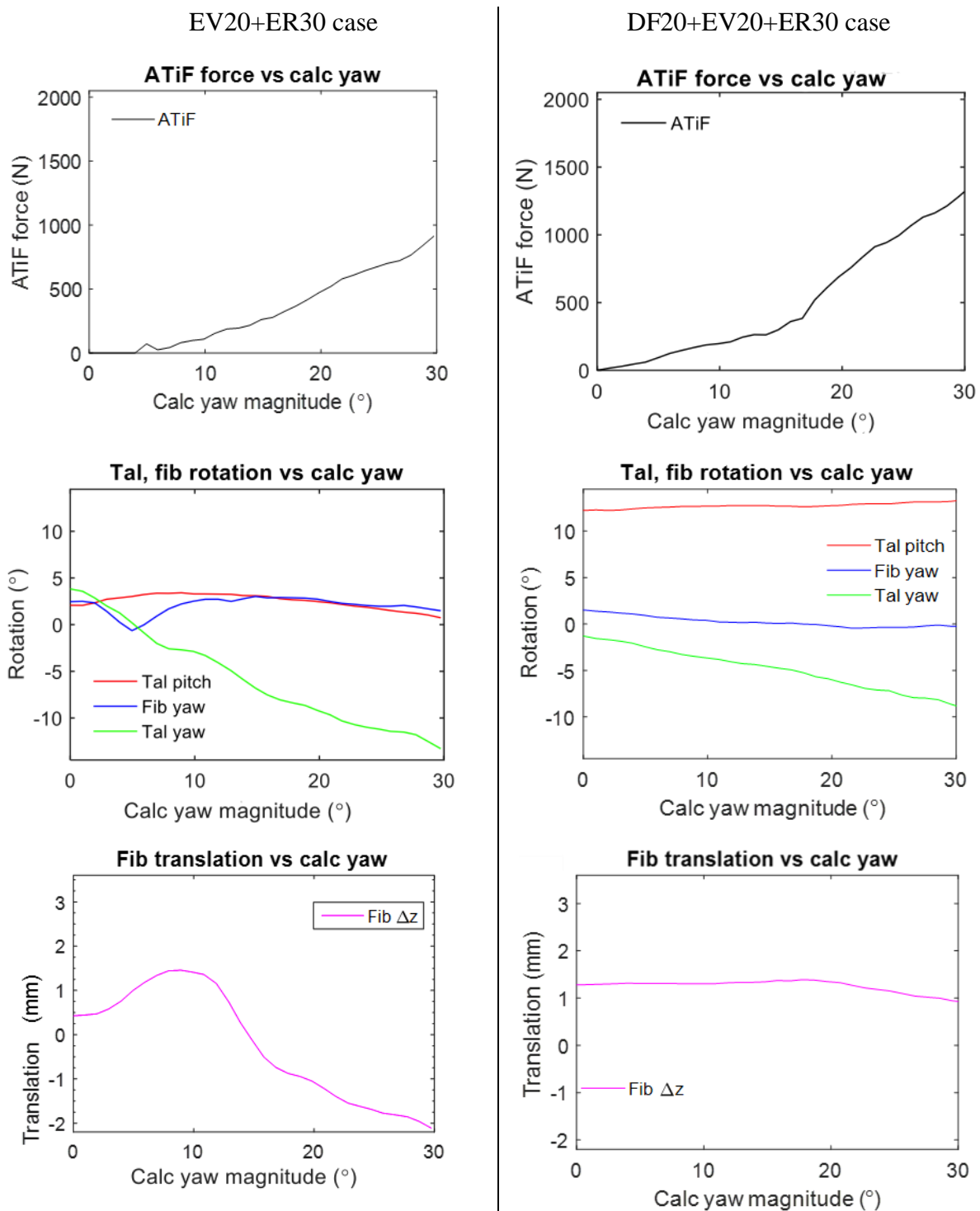


Figure 38. Total force in the ATiF, and bone kinematics for the EV20+ER30 (left column) and the DF20+EV20+ER30 (right column) cases.

4.4. Discussion

Talar wedging and fibular translation at 0° of calcaneus yaw rotation

The ATiF was first engaged at different angles of calcaneus rotation in the DF20+ER30 and EV20+ER30 cases (Figure 37 and Figure 38). This can be explained by the rotations of the talus and fibula. In the DF20+ER30 case, the ATiF fibers had a total load of 547 N at 0° of calcaneus yaw rotation (corresponding to 20° of calcaneus dorsiflexion) (Figure 37). At this point, talus pitch was 11° and talus yaw was -6°. This means that the wider anterior portion of the talar dome was more wedged into the ankle mortise (Figure 39) which increased diastasis of the tibio-fibular syndesmosis. This was observed as a fibula yaw of -3° which loaded the ATiF fibers. In comparison, in the EV20+ER30 case, the ATiF fibers had no load at 0° of calcaneus yaw rotation (corresponding to 20° of calcaneus eversion) (Figure 38). The talus had a lower pitch magnitude (2°) and a yaw rotation in the opposite direction (4°) compared with those in DF20+ER30 case. Therefore, the talus was wedged in the ankle mortise to a lesser extent which resulted in a fibula yaw rotation in the opposite direction (3°) compared to the DF20+ER30 case (Figure 37). Thus, talus pitch and yaw and fibula yaw contributed to the ATiF being engaged earlier in the DF20+ER30 case compared to the EV20+ER30 case.

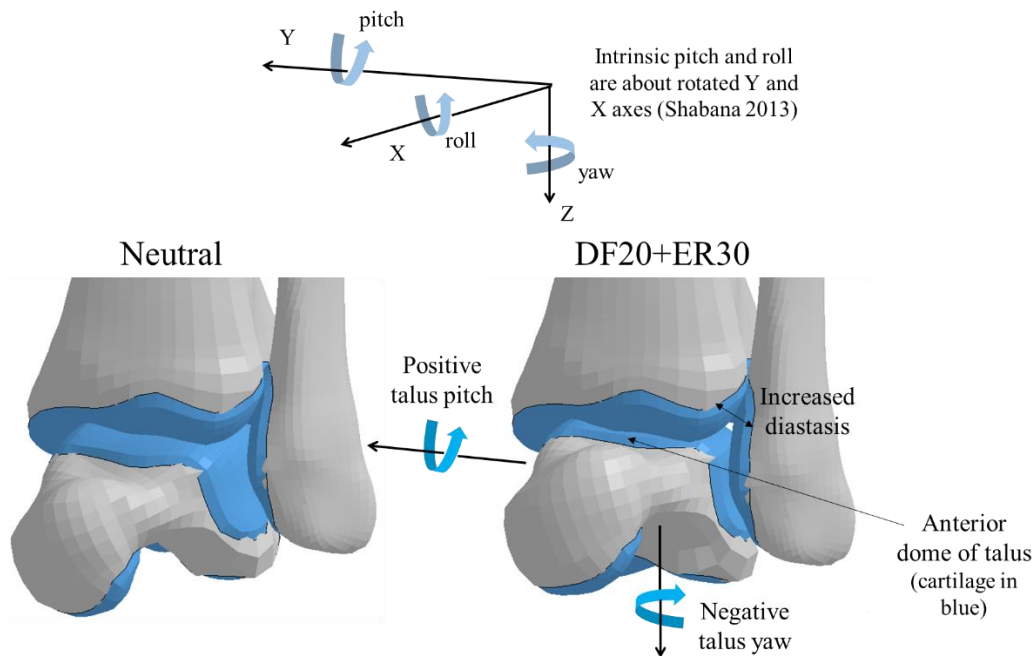


Figure 39. Schematic of talus motions that cause the talus to wedge into the ankle mortise.

Translation of the fibula and loading of the CF also contributed to the early engagement of the ATiF in the DF20+ER30 case. At 0° of calcaneus yaw rotation (Figure 37), the fibula had

translated 2.7 mm in the +Z direction. This is because the instantaneous center of calcaneus dorsiflexion was anterior to the fibula (Figure 36). Therefore, the CF fibers were loaded during dorsiflexion and pulled the fibula approximately along the +Z direction with a total force of 807 N (Figure 36). This force was primarily distributed between the ATiF and PTiF. At 0° of calcaneus yaw rotation in the EV20+ER30 case, the fibula had translated 0.4 mm in the -Z direction because the CF fibers did not bear any load. In fact, none of the lateral ligaments were loaded at 0° of calcaneus yaw rotation in the EV20+ER30 case so there was minimal force pulling the fibula in the +Z direction to load the ATiF. This suggests that that fibula inferior translation (approximately along +Z) during dorsiflexion of the calcaneus may be a mechanism for generating ATiF force. Fibula inferior translation relative to the tibia has been observed in living humans for sub-failure rotation inputs to the calcaneus (Beumer et al., 2009) and in cadaver experiments for dorsiflexion inputs to the calcaneus (Mait et al. 2016).

In the ER30 case, the ATiF was engaged at a similar value of calcaneus yaw (between 4° and 6°) to that in the EV20+ER30 case. A possible explanation for this is that the rotations of the talus at 0° of calcaneus yaw in the ER30 case were similar to those in the EV20+ER30 case. At 0° of calcaneus yaw, the talus yaw was either zero (ER30 case; Figure 37) or positive (EV20+ER30 case; Figure 38), and talus pitch values are less than 3° (in the ER30 and EV20+ER30 cases). In contrast, talus yaw was -6° and talus pitch was 11° in the DF20+ER30 case. Thus, at 0° of calcaneus yaw, the talus is wedged into the ankle mortise to a greater extent in the DF20+ER30 case than in the ER30 and EV20+ER30 cases. This caused negative yaw of the fibula in the DF20+ER30 case which loaded the ATiF. Fibula translation in the +Z direction at 0° of calcaneus yaw further loaded the ATiF in the DF20+ER30 case.

Talar wedging and fibular translation at 30° of calcaneus yaw rotation

In the DF20+ER30 case, talar wedging continued during calcaneus yaw rotation as the magnitudes of talus pitch and yaw increased. The magnitude of fibula yaw also increased to 5° and fibula Δz increased to more than 3 mm, both of which increased the force in the ATiF fibers. In the EV20+ER30 case, at 30° of calcaneus yaw, the magnitude of talus yaw increased to 13°, but the talus pitch was less than 1° and fibula yaw was only 1.5° which means that talar wedging occurred to a lesser extent than in the DF20+ER30 case. Fibula Δz decreased to less than -2 mm in the EV20+ER30 case. Consequently, at 30° of calcaneus yaw, the total force in the ATiF fibers in the EV20+ER30 case was 44.5% of the force in the DF20+ER30 case. In the ER30 case, talus yaw decreased to -17° at 30° of calcaneus yaw. This could have caused the fibula yaw of -4.5° observed at 30° of calcaneus yaw, which generated ATiF force, although to a lesser extent than the DF20+ER30 case.

Comparison with experimental studies

The bone kinematic responses of the optimized model were evaluated against experimental data reported by Mait et al. (2016) (Section 3.3). The talus yaw and pitch, and fibula yaw and Δz responses in the ER30 case were optimized to experimental data in the ER30 case (Section 3.3.2) and evaluated to be within 2° and 2 mm of the experimental data in the DF20+ER30 and EV20+ER30 cases (Section 3.3.3).

In the optimized model, cases with calcaneus eversion (EV20+ER30 and DF20+EV20+ER30; Figure 38) generated lower talus yaw magnitude, and lesser talar wedging, than cases without calcaneus eversion (ER30 and DF20+ER30; Figure 37) (Table 13). The same trend was observed in measurements at 20° of calcaneus external rotation in cadaver ankle experiments at (Button, Wei, & Haut, 2015; Mait et al., 2016a). Button et al. (2015) reported that the EV20+ER20 case produced less talus yaw than the ER20 case (Table 13) because foot eversion “unlocked” the subtalar joint (Figure 40) and reduced subtalar stiffness. The talus yaw responses of the optimized model were within the ranges reported by Button et al. (2015) (ER=20; Table 13). The trend in the optimized model also agreed with the measurements of Mait et al. (2016a) because the data reported by Mait et al. (2016a) were the optimization targets for the optimized model.

The ATiF force and talus yaw responses in the optimized model were compared with the responses reported by Wei et al. (2012) (ER=30; Table 13). The DF20+ER30 case generated more ATiF force than the DF20+EV20+ER30 case in the optimized model, whereas Wei et al. (2012) suggested the opposite trend since the ATiF was injured in the DF20+EV20+ER30 case but not in the DF20+ER30 case. This may be because of the proximal fibula constraint in the Wei et al. (2012) study which did not allow fibula Δz translation. It is possible that this constraint excluded the dorsiflexion-induced fibula inferior translation mechanism of generating ATiF force. Therefore, by potting the fibula, Wei et al. (2012) may have protected the ATiF in the DF20+ER30 case.

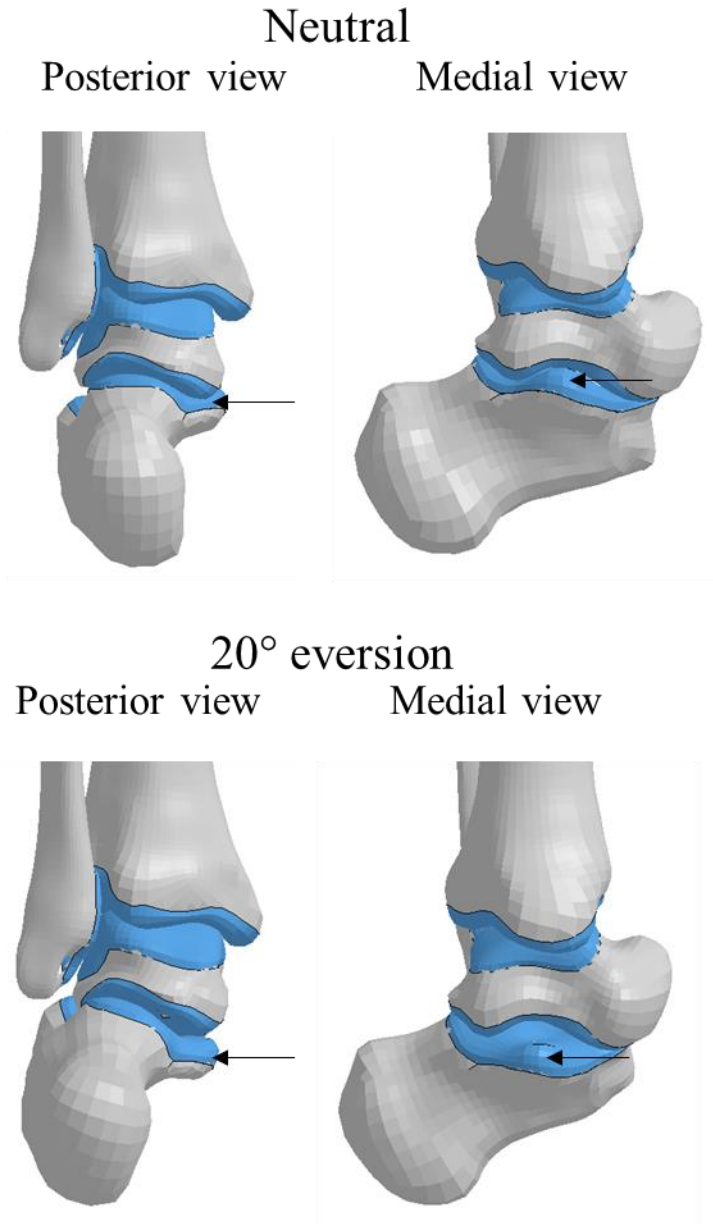


Figure 40. Schematic showing subtalar joint unlocking mechanism under calcaneus eversion (Button et al. 2015). The sustentaculum tali (shown by arrow) of the calcaneus locks with the articulating surface of the talus in the neutral position (top images). When everted, these surfaces unlock (bottom images).

Table 13. Comparison of ATiF force and talus yaw in optimized model and experiments reported by Wei et al. (2012).

Response		Loading condition			
		ER	DF20+ER	EV20+ER	DF20 + EV20 + ER
		ER = 30			
Optimized model	ATiF force (N)	1321	2049	912	1282
	Mechanism	Fibula Δz			
	Talus yaw ($^{\circ}$)	-17.0	-14.5	-13.0	-8.0
Wei et al. (2012)	ATiF	N/R	Not injured	N/R	Injured at ER = $46.8 \pm 6.1^{\circ}$
	Mechanism	Talus yaw			
	Talus yaw ($^{\circ}$)	N/R	-18.3 ± 1.8	N/R	-26.8 ± 1.4
		ER = 20			
Optimized model	Talus yaw ($^{\circ}$)	-12.5	-12.0	-8.5	-6.5
Button et al. (2015)	Talus yaw ($^{\circ}$)	-13.3 ± 2.1	N/R	-10.5 ± 2.8	N/R

N/R: this condition was not reported.

The optimized model suggested that calcaneus dorsiflexion may predispose the ATiF to injury, but Wei et al. (2012) reported that “eversion ... predisposes the ATiF to injury, forming a basis for high ankle sprains.” In the Wei et al. (2012) study, the DF20+EV20+ER30 case produced 8.5° more mean talus yaw magnitude than the DF20+ER30 case (Table 13). As described earlier in this section, the optimized model showed the opposite trend: cases with calcaneus eversion (EV20+ER30 and DF20+EV20+ER30) generated less talus yaw magnitude and ATiF force than cases without calcaneus eversion (ER30 and DF20+ER30).

A possible explanation for the increase in talus yaw magnitude due to eversion in the DF20+EV20+ER30 case in the Wei et al. (2012) study is that the ‘heel-lock’ athletic taping pattern employed by Wei et al. (2012) may have stiffened the subtalar joint (Figure 41). As mentioned

earlier in this section, Button et al. (2015) reported that calcaneus eversion reduced subtalar stiffness by unlocking the subtalar joint. Clinical studies have proposed that a heel-lock taping pattern can stiffen the subtalar joint by keeping it locked during eversion and external rotation of the calcaneus (Purcell, Schuckman, Docherty, Schrader, & Poppy, 2009; Wilkerson, 1991). The axial load applied in the Wei et al. (2012) study may also have stiffened the subtalar joint under eversion (Stiehl & Skrade, 1993). The calcaneus is connected to the talus through the subtalar joint, so a stiffer subtalar joint can produce greater talus yaw magnitude and talar wedging for an external rotation input to the calcaneus.

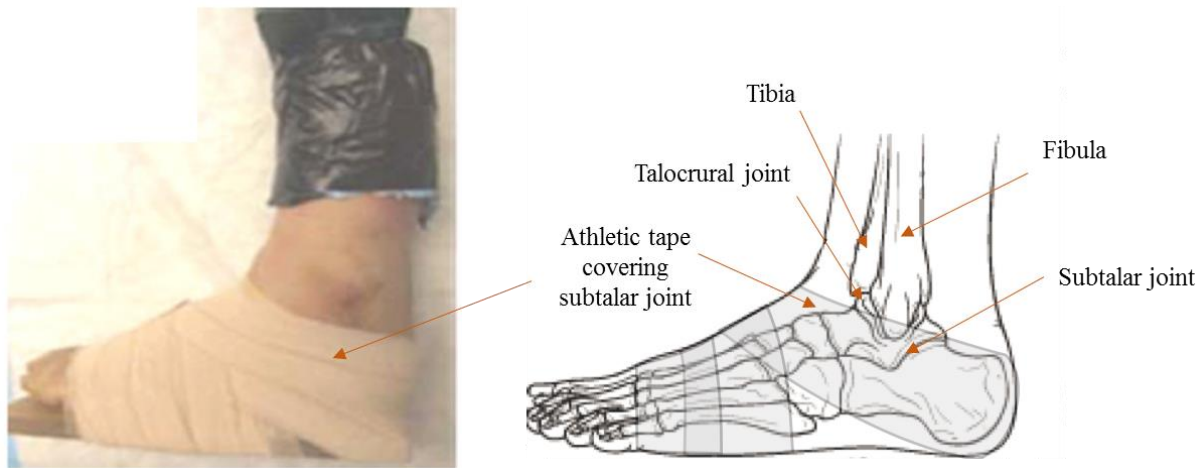


Figure 41. Lateral view of a left foot showing cadaver athletic taping pattern used by Wei et al. (2012) (left image). Schematic to show that the taping pattern may have increased the stiffness of the subtalar joint (right image).

Some differences between the optimized model and the experiments of Wei et al. (2012) and Button et al. (2015) should be noted. Wei et al. (2012) and Button et al. (2015) applied a 1500 N compressive axial load to the tibia and fibula for all cadaver experiments whereas a compressive axial load of 136.1 N was applied to the optimized model to keep the model within its intended range of applicability. Wei et al. (2012) and Button et al. (2015) also used an athletic taping pattern to constrain the foot to a base plate. Despite these differences, the talus yaw magnitudes produced by the optimized model were within the range reported by Button et al. (2015) in the ER20 and EV20+ER20 cases and within 2° of the range reported by Wei et al. (2012) in the DF20+ER30 case. This suggests that talus yaw and ATiF force may not be sensitive to axial load and subtalar stiffening due to taping in the ER30, EV20+ER30, and DF20+ER30 cases. The talus yaw magnitude in the optimized model deviated significantly from the response in the Wei et al. (2012) study in the DF20+EV20+ER30 case, which suggests that talus yaw and ATiF force may be sensitive to subtalar stiffening due to axial load or taping in the DF20+EV20+ER30 case. A higher

axial load and use of a taping pattern may keep the subtalar joint locked during eversion and produce a talus yaw magnitude in the optimized model that is closer to that reported by Wei et al. (2012) in the DF20+EV20+ER30 case. The sensitivity of talus yaw and ATiF force to subtalar stiffening due to axial load and athletic taping can be avenues for future research.

The effect of the taping pattern on talus yaw magnitude and ATiF force was not considered in the optimized model because the mechanical characteristics of the taping pattern (such as stiffness and friction) were not reported by Wei et al. (2012). Moreover, the complex geometry and contact characteristics of the athletic taping pattern present modeling challenges in an FE environment. As a tractable alternative, subtalar stiffening due to taping may be simulated by directly stiffening the talo-calcaneal ligaments that comprise the subtalar joint. These ligaments were beyond the scope of this thesis. The effect of stiffening the subtalar joint on ATiF force in the optimized model in the DF20+EV20+ER30 case can be studied in the future to gain further insight into the *in situ* behavior of the ATiF.

Fibula Δz translation occurs during sub-failure rotations of the ankle (Beumer et al., 2009). However, the precise relationship between calcaneus dorsiflexion and fibula Δz translation under compressive axial loads on the order of human body weight applied to the proximal tibia and fibula is not known. This may affect the magnitude of ATiF force generated due to dorsiflexion and can be investigated in the future.

The ranges of rotation inputs to the calcaneus for the optimized model were in sub-injury regimes, therefore we expect the ligament force responses to be less than the failure forces of the ligaments. A large range of failure force values (625 to 2510 N) of ankle syndesmosis ligaments (including the ATiF) is reported in the literature (Beumer, van Hemert, Swierstra, Jasper, & Belkoff, 2003; Hoefnagels, Waites, Wing, Belkoff, & Swierstra, 2007), with the failure force for ligaments from younger specimens (aged 16 to 26 years) being 2.36 times greater than the failure force for ligaments from older specimens (aged 48-86 years) (Noyes & Grood, 1976). This suggests that the peak ATiF forces in the optimized model may be within a sub-failure range or, in some cases, approaching failure.

4.5. Conclusion

The objective of this chapter was to describe the relationship between total force in the ATiF and talus pitch and yaw, and fibula yaw and Δz for rotation inputs to the calcaneus that were relevant to syndesmotoc ankle sprains. The DF20+ER30 case generated maximum ATiF force among the four cases considered. 20° of dorsiflexion caused more talar wedging in the syndesmotoc joint and inferior translation of the fibula than 20° of eversion, which led to greater ATiF force due to dorsiflexion. Therefore, the optimized model suggested that dorsiflexion may predispose the ATiF to injury under external rotation more than eversion. Wei et al. (2012) reported the opposite trend.

One possible explanation for this difference is that the rigid potting of the proximal fibula in the study by Wei et al. (2012) prevented inferior translation of the fibula during dorsiflexion, which may have protected the ATiF. Another possible explanation is that talus yaw and ATiF force may be sensitive to subtalar stiffening due to axial load and the athletic taping pattern employed by Wei et al. (2012) in the DF20+EV20+ER30 case. This may have caused more talar wedging and predisposed the ATiF to injury. It is recommended that the effect of subtalar stiffening on ATiF force be investigated in the future. In this way, the optimized model was able to provide insight into the relationship between ATiF force and kinematic responses of the talus and fibula for rotation inputs to the calcaneus that were relevant to syndesmotic ankle sprains.

Chapter 5

Conclusions, limitations and future work

5.1. Conclusions

Computational ankle models reported in the literature fall into two broad categories. The first includes models validated at the gross structural level and the second includes detailed models of ligaments that do not consider gross joint mechanics. This thesis is a step toward establishing a link between these two categories for understanding the relationship between gross ankle mechanics and the underlying *in situ* ligament mechanics.

The UVA Ankle model was refined for this thesis. The bone geometry of the UVA Ankle model was retained and the insertion geometries of the ankle ligaments were updated based on anatomical studies and cadaver dissections. The ligaments were modeled as distributions of springs to distribute the loads transmitted by the ligaments across the insertion sites. Articular cartilage was represented in the UVA ankle model to achieve a realistic anatomical representation. Cartilage also served to reduce the gaps between the bones in the ankle, which reduced hard bone to bone contact and led to physically more realistic bone kinematic responses under an external rotation input to the calcaneus.

The ligaments in the refined model were parameterized to represent *in situ* fiber toe regions, the number of fibers in a ligament, and the skewness of the IOM. A simplifying assumption of a bilinear *in situ* fiber stiffness curve was made. A sensitivity study based on a multivariate linear regression model showed that the bone kinematic responses were most sensitive to the *in situ* fiber toe regions. Therefore, the *in situ* fiber toe regions were optimized to match the bone kinematic responses of the model to the responses of a cadaver ankle (specimen 743L). The bone kinematic responses of the optimized model were evaluated against the responses of specimen 743L under sequential rotation inputs to the calcaneus. Some deviations were observed in the navicular kinematic responses and the moment response under dorsiflexion followed by external rotation, but the model responses generally agreed with experimental data.

The optimized model was an improvement over existing computational ankle models because it was able to meet experimental evaluation targets by optimizing only nine parameters. These parameters represent the *in situ* fiber toe regions of ankle ligaments under certain simplifying assumptions. This provides some insight into the *in situ* behaviors of ankle ligaments, which are extremely difficult to measure experimentally. Prior to this study, few quantitative descriptions of the *in situ* toe regions of ankle ligaments at the fiber level were available. Based on the results of this thesis, it is recommended that *in situ* toe regions be represented in computational ankle models to study bone kinematics and ligament mechanics.

The relationship between total force in the ATiF and talus pitch and yaw, and fibula yaw and Δz for combinations of dorsiflexion, eversion and external rotation inputs to the calcaneus was described. 20° of dorsiflexion caused more talar wedging in the syndesmotic joint and inferior translation of the fibula than 20° of eversion, which led to greater ATiF force. Therefore, the optimized model suggested that dorsiflexion may predispose the ATiF to injury under external rotation more than eversion. In comparison, Wei et al. (2012) reported that eversion predisposed the ATiF to injury. This may be because talus yaw differed significantly in the Wei et al. (2012) study compared to the optimized model in the DF20+EV20+ER30 case. Talus yaw and ATiF force may be sensitive to subtalar stiffening due to axial load and the athletic taping pattern employed by Wei et al. (2012) in the DF20+EV20+ER30 case. The potential sensitivity to subtalar stiffening due to axial load and athletic taping can be investigated further to understand mechanisms that may predispose the ATiF to injury. This can further elucidate the relationship between *in situ* ligament mechanics, bone kinematics and gross ankle kinematics relevant to syndesmotic ankle sprains

5.2. Limitations

Biological variability in bone and ligament insertion geometry was beyond the objectives of this thesis, so the degree to which the results are generalizable to the population remains unknown. Variability of bone geometry and insertion sites may influence the ligament responses obtained using the methods employed in this thesis. Further research efforts are necessary to quantify these effects for the optimized model.

The overall mechanical behavior of ankle ligaments was idealized using a bilinear stiffness curve at the fiber level. Viscoelastic and nonlinear behaviors of the ankle ligaments have been experimentally observed and formulated in models such as the quasilinear viscoelastic (QLV) model commonly applied in biomechanics (Fung 1972, Funk et al. 2000, Forestiero, Carniel and Natali 2014). More advanced models could be used to explore additional aspects of ligament nonlinear behavior under various loading conditions.

The effect of musculotendinous structures was ignored. A large part of the effect of muscle contraction can be modeled through a compressive axial load applied to the calcaneus since the Achilles tendon is the most significant load path. Tensile load in the Achilles tendon leads to axial compression of the leg. However, muscle contraction influences gross ankle mechanics, bone kinematics and ligament mechanics in other ways as well (Baumhauer et al. 1995). Reasonable muscle force and activation timing need to be implemented to refine the model response.

5.3. Future work

The optimized model has been evaluated against experimental data at the level of bone kinematics and gross external rotation moment. It also represents ligament fibers that have a physical interpretation. This is an improvement over computational ankle models reported in the literature. It can be used to obtain insight into the *in situ* behavior of ankle ligaments that is not accessible to experiments. Ligament deformations and loads under different loading conditions can be studied to understand the relationship between gross ankle mechanics and the underlying *in situ* ligament mechanics.

The immediate extension of this thesis will be to include failure criteria at the fiber level in the optimized model to understand ligament injury mechanisms. The resulting model with ligament failure can be used to study the injury mechanism of syndesmotic ankle sprains, which was the motivation for this thesis. Since the optimized model has been evaluated against the responses of one specimen, it can be used as a computational surrogate. A computational surrogate can be loaded multiple times to cause injury, whereas an injured post-mortem human surrogate cannot be tested again. Computational surrogates also have the advantage of high controllability and repeatability, and the cost of a simulation is far less than the cost of an experiment. The proposed model with ligament failure can be a valuable tool to study ligament injury mechanisms.

Much remains to be known about the mechanism of, and prevention strategies for syndesmotic ankle sprains. There is a paucity of literature on syndesmotic ankle sprains compared to lateral ankle sprains (Williams, Jones, & Amendola, 2007). Moreover, the literature that does exist is focused more on diagnosis and treatment of these injuries (Lin, Gross, & Weinhold, 2006; Nussbaum et al., 2001; Williams et al., 2007). While a few studies have investigated the injury mechanism (Button, Wei, Meyer, & Haut, 2013; Wei et al., 2012), these studies did not attempt to investigate injury prevention. The proposed model can be used to systematically study the mechanism of, and prevention strategies for syndesmotic ankle sprains.

The proposed model can also be used to study injury prevention techniques for lateral ankle sprains. Injury prevention strategies for ankle sprains include bracing, taping, sparring (Kaminski et al., 2013; Mickel et al., 2006), shoe design (Barrett et al., 1993), and proprioceptive training (Verhagen et al., 2004). Anderson, Hunt, and McCormick (2010) reported that although these strategies can be effective in preventing foot and ankle sprains, they are applied in an ad-hoc manner and studies on “definitive injury prevention” are lacking. The proposed model can add scientific rigor to the craft of prevention of ankle ligament injuries.

References

- Anderson, R. B., Hunt, K. J., & McCormick, J. J. (2010). Management of Common Sports-related Injuries About the Foot and Ankle. *Journal of the American Academy of Orthopaedic Surgeons*, *18*(9), 546-556.
- Barrett, J. R., Tanji, J. L., Drake, C., Fuller, D., Kawasaki, R. I., & Fenton, R. M. (1993). High-versus low-top shoes for the prevention of ankle sprains in basketball players A prospective randomized study. *The American Journal of Sports Medicine*, *21*(4), 582-585.
- Beumer, A., Valstar, E. R., Garling, E. H., Niesing, R., Ranstam, J., Löfvenberg, R., & Swierstra, B. A. (2003). Kinematics of the distal tibiofibular syndesmosis: radiostereometry in 11 normal ankles. *Acta orthopaedica Scandinavica*, *74*(3), 337-343.
- Beumer, A., van Hemert, W. L., Swierstra, B. A., Jasper, L. E., & Belkoff, S. M. (2003). A biomechanical evaluation of the tibiofibular and tibiotalar ligaments of the ankle. *Foot & ankle international*, *24*(5), 426-429.
- Blankevoort, L., & Huiskes, R. (1996). Validation of a three-dimensional model of the knee. *Journal of Biomechanics*, *29*(7), 955-961.
- Boytim, M. J., Fischer, D. A., & Neumann, L. (1991). Syndesmotic ankle sprains. *The American journal of sports medicine*, *19*(3), 294-298.
- Button, K. D., Wei, F., & Haut, R. C. (2015). Unlocking the talus by eversion limits medial ankle injury risk during external rotation. *Journal of biomechanics*, *48*(13), 3724-3727.
- Button, K. D., Wei, F., Meyer, E. G., & Haut, R. C. (2013). Specimen-Specific Computational Models of Ankle Sprains Produced in a Laboratory Setting. *Journal of biomechanical engineering*, *135*(4), 041001.
- Carson, M. C., Harrington, M. E., Thompson, N., O'connor, J. J., & Theologis, T. N. (2001). Kinematic analysis of a multi-segment foot model for research and clinical applications: a repeatability analysis. *Journal of biomechanics*, *34*(10), 1299-1307.
- Chen, J., Siegler, S., & Schneck, C. D. (1988). The three-dimensional kinematics and flexibility characteristics of the human ankle and subtalar joint—part II: flexibility characteristics. *Journal of biomechanical engineering*, *110*(4), 374-385.
- Collins, L. M., Dziak, J. J., & Li, R. (2009). Design of experiments with multiple independent variables: a resource management perspective on complete and reduced factorial designs. *Psychological methods*, *14*(3), 202.
- Colville, M. R., Marder, R. A., Boyle, J. J., & Zarins, B. (1990). Strain measurement in lateral ankle ligaments. *The American journal of sports medicine*, *18*(2), 196-200.

- Ekstrand, J., & Tropp, H. (1990). The incidence of ankle sprains in soccer. *Foot & Ankle International*, 11(1), 41-44.
- Forestiero, A., Carniel, E. L., & Natali, A. N. (2014). Biomechanical behaviour of ankle ligaments: constitutive formulation and numerical modelling. *Computer methods in biomechanics and biomedical engineering*, 17(4), 395-404.
- Fung, Y. C. (2013). *Biomechanics: mechanical properties of living tissues*. Springer Science & Business Media.
- Funk, J. R., Hall, G. W., Crandall, J. R., & Pilkey, W. D. (2000). Linear and quasi-linear viscoelastic characterization of ankle ligaments. *Journal of biomechanical engineering*, 122(1), 15-22.
- Gabler, L. F., Panzer, M. B., & Salzar, R. S. (2014). High-Rate Mechanical Properties of Human Heel Pad for Simulation of a Blast Loading Condition. IRC-14-87 IRCOBI Conference 2014.
- Garrick, J. G. (1977). The frequency of injury, mechanism of injury, and epidemiology of ankle sprains*. *The American journal of sports medicine*, 5(6), 241-242.
- Haraguchi, N., & Armiger, R. S. (2009). A new interpretation of the mechanism of ankle fracture. *The Journal of Bone & Joint Surgery*, 91(4), 821-829.
- Hoefnagels, E. M., Waites, M. D., Wing, I. D., Belkoff, S. M., & Swierstra, B. A. (2007). Biomechanical comparison of the interosseous tibiofibular ligament and the anterior tibiofibular ligament. *Foot & ankle international*, 28(5), 602-604.
- Jenkyn, T. R., & Nicol, A. C. (2007). A multi-segment kinematic model of the foot with a novel definition of forefoot motion for use in clinical gait analysis during walking. *Journal of biomechanics*, 40(14), 3271-3278.
- Johnson, E. E., & Markolf, K. L. (1983). The contribution of the anterior talofibular ligament to ankle laxity. *J Bone Joint Surg Am*, 65(1), 81-88.
- Kaminski, T. W., Hertel, J., Amendola, N., Docherty, C. L., Dolan, M. G., Hopkins, J. T., ... & Richie, D. (2013). National Athletic Trainers' Association position statement: conservative management and prevention of ankle sprains in athletes. *Journal of athletic training*, 48(4), 528-545.
- Kärrholm, J., Hansson, L. I., & Selvik, G. (1985). Mobility of the lateral malleolus: A roentgen stereophotogrammetric analysis. *Acta Orthopaedica Scandinavica*, 56(6), 479-483.
- Kastelic, J., Palley, I., & Baer, E. (1980). A structural mechanical model for tendon crimping. *Journal of biomechanics*, 13(10), 887-893.

- Kwak, S. D., Blankevoort, L., & Ateshian, G. A. (2000). A mathematical formulation for 3D quasi-static multibody models of diarthrodial joints. *Computer methods in biomechanics and biomedical engineering*, 3(1), 41-64.
- Li, G., Gil, J., Kanamori, A., & Woo, S. Y. (1999). A validated three-dimensional computational model of a human knee joint. *Journal of biomechanical engineering*, 121(6), 657-662.
- Liacouras, P. C., & Wayne, J. S. (2007). Computational modeling to predict mechanical function of joints: application to the lower leg with simulation of two cadaver studies. *Journal of biomechanical engineering*, 129(6), 811-817.
- Lin, C. F., Gross, M. T., & Weinhold, P. (2006). Ankle syndesmosis injuries: anatomy, biomechanics, mechanism of injury, and clinical guidelines for diagnosis and intervention. *Journal of Orthopaedic & Sports Physical Therapy*, 36(6), 372-384.
- Lucas, S. R., Bass, C. R., Crandall, J. R., Kent, R. W., Shen, F. H., & Salzar, R. S. (2009). Viscoelastic and failure properties of spine ligament collagen fascicles. *Biomechanics and modeling in mechanobiology*, 8(6), 487-498.
- Lundberg, A., Svensson, O. K., Nemeth, G., & Selvik, G. (1989). The axis of rotation of the ankle joint. *Journal of Bone & Joint Surgery, British Volume*, 71(1), 94-99.
- Mait, A. R., Forman, J. L., Mane, A., Donlon, J. P., & Kent, R. W. (2016a). Quasi-Static Kinematics Capture of Human Leg Bones during Internal and External Foot Rotation (manuscript in preparation). *Journal of Biomechanics* (target journal).
- Mait, A. R., Forman, J. L., Mane, A., Donlon, J. P., & Kent, R. W. (2016b). Transient Kinetics of the Human Ankle during Internal and External Foot Rotation with Consideration of Functional Boundary Conditions (manuscript in preparation). *Journal of Biomechanics* (target journal).
- Mait, A. R., Mane, A., Donlon, J. P., Forman, J. L., & Kent, R. W. (2015). Kinetics and kinematics of the ankle during foot external rotation. In *Proceedings of the 39th Annual Meeting of the American Society of Biomechanics*. Columbus, USA.
- McKay, M. D., Beckman, R. J., & Conover, W. J. (2000). A comparison of three methods for selecting values of input variables in the analysis of output from a computer code. *Technometrics*, 42(1), 55-61.
- Mickel, T. J., Bottoni, C. R., Tsuji, G., Chang, K., Baum, L., & Tokushige, K. A. S. (2006). Prophylactic bracing versus taping for the prevention of ankle sprains in high school athletes: a prospective, randomized trial. *The journal of foot and ankle surgery*, 45(6), 360-365.
- Millington, S. A., Grabner, M., Wozelka, R., Anderson, D. D., Hurwitz, S. R., & Crandall, J. R. (2007). Quantification of ankle articular cartilage topography and thickness using a high resolution stereophotography system. *Osteoarthritis and cartilage*, 15(2), 205-211.

- Mow, V. C., Holmes, M. H., & Lai, W. M. (1984). Fluid transport and mechanical properties of articular cartilage: a review. *Journal of biomechanics*, 17(5), 377-394.
- Mow, V. C., & Mansour, J. M. (1977). The nonlinear interaction between cartilage deformation and interstitial fluid flow. *Journal of Biomechanics*, 10(1), 31-39.
- Myers, R. H., Montgomery, D. C., & Anderson-Cook, C. M. (2016). *Response surface methodology: process and product optimization using designed experiments*. John Wiley & Sons.
- Neal, M. O. (2004, January). Front structure design procedure for optimal pedestrian leg impact performance. In *ASME 2004 International Design Engineering Technical Conferences and Computers and Information in Engineering Conference* (pp. 199-205). American Society of Mechanical Engineers.
- Neal, M. O., Tu, J., & Jones, D. R. (2008). *A response surface based tool for evaluating vehicle performance in the pedestrian leg impact test* (No. 2008-01-1244). SAE Technical Paper.
- Nie, B., Panzer, M. B., Mane, A., Mait, A. R., Donlon, J. P., Forman, J. L., & Kent, R. W. (2015). A framework for parametric modeling of ankle ligaments to determine the in situ response under gross foot motion. *Computer methods in biomechanics and biomedical engineering*, 1-12.
- Nie, B., Panzer, M. B., Mane, A., Mait, A. R., Donlon, J. P., Forman, J. L., & Kent, R. W. (2016). In situ behavior of ankle ligaments (under review). *Journal of the Mechanical Behavior of Biomedical Materials*.
- Nigg, B. M., Skarvan, G., Frank, C. B., & Yeadon, M. R. (1990). Elongation and forces of ankle ligaments in a physiological range of motion. *Foot & Ankle International*, 11(1), 30-40.
- Noyes, F. R., & Grood, E. S. (1976). The strength of the anterior cruciate ligament in humans and Rhesus monkeys. *J Bone Joint Surg Am*, 58(8), 1074-1082.
- Nussbaum, E. D., Hosea, T. M., Sieler, S. D., Incremona, B. R., & Kessler, D. E. (2001). Prospective evaluation of syndesmotic ankle sprains without diastasis. *The American journal of sports medicine*, 29(1), 31-35.
- Purcell, S. B., Schuckman, B. E., Docherty, C. L., Schrader, J., & Poppy, W. (2009). Differences in ankle range of motion before and after exercise in 2 tape conditions. *The American journal of sports medicine*, 37(2), 383-389.
- Reinschmidt, C., Van Den Bogert, A. J., Lundberg, A., Nigg, B. M., Murphy, N., Stacoff, A., & Stano, A. (1997). Tibiofemoral and tibiocalcaneal motion during walking: external vs. skeletal markers. *Gait & Posture*, 6(2), 98-109.
- Rubin, A., & Sallis, R. (1996). Evaluation and diagnosis of ankle injuries. *American family physician*, 54(5), 1609-1618.

- Shabana, A. A. (2013). *Dynamics of multibody systems*. Cambridge university press.
- Shin, J., Yue, N., & Untaroiu, C. D. (2012). A finite element model of the foot and ankle for automotive impact applications. *Annals of biomedical engineering*, 40(12), 2519-2531.
- Siegler, S., Chen, J., & Schneck, C. D. (1988). The three-dimensional kinematics and flexibility characteristics of the human ankle and subtalar joints—Part I: Kinematics. *Journal of biomechanical engineering*, 110(4), 364-373.
- Stander, N., Roux, W., Eggleston, T., & Craig, K. (2007). LS-OPT user's manual—a design optimization and probabilistic analysis tool for the engineering analyst. *Livermore Software Technology Corporation, Livermore*.
- Stiehl, J. B., Skrade, D. A., Needleman, R. L., & Scheidt, K. B. (1993). Effect of axial load and ankle position on ankle stability. *Journal of orthopaedic trauma*, 7(1), 72-77.
- Stiehl, J. B., Skrade, D. A., & Johnson, R. P. (1992). Experimentally produced ankle fractures in autopsy specimens. *Clinical orthopaedics and related research*, 285, 244-249.
- Svensson, O. K., Lundberg, A., Walheim, G., & Selvik, G. (1989). In vivo fibular motions during various movements of the ankle. *Clinical Biomechanics*, 4(3), 155-160.
- Tranberg, R., & Karlsson, D. (1998). The relative skin movement of the foot: a 2-D roentgen photogrammetry study. *Clinical Biomechanics*, 13(1), 71-76.
- Verhagen, E., Van der Beek, A., Twisk, J., Bouter, L., Bahr, R., & Van Mechelen, W. (2004). The effect of a proprioceptive balance board training program for the prevention of ankle sprains a prospective controlled trial. *The American journal of sports medicine*, 32(6), 1385-1393.
- Villwock, M. R., Meyer, E. G., Powell, J. W., & Haut, R. C. (2009, June). External rotation ankle injuries: investigating ligamentous rupture. In *ASME 2009 Summer Bioengineering Conference* (pp. 253-254). American Society of Mechanical Engineers.
- Wei, F., Hunley, S. C., Powell, J. W., & Haut, R. C. (2011). Development and validation of a computational model to study the effect of foot constraint on ankle injury due to external rotation. *Annals of biomedical engineering*, 39(2), 756-765.
- Wei, F., Post, J. M., Braman, J. E., Meyer, E. G., Powell, J. W., & Haut, R. C. (2012). Eversion during external rotation of the human cadaver foot produces high ankle sprains. *Journal of Orthopaedic Research*, 30(9), 1423-1429.
- Wei, F., Villwock, M. R., Meyer, E. G., Powell, J. W., & Haut, R. C. (2010). A biomechanical investigation of ankle injury under excessive external foot rotation in the human cadaver. *Journal of biomechanical engineering*, 132(9), 091001.

Wilkerson, G. B. (1991). Comparative biomechanical effects of the standard method of ankle taping and a taping method designed to enhance subtalar stability. *The American journal of sports medicine*, 19(6), 588-595.

Williams, G. N., Jones, M. H., & Amendola, A. (2007). Syndesmotic ankle sprains in athletes. *The American journal of sports medicine*, 35(7), 1197-1207.

Xenos, J. S., Hopkinson, W. J., Mulligan, M. E., Olson, E. J., & Popovic, N. A. (1995). The tibiofibular syndesmosis. Evaluation of the ligamentous structures, methods of fixation, and radiographic assessment. *J Bone Joint Surg Am*, 77(6), 847-856.

Appendix 1

This appendix contains sensitivity coefficients, confidence intervals and p values for the six most sensitive DVs for each response from the multivariable regression analysis in Section 3.2.2. Statistical significance was evaluated based on the criteria described in Section 3.2.1 (Algorithm of the sensitivity study). Quantile-Quantile (QQ) plots of the residuals of each model versus standard normal samples are also provided in this appendix.

Response: yaw_fib

Variable	Sensitivity	Confidence Interval (lower)	Confidence Interval (upper)	Confidence interval	p value
ci_ATiF	-14.94	-15.35	-14.53	0.83	0.00E+00
ci_PTaF	9.62	9.20	10.03	0.83	2.22E-244
ci_CaIF	-6.41	-6.82	-6.00	0.83	2.41E-143
ci_TibN	-1.83	-2.24	-1.41	0.83	2.03E-17
ci_CaIT	-1.66	-2.08	-1.25	0.83	6.21E-15
ci_PTiF	1.26	0.84	1.67	0.83	3.65E-09

Response: pitch_fib

Variable	Sensitivity	Confidence Interval (lower)	Confidence Interval (upper)	Confidence interval	p value
ci_TibN	1.76	1.68	1.84	0.16	1.13E-224
ci_CaIF	1.04	0.96	1.12	0.16	9.67E-108
ci_ATiF	-0.85	-0.93	-0.76	0.16	8.28E-78
ci_CaIT	0.26	0.18	0.34	0.16	2.79E-10
ci_ATaT	0.22	0.14	0.30	0.16	1.60E-07
ci_PTaT	0.18	0.10	0.26	0.16	1.20E-05

Response: roll_fib

Variable	Sensitivity	Confidence Interval (lower)	Confidence Interval (upper)	Confidence interval	p value
ci_ATiF	1.49	1.45	1.52	0.06	0.00E+00
ci_CaIF	0.39	0.36	0.42	0.06	3.89E-97
ci_PTaF	-0.18	-0.21	-0.15	0.06	2.81E-26
ci_PTaT	0.07	0.03	0.10	0.06	8.10E-05
ci_CaIT	0.06	0.03	0.09	0.06	2.66E-04
ci_PTiF	-0.05	-0.08	-0.01	0.06	4.60E-03

Response: yaw_tal

Variable	Sensitivity	Confidence Interval (lower)	Confidence Interval (upper)	Confidence interval	p value
ci_PTaF	-10.50	-10.90	-10.20	0.70	8.17E-284
ci_PTaT	-3.31	-3.71	-2.91	0.80	6.34E-53
ci_ATiF	-2.20	-2.60	-1.80	0.80	5.56E-26
ci_CalF	1.26	0.86	1.66	0.80	8.51E-10
ci_ATaT	-0.54	-0.94	-0.14	0.80	8.00E-03
ci_TibN	0.45	0.05	0.85	0.80	2.87E-02

Response: pitch_tal

Variable	Sensitivity	Confidence Interval (lower)	Confidence Interval (upper)	Confidence interval	p value
ci_PTaT	4.82	4.54	5.10	0.56	1.22E-167
ci_CalF	-4.20	-4.47	-3.92	0.56	8.10E-138
ci_ATiF	-2.58	-2.86	-2.30	0.56	6.75E-64
ci_ATaT	-2.50	-2.78	-2.22	0.56	3.13E-60
ci_PTaF	2.31	2.03	2.59	0.56	7.73E-53
ci_TibN	-1.42	-1.70	-1.14	0.56	1.59E-22

Response: roll_tal

Variable	Sensitivity	Confidence Interval (lower)	Confidence Interval (upper)	Confidence interval	p value
ci_ATiF	-4.19	-4.53	-3.84	0.69	2.84E-99
ci_CalF	-3.81	-4.15	-3.46	0.69	9.28E-85
ci_ATaT	3.46	3.11	3.81	0.69	2.29E-72
ci_PTaT	1.74	1.39	2.09	0.69	6.15E-22
ci_TibN	-1.25	-1.59	-0.90	0.69	3.10E-12
ci_CalT	-0.91	-1.25	-0.56	0.69	4.04E-07

Response: yaw_nav

Variable	Sensitivity	Confidence	Confidence	Confidence interval	p value
		Interval (lower)	Interval (upper)		
ci_TibN	-4.72	-4.93	-4.51	0.42	1.92E-232
ci_ATiF	-3.16	-3.38	-2.95	0.42	1.31E-136
ci_CalF	-3.13	-3.34	-2.91	0.42	5.73E-134
ni_TibN	0.75	0.54	0.96	0.42	6.12E-12
ci_PTaF	-0.32	-0.54	-0.11	0.42	2.60E-03
ni_CalF	0.26	0.05	0.47	0.42	1.58E-02

Response: pitch_nav

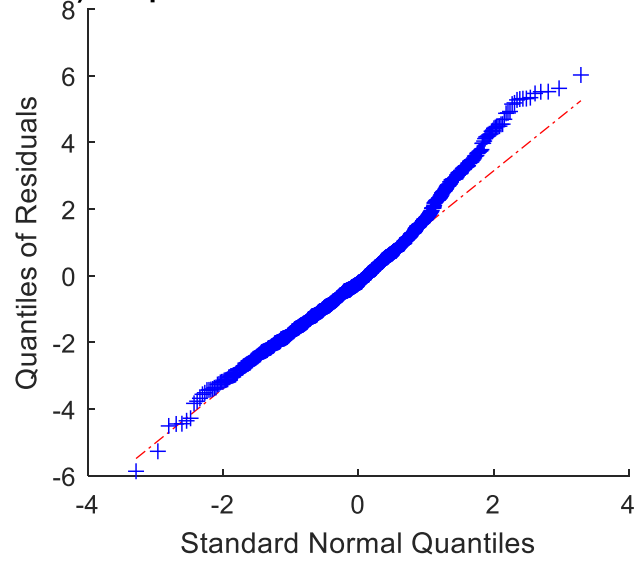
Variable	Sensitivity	Confidence	Confidence	Confidence interval	p value
		Interval (lower)	Interval (upper)		
ci_CalF	-1.46	-1.56	-1.36	0.21	5.43E-123
ci_ATiF	-1.44	-1.54	-1.33	0.21	7.02E-120
ci_PTaF	-0.90	-1.01	-0.80	0.21	1.27E-56
ci_ATaT	-0.45	-0.56	-0.35	0.21	1.37E-16
ci_TibN	-0.42	-0.53	-0.32	0.21	5.43E-15
ni_CalF	0.18	0.08	0.29	0.21	5.45E-04

Response: roll_nav

Variable	Sensitivity	Confidence	Confidence	Confidence interval	p value
		Interval (lower)	Interval (upper)		
ci_TibN	6.36	6.14	6.59	0.45	6.06E-308
ci_CalF	1.96	1.74	2.18	0.45	1.25E-58
ci_ATiF	1.78	1.56	2.00	0.44	7.61E-50
ci_PTaF	0.92	0.70	1.14	0.44	1.29E-15
ni_TibN	-0.62	-0.84	-0.39	0.45	6.83E-08
ci_CalT	0.26	0.04	0.48	0.45	2.06E-02

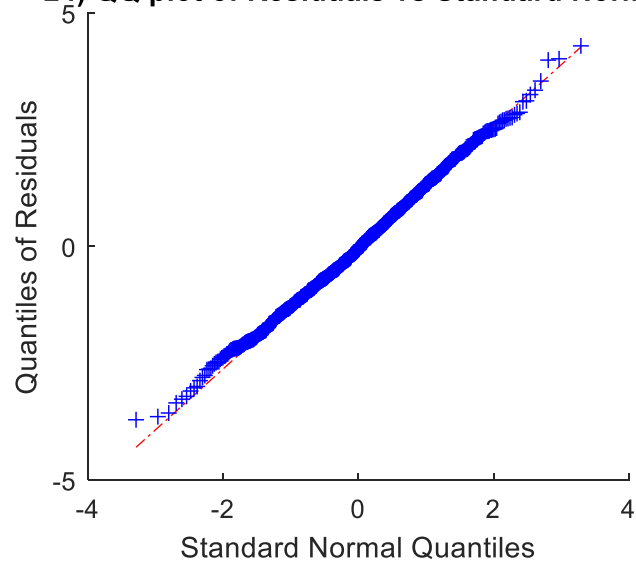
Response: talus yaw

23) QQ plot of Residuals vs Standard Normal



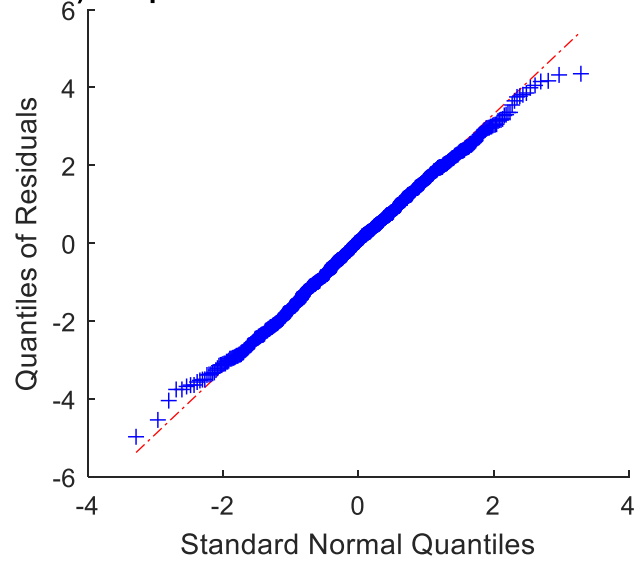
Response: talus pitch

24) QQ plot of Residuals vs Standard Normal



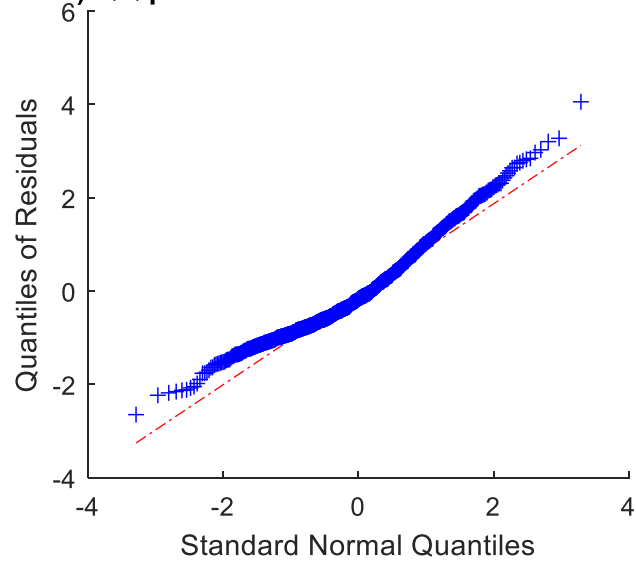
Response: talus roll

25) QQ plot of Residuals vs Standard Normal



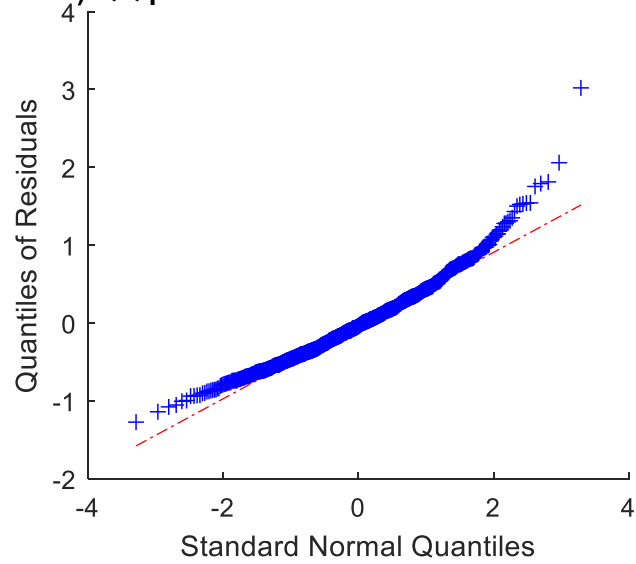
Response: navicular yaw

26) QQ plot of Residuals vs Standard Normal



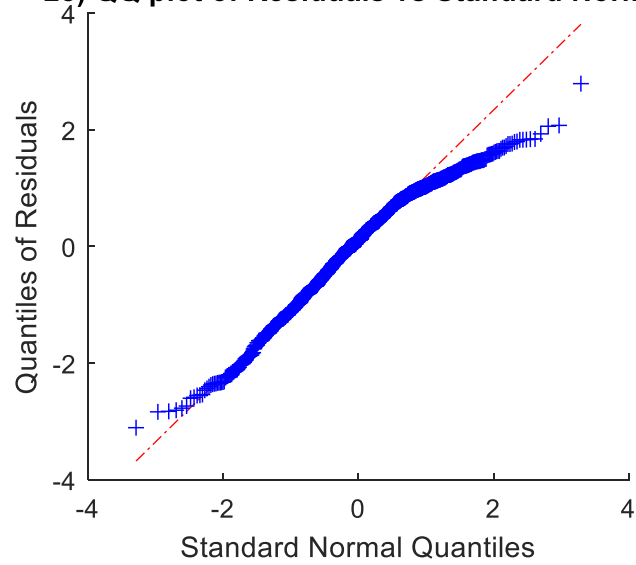
Response: navicular pitch

27) QQ plot of Residuals vs Standard Normal



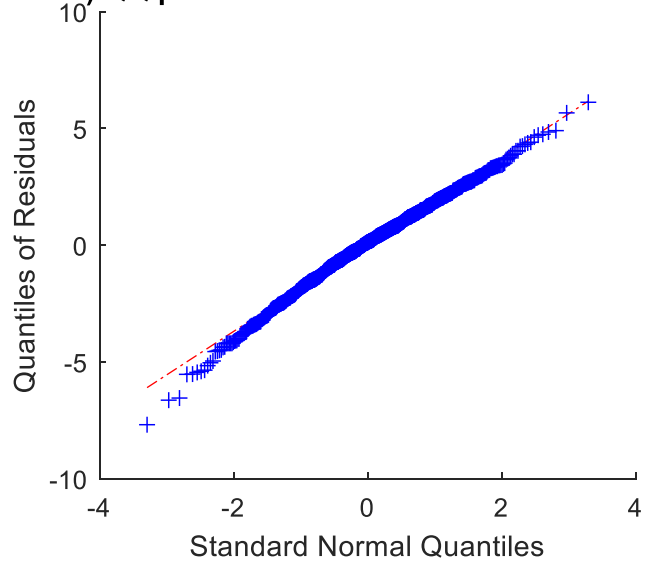
Response: navicular roll

28) QQ plot of Residuals vs Standard Normal



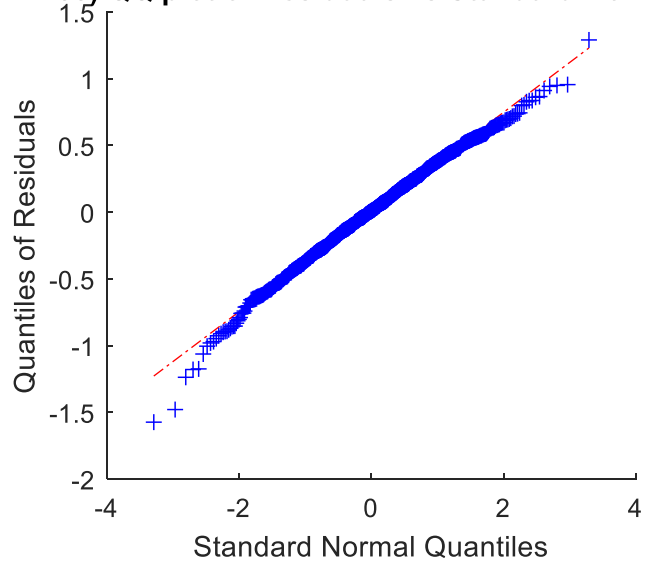
Response: fibula yaw

32) QQ plot of Residuals vs Standard Normal



Response: fibula pitch

33) QQ plot of Residuals vs Standard Normal



Response: fibula roll

